

Copyright
by
Todd Jeffrey Hoppe
2013

The Dissertation Committee for Todd Jeffrey Hoppe Certifies that this is the approved version of the following dissertation:

Laser-Based Techniques for Manipulating the Single-Cell Environment

Committee:

Jason B. Shear, Supervisor

Richard M. Crooks

Katherine A. Willets

David A. Vanden Bout

Richard A. Morrisett

Laser-Based Techniques for Manipulating the Single-Cell Environment

by

Todd Jeffrey Hoppe, B.S. Ch.

Dissertation

Presented to the Faculty of the Graduate School of

The University of Texas at Austin

in Partial Fulfillment

of the Requirements

for the Degree of

Doctor of Philosophy

The University of Texas at Austin

May 2013

Dedication

This work is dedicated to my lovely and patient wife, Emily

Acknowledgments

First and foremost, I would like to thank my advisor, Jason Shear, who provided both the environment and resources for me to succeed in this endeavor. I am also grateful to my committee members, Dr. Richard Crooks, Dr. Katherine Willets, Dr. David Vanden Bout, and Dr. Richard Morrisett for providing me their time and consideration. I offer my gratitude to all current and former members of the Shear Lab. Dr. Rex Nielson was gracious enough to provide instruction in both microfluidics and cell culture, two fields in which I would have been lost without his guidance. Dr. Eric Ritschdorff was also generous with both insight and assistance throughout my graduate career, especially in the area of photofabrication, and spent countless hours reviewing every page of this dissertation. Dr. Samira Moorjani, Dr. Bryan Kaehr, Dr. Stephanie Seidlets, Dr. Eric Spivey, Dr. Jodi Connell, Michelle Fox, Derek Hernandez, Maryam Ali, Michael Robinson, Mindy Fitzpatrick, Rikki Gartner, and Janine Elliott have all provided constructive criticism over the course of this research and I hope that I have returned the favor in kind. Thank you to Tim Hooper, who helped immensely in the process of converting ideas into instruments. I am also thankful for the support from friends and former instructors in Sand Springs, Oklahoma. I have always been proud to call myself a Sandite. To my undergraduate advisor, Dr. Gordon Purser, who so often gave his time and energy as a mentor and a friend. There are many experiences in my life that would have never been possible if not for Dr. Purser and his wife, Jane. To my friends and

family in Austin, who provided their companionship, along with food and libations, every Thursday night for as long as I can remember. To my parents, Jeff and Kathy Hoppe, and my brother, Brian, who have inspired and encouraged all of my academic pursuits. And to my wife, Emily, whose patience and compassion are unmatched. Thank you for your unconditional support. I could not have done any of this without any of you.

Laser-Based Techniques for Manipulating the Single-Cell Environment

Publication No. _____

Todd Jeffrey Hoppe, Ph. D.

The University of Texas at Austin, 2013

Supervisor: Jason B. Shear

The environment encountered by a single cell *in vivo* is a complex and dynamic system that is often simplified experimentally via *ex vivo* and *in vitro* methods. As our understanding of cell response in these basic environments grows, there is a corresponding need for techniques that modify traditional cell culture in ways that better mimic the complexities of *in vivo* systems. This dissertation examines how the three-dimensional (3D) properties of a focused pulsed laser can be incorporated within existing techniques to dynamically manipulate these microenvironments in the presence of single cells. As a modification on existing microfluidic technology for chemically dosing cells, it is shown how a cost-effective microchip laser can be used to ablate microscopic pores in a thin, biocompatible polymer membrane. These pores serve as conduits for introducing dosing reagents in close proximity to cultured cells combining subcellular resolution with spatial and temporal control. Because reagent flow is physically separated from the cell-culture flow chamber by this polymer membrane, the geometry of the reagent flow cell can be altered to accommodate multiple reagents flowing in parallel with minimal mixing due to the laminar flow characteristics of

microfluidic devices. By manipulating reagent flow, a single cell can be dosed at opposing ends by distinct reagents or by defined, stable gradients of a single reagent. Additionally, these dosing streams can be switched with subsecond temporal resolution or dynamically mixed to study potential synergistic or antagonistic effects. To define the physical environment surrounding small populations of cells, an existing platform for mask-directed multiphoton lithography is used to create biocompatible protein-based microstructures for studying cancer-cell migration and invasion in physically confined regions. In these studies, a variety of 3D shapes incorporating spatial gradients are examined with invasive cell types. Additionally, these methods have been modified to allow for *in situ* fabrication of gelatin microstructures with 3D resolution around suspended somatic cells by covalently binding a photosensitizing molecule to the protein prior to fabrication. The architecture of these microstructures is designed to provide a variety of 3D confinement scenarios with biological relevance.

Table of Contents

List of Figures	xiii
Chapter 1: Introduction	1
1.1 Laser-Based Analytical Techniques	4
1.1.1 Biological Applications of Lasers	6
1.1.2 Multiphoton Excitation	7
1.2 Microfluidics	10
1.2.1 Laminar Flow	10
1.2.2 Microfluidic Gradients	13
1.3 Multiphoton Lithography	16
1.4 Summary of Chapters	20
1.5 References	21
Chapter 2: Development of a Microfluidic Device for Real-Time Manipulation of the Subcellular Chemical Environment	27
2.1 Introduction	27
2.2 Experimental Methods	29
2.2.1 Device Design	29
2.2.2 Laser Ablation Parameters	35
2.2.3 Cell Culture	35
2.2.4 Microscopy	36
2.2.5 Chemicals	37
2.2.6 Environmental Chamber	38
2.3 Results and Discussion	39
2.3.1 Cell Culture on Polyimide Film	39
2.3.2 Laser Ablation of Polyimide Film	42
2.3.3 Real-Time Pore Ablation	46
2.3.4 Chemical Etching of the Polyimide Membrane	50
2.3.5 Open-Top Flow	53
2.3.6 Single-Cell Targeting	56

2.4 Conclusions.....	59
2.5 References.....	61
Chapter 3: Complex Multi-Reagent Dosing Patterns	64
3.1 Introduction.....	64
3.2 Experimental.....	67
3.2.1 Flow Device Design and Assembly.....	67
3.2.2 Laser Ablation.....	71
3.2.3 Cell Culture.....	72
3.2.4 Chemicals.....	73
3.2.5 Microscopy	74
3.3 Results and Discussion	74
3.3.1 Multi-Reagent Device Design.....	74
3.3.2 Reagent Switching	75
3.3.3 Variable Concentration Control.....	77
3.3.4 Arbitrary Mapping of Reagents	80
3.3.5 Subcellular Targeting with Multiple Reagents	82
3.3.6 Reagent Stream Overlap	85
3.3.7 Reagent Switching with High Temporal Resolution	88
3.4 Conclusions.....	91
3.5 References.....	93
Chapter 4: Biocompatibility of Photofabricated Protein Microstructures for Studying Cancer-Cell Migration and Invasion.....	96
4.1 Introduction.....	96
4.2 Experimental Methods.....	99
4.2.1 Fabrication Solutions	99
4.2.2 Multiphoton Fabrication	99
4.2.3 Cell Culture.....	101
4.2.4 Microscopy	102
4.2.5 Chemicals.....	102

4.3 Results and Discussion	103
4.3.1 Biocompatibility of Photofabricated Protein Microstructures for Somatic Cells	103
4.3.2 Cellular Interaction with Fabrication Materials	106
4.3.3 Invasion of Protein Microstructures	110
4.3.4 Migration through Narrow Openings	113
4.3.5 Vertical Invasion Traps	118
4.4 Conclusions	120
4.5 References	121
Chapter 5: In Situ Photofabrication of Eosin-Conjugated Gelatin Microstructures for Single-Cell Trapping	124
5.1 Introduction	124
5.2 Experimental Methods	126
5.2.1 Eosin Conjugation	126
5.2.2 Fabrication Solution	127
5.2.3 Cell Culture	128
5.2.4 Cell Preparation for Fabrication	129
5.2.5 Multiphoton Fabrication	129
5.2.6 Microscopy	133
5.2.7 Chemicals	133
5.3 Results and Discussion	133
5.3.1 In Situ Fabrication with Eosin-Conjugated Gelatin	133
5.3.2 Reducing Post-Fabrication Cytotoxicity	139
5.3.3 In Situ Fabrication in the Presence of Human Cells	143
5.3.4 Complete 3D Isolation of Single Cells	145
5.3.5 Internalization of In Situ Fabricated Particles	148
5.4 Conclusions	149
5.5 References	151

Bibliography154

List of Figures

Figure 1.1: Multiphoton excitation	8
Figure 1.2: Laminar flow in microfluidics.....	11
Figure 1.3: Microfluidic subcellular dosing.....	15
Figure 1.4: Photosensitizers	18
Figure 2.1: Microfluidic dosing device.....	31
Figure 2.2: Microfluidic device assembly	33
Figure 2.3: Cell culture on polyimide film	42
Figure 2.4: SEM of polyimide pores.....	45
Figure 2.5: Real-time pore ablation	48
Figure 2.6: Video-rate imaging of pore formation.....	49
Figure 2.7: Chemically etched polyimide film	51
Figure 2.8: Open-top access to cells	55
Figure 2.9: Subcellular dosing	58
Figure 3.1: Fully assembled flow device	69
Figure 3.2: Reagent switching	76
Figure 3.3: Variable concentration control	79
Figure 3.4: Generation of arbitrary multi-reagent dosing maps	81
Figure 3.5: Multi-reagent targeting.....	83
Figure 3.6: Dynamics of dye localization.....	85
Figure 3.7: Overlapping streams.....	86
Figure 3.8: Fast switching of reagents	89

Figure 4.1: Protein microstructures for studying cell behavior	104
Figure 4.2: Cell division	106
Figure 4.3: Cells on photofabricated protein pads	108
Figure 4.4: Gelatin interaction	109
Figure 4.5: NG108-15 invasion in protein microstructures	111
Figure 4.6: Invasion and migration	112
Figure 4.7: Open narrow channel migration	113
Figure 4.8: Gelatin spikes	115
Figure 4.9: Closed narrow channel migration.....	116
Figure 4.10: MDA-MB-231 invasion	118
Figure 4.11: Vertical invasion trap	119
Figure 5.1: In situ fabrication.....	132
Figure 5.2: Eosin conjugation.....	135
Figure 5.3: Single-cell trapping	137
Figure 5.4: Apoptosis.....	139
Figure 5.5: Reducing post-fabrication cytotoxicity	140
Figure 5.6: Cell division	142
Figure 5.7: Aneuploid division	143
Figure 5.8: MDA-MB-231 isolation.....	144
Figure 5.9: 3D isolation	146
Figure 5.10: Free-floating 3D isolation	147
Figure 5.11: Phagocytosis of photofabricated gelatin particles	149

Chapter 1: Introduction

In 1907, at Johns Hopkins University, Ross Harrison explanted a piece of embryonic frog tissue onto a sterile cover slip and bathed it with a drop of freshly drawn lymph [1]. The lymph soon clotted and Harrison watched over a period of days as a single nerve fiber grew from the tissue and branched out into the media. While many researchers had previously demonstrated the ability to maintain living sections of tissue outside the body [2], Harrison's results suggested that tissues and cells could be cultured to thrive apart from the *milieu intérieur*¹. These cells displayed a level of autonomy that established the basis of cell culture as a technique that allows researchers to observe and manipulate cells and their progeny with significant control of their environment. In the century since Harrison's discovery, cell culture has developed into a fundamental biological technique for vaccine development, stem-cell therapy, genetics, and cancer research [3].

Cells in their native environment are bombarded by chemical cues (e.g., cytokines [4], hormones [5], and growth factors [6]), as well as physical cues (e.g., substrate stiffness [7] and topography [8]), that can alter their behavior. The phenotypic plasticity of a single cell allows it to react and respond to these cues as receptors on the surface of the cell membrane integrate chemical signals [9] and focal adhesions constructed from the actin cytoskeleton interrogate the physical environment [10]. These effects mediate

¹ The self-sustaining internal environment of the body as first proposed by Claude Bernard in 1854 [3].

gene expression, leading to structural and functional transformations such as differentiation [11], growth [12], and morphogenesis [13]. The complexity created by this elaborate combination of signals makes it nearly impossible to match the action of a single cell to its antecedent cue. Removing the cell from its complex *in vivo* surroundings allows for experimental control of the environment and simplifies the process of resolving these responses on a single-cell level. Cell culture allows for the investigation of an individual response to a single stimulus, thereby adding to the fundamental understanding of cell behavior from which biological and computational models can be created to predict behavior in complex environments (e.g., cellular networks [14]). In many cases, however, the emergence of synergistic and antagonistic effects complicates the reconstruction [15]. Each additional level of complexity in the biological model necessitates a corresponding intricacy in the tools used to study it. While traditional 2D cell culture techniques on a petri dish or in a flask are attractive for their simplicity, many of these techniques lack the flexibility and biological relevance for interrogating more complex cellular behavior.

This dissertation presents techniques that allow for the dynamic remodeling of cellular microdomains to mimic specific complexities within the cellular microenvironment. For example, it has been shown that stem-cell division and differentiation is directed by their niche – a collection of the physical and chemical cues in the cellular microenvironment [16]. A highly specific series of chemical cues is required to induce the transcription factors that eventually lead to stem cell differentiation

[17]. However, in similar chemical environments, gene expression, morphology, and protein upregulation within naïve stem cells shifts as a function of substrate stiffness. Mesenchymal stem cells derived from bone marrow will develop branching that is characteristic of neurons, exhibit a neurogenic transcription profile, and express neuron-specific markers β 3 tubulin and neurofilament heavy chain when cultured on substrates with an elastic modulus similar to brain tissue (0.1-1 kPa). The same cell type exhibits myogenic behavior (spindle formation, myoD1 upregulation) on surfaces with elasticity similar to muscle (10-20 kPa) and osteogenic behavior (F-actin stress fibers, CBF α 1 upregulation) on surfaces with elasticity similar to collagenous bone precursors (25-50 kPa) [18]. When the mechano-transducers responsible for converting these physical cues to intracellular chemical signals (nonmuscle myosin II) are inhibited, stem cells no longer differentiate as a function of surface modulus. Similarly, immunological cells define their migratory behavior using a flexible hierarchy of chemotactic signals. Human neutrophils (the most abundant of the leukocytes) integrate a variety of signals from host cells, as well as non-native cells, to determine their chemotaxis *in vivo*. In the presence of both native chemokines and bacteria-derived factors, neutrophils will preferentially migrate towards bacteria-derived factors [19]. Neutrophil migration is also partially determined by the cell's history with various chemoattractants. These cells will preferentially migrate towards newly discovered attractants even when that migration pattern takes the cell away from the highest concentrations of the chemotactic gradient that originally attracted the cell [20]. In each of these cases, the combinatorial effect created by multiple signals in a complex environment serves to convolute cell behavior

beyond what would be predicted by each signal in isolation. Understanding how a single cell assimilates various combinations and sequences of chemical and physical cues requires techniques that can dynamically shape the chemical and physical environments below the resolution of a single cell.

Modern advances in microtechnology offer a variety of approaches for recreating aspects of biological environments in a controlled setting. Of particular interest, both microfluidic and microfabrication techniques have been applied in the Shear Lab for these purposes [21-29]. Microfluidic approaches are attractive because cells can be exposed to a defined chemical environment, as waste products and interfering chemical signals are continuously washed away. Microfabrication provides a means for defining physical microenvironments on the scale of a single cell. This dissertation introduces a laser-based microfluidics technique for dynamically changing the chemical microenvironment around single cells, as well as a laser-based microfabrication technique for defining the three-dimensional (3D) physical microenvironment around single cells.

1.1 LASER-BASED ANALYTICAL TECHNIQUES

Soon after he invented the original MASER in 1954, Charles Townes acknowledged the potential of a maser-type oscillator that could emit radiation at visible and IR wavelengths [30]. While Townes theorized at the time how these “infrared and optical masers” could be constructed, Theodore Maiman was the first to demonstrate a laser in the visible spectrum in 1960, a 1-cm ruby crystal pumped by a flashlamp, with

emission lines at 692.9 and 694.3 nm [31]. While Maiman's ruby laser was a three-level system that required significant pumping to achieve population inversion, the discovery of other gain mediums allowed for stable lasing in the visible spectrum with lower thresholds for pumping. In the decade after the first ruby laser demonstration, a variety of laser wavelengths in the visible spectrum were presented using gain mediums including gases (e.g., HeNe, CO₂, and Ar) [32], dyes (e.g., phthalocyanine, stilbene, and rhodamine 6G) [33], and other solid-state materials (e.g., Nd:YAG) [34]. Rapid advances in technology during this time period allowed lasers to be easily incorporated in a variety of fields of scientific research and practical applications in fiber optics, optical disc drives, barcode scanning, and laser printing. Advances in spectroscopic detection limits were made possible by the development of the laser, including surface-enhanced Raman scattering for single-molecule imaging [35] and ultra-fast laser spectroscopy for time-correlated single-photon counting [36]. Laser ablation is now commonly used to vaporize and ionize samples for electrospray ionization [37] and inductively coupled plasma mass spectrometry [38]. The Nobel Prize was awarded for laser-based techniques for cooling individual atoms to μK temperatures in optical molasses [39], frequency combs that serve as optical rulers for measuring absolute optical frequencies [40], and femtosecond pump-probe spectroscopy for measuring short-lived reaction intermediates and transition states [41]. Additionally, developments in laser technology since 1960 have also led to significant advances in bioanalytical and biological imaging techniques.

1.1.1 Biological Applications of Lasers

In many instances, laser-based techniques in biology offer advantages over traditional methods (e.g., epifluorescence, fixing and sectioning, puffer pipet delivery) for probing and manipulating cellular microenvironments. For example, the coherence of laser light allows it to be focused to extremely small focal areas by high numerical aperture optics for enhanced 2D and 3D resolution, while its spectral purity allows for selective excitation of fluorescent labeling molecules and photocatalysts. Lasers are also easily incorporated within existing optical imaging systems commonly used by biologists (e.g., optical microscopes and endoscopes), many of which benefit from deep sampling depths and non-destructive imaging relative to electron and scanning probe microscopy. For example, confocal microscopy and its optical sectioning capabilities allow for 3D reconstruction of cellular organelles and their internal structure [42]. Techniques such as fluorescence cross-correlation spectroscopy (FCCS) have made it possible to measure the binding kinetics of biomolecules in a living cell [43]. Lasers have provided the means for developing super resolution techniques capable of resolving cellular structures and architecture beyond the diffraction limit, including individual actin microfilaments less than 10 nm in diameter [44]. Under specific conditions (high numerical aperture focusing, high peak powers), lasers have also made it possible to perform non-linear photochemistry in biological samples with high spatial and temporal resolution via multiphoton excitation.

1.1.2 Multiphoton Excitation

In a single-photon excitation regime, an electron is excited from the singlet ground state (S_0) to a singlet excited state (S_1) by absorption of a photon corresponding to the energy gap between these levels. By comparison, multiphoton excitation is a low probability event that only occurs when multiple lower-energy photons are absorbed by a single molecule nearly simultaneously (Figure 1.1). In both cases, we can think of the absorption of one (or more) photons in terms of a chemical reaction [45]:



where M represents the ground-state molecule and the absorption of n photons ($h\nu$) results in the formation of an excited-state molecule (M^*). The kinetics of this reaction can then be represented as:

$$\frac{d[M^*]}{dt} = k[h\nu]^n[M] = \delta I^n[M], \quad [1.3]$$

where k is the rate constant, δ is the excitation cross-section ($\text{cm}^{2n}(\text{s}/\text{photon})^{n-1}$), and I is the intensity of the excitation radiation ($\text{photons s}^{-1} \text{cm}^{-2}$). Because the rate of excitation scales as a function of I^n , it follows that multiphoton processes require significantly higher photon flux than single-photon excitation. This can be achieved by focusing a high-peak power laser beam through a high numerical aperture (NA) objective, where the density of photons required for multiphoton excitation can be delivered to extremely small volumes ($\sim 1 \mu\text{m}^3$), resulting in highly localized excitation.

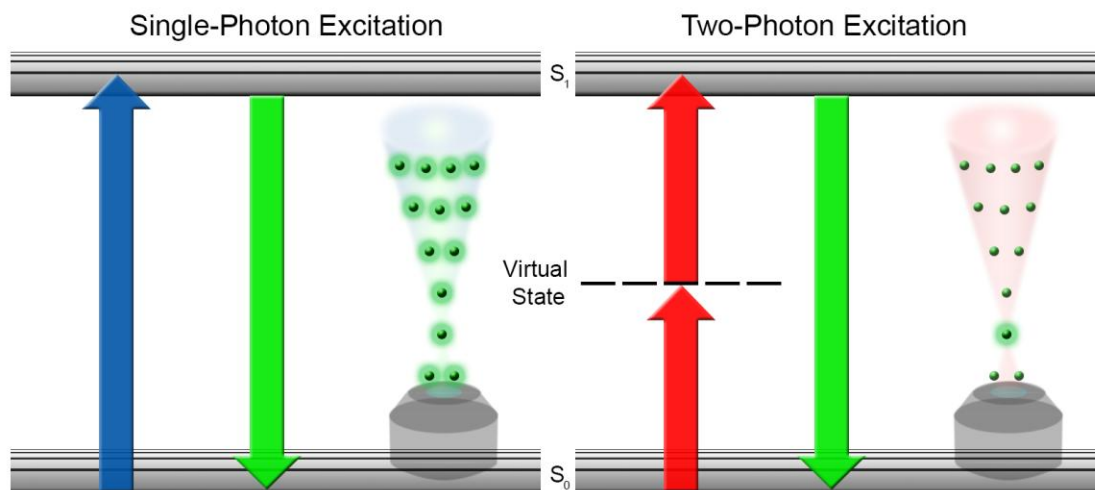


Figure 1.1: Multiphoton excitation. A simplified Jablonski diagram illustrating the differences between single-photon and two-photon excitation. In single-photon excitation, a photon is absorbed that matches the energy gap between ground state (S_0) and excited state (S_1). Focused light at the excitation wavelength excites molecules along the entire optical axis (left). In two-photon excitation, two lower energy photons that collectively match the energy gap between S_0 and S_1 are absorbed. Focused light at the two-photon excitation wavelength results in excitation only when the photon flux is high enough for a molecule to absorb two photons near simultaneously. Using a high-peak power laser and high numerical aperture objective, multiphoton excitation only occurs in a small volume centered at the focal spot with essentially no excitation at other points along the optical axis (right).

In 1990, the Webb Lab was the first to describe how multiphoton microscopy could be used for non-destructive optical sectioning of living cells, as well as the spatially resolved photolytic release of caged molecules [46]. Although these investigators used a pulsed dye laser in their initial demonstration, advancements around the same time in solid-state laser technology and mode-locking led to the development of the tool most

commonly used in multiphoton microscopy, the femtosecond-pulsed titanium-sapphire oscillator (Ti:S) [47]. With its ultrashort ($\sim 10\text{-}200$ fs) pulses and low duty cycle (10^{-5}), a Ti:S beam of low average power (~ 30 mW) can deliver terawatt (10^{12} W cm^{-2}) peak intensities to a $1\ \mu\text{m}^3$ (1 fL) volume within a sample by focusing through a 1.30 NA objective. These properties allow for microscale 3D resolution ideal for photolithography because the photon flux required for multiphoton processes is achieved only at axial positions close to the focal spot. Additionally, the near-IR wavelengths of a Ti:S oscillator experience less scatter and typically are less damaging within biological material, allowing for greater depth of focusing within these samples. Less expensive lasers, such as the Q-switched frequency-doubled (532 nm) Nd:YAG used in Chapters 2 and 3, can also be used in conjunction with high numerical aperture optics to produce multiphoton excitation at the sacrifice of longer pulse widths (~ 500 ps) and a lower repetition rate (~ 7.5 kHz). Multiphoton excitation is also possible, but impractical, with continuous-wave lasers due to the high average powers required in the absence of pulsing to achieve high peak intensities in the focal volume. The techniques presented in this dissertation rely on multiphoton excitation from a focused, pulsed laser beam (mode-locked Ti:S or Q-switched Nd:YAG) to supplement the advantages of microfluidics to pattern the chemical microenvironment of single cells and microfabrication to construct the physical microenvironment of single cells.

1.2 MICROFLUIDICS

1.2.1 Laminar Flow

Microfluidics has its roots in microanalytical chromatography techniques that allow for high sensitivity and resolution from small sample volumes. Advances in capillary electrophoresis, in particular, drove improvements in microfluidic technology [48]. It was not until the early-1990s, with funding from the Defense Advanced Research Projects Agency (DARPA), that the current wave of microfluidics began. Just as low-resolution contact lithography was losing its utility for manufacturing the shrinking features of integrated circuits, researchers were beginning to realize that this instrumentation was ideal for creating the relatively large features (μm - mm) necessary for microfluidics. Initially, microfluidic devices were used for high-throughput DNA sequencing [49], chemical mixers [50], microscale total analysis systems (μTAS) [51], and biological microelectromechanical systems (bioMEMS) [52]. In 1999, George Whitesides was the first to demonstrate how a simple microfluidic chip could be used to pattern cell substrates, stain organelles of cultured cells, and selectively position different cell types [53].

Microfluidic technology works well for defining cellular microenvironments because the dimensions of these devices are on the same scale as most somatic cells (10-100 μm). At these dimensions, the viscous forces of solution flow overtake inertial forces, resulting in laminar flow that lacks the turbulence that complicates fluid dynamics at larger scales [54]. This laminar flow regime allows for the creation of stable boundaries between concurrent flow of miscible reagent solutions that can be used to

pattern the chemical environment around cultured cells (Figure 1.2). Microfluidic platforms offer the additional benefit that small numbers of cells and small volumes of reagents are required for each experiment. Techniques that take advantage of the unique properties of microfluidics are now used to create complex mixtures [55], introduce gradients [56], and provide 3D delivery of reagents [57] in cell culture.

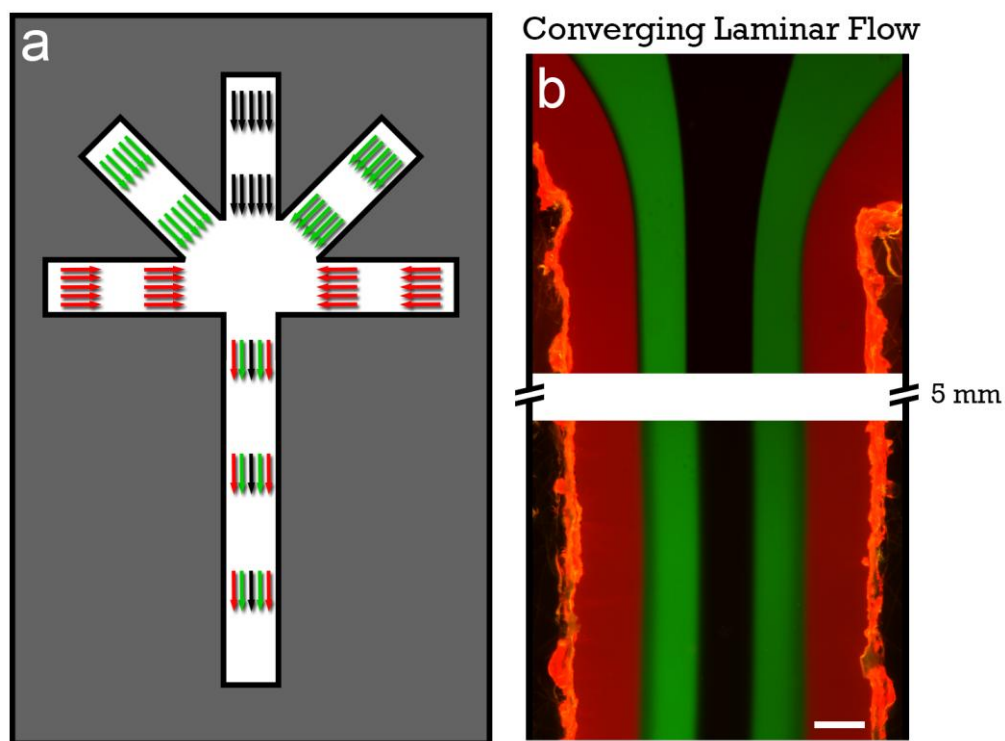


Figure 1.2: Laminar flow in microfluidics. (a) In a flow cell geometry with five laminar inlets and one outlet, all five streams combine and maintain laminarity in a single channel. (b) Experimental demonstration of part (a), where five confluent streams of (left to right) 50 μM rhodamine (red), 50 μM fluorescein (green), water, 50 μM fluorescein, and 50 μM rhodamine flow at individual rates of 0.1 mL min^{-1} . The streams combine in the central channel and flow concurrently in a laminar flow regime with minimal amounts of mixing at distances of 5 mm downstream. Scale Bar = 200 μm .

In fluid mechanics, the flow properties of an incompressible fluid are represented mathematically by the Navier-Stokes equations, a set of nonlinear second-order partial differential equations derived from the application of Newton's Second Law to describe the conservation of linear momentum in viscous fluid flow [54]. Solutions to the Navier-Stokes equations produce a vector field describing the flow velocity at each point in space and time. While the existence of singularities in the Navier-Stokes equations continue to trouble mathematicians more than 150 years after their discovery, simplified terms derived from the Navier-Stokes equations such as the Strouhal number (oscillating flow), Froude number (free-surface flow), Euler number (frictional flow), and Reynolds number (laminar flow) have helped define fluid dynamics [54].

Of particular interest to the field of microfluidics is the Reynolds number. Through dimensional analysis, both the independent and dependent variables within the Navier-Stokes equations can be simplified with characteristic values to provide a dimensionless Navier-Stokes equation that exhibits dynamic similitude. One of the terms within this dimensionless Navier-Stokes equation, the Reynolds number (Re), predicts whether flow within a channel will be laminar or turbulent. The Reynolds number, defined as the ratio of inertial forces to viscous forces, is expressed as:

$$\text{Re} = \frac{\rho v d}{\mu}, \quad [1.1]$$

where ρ is the density of the fluid, v is the mean velocity of the fluid, d is the hydraulic diameter of the channel, and μ is the dynamic viscosity of the fluid [58]. For most

geometries, a Reynolds number below 2,000 corresponds to laminar flow [54]. In practice, the actual transition point from laminar to turbulent flow depends on local conditions at the walls (surface roughness, vibration, etc.), and this transition occurs over a range of Reynolds numbers where flow is a combination of both regimes (transitional flow). For aqueous solution flow in a microfluidic device, where ρ is on the order of 10^3 kg m^{-3} and μ is on the order of $10^{-3} \text{ kg m}^{-1} \text{ s}^{-1}$, Re is well below the laminar/turbulent transition point at reasonable flow rates. For example, a flow channel with a diameter of 1 mm would require flow rates above 2 m s^{-1} (120 mL min^{-1}) to exceed laminar flow conditions. The microfluidic device (and its various geometries) discussed in Chapters 2 and 3 produce calculated Re values several orders of magnitude below this transition point, resulting in a low probability of encountering turbulent flow in the range of flow rates used during experimentation.

1.2.2 Microfluidic Gradients

While there are obvious advantages to the spatial control that the steep boundaries between reagents in microfluidics provide, there are many instances where a diffuse gradient would have more biological relevance. In the case of chemotaxis, many cell types migrate according to the length and shape of the chemokine gradient they perceive [59]. In cancer metastasis, the breast cancer cell line MDA-MB-231² (whose invasive properties are further explored in Chapter 4) overexpresses receptors for epidermal growth factor (EGF) [60], an inherent quality that drives cell invasion into an EGF

² MDA-MB-231 is a metastatic epithelial-like cell line obtained in 1973 from the pleural effusion site of a 51-year old caucasian female presenting adenocarcinoma at M.D. Anderson Cancer Center (Houston, TX).

gradient and leads to invasion through the basement membrane, the first step of metastasis.

To create more complex gradients within a microfluidic device, a series of mixing zones can be fabricated in the flow chip (e.g., the “Christmas tree” geometry [61]). For simple gradients in a device that maintains the ability to create steep laminar boundaries, free-diffusion gradient generators are often used [62]. Gradients are established in these geometries by the diffusion of reagents perpendicular to the flow direction. Although little to no convective mixing is present in a laminar flow regime, mass transfer still occurs via diffusion as a function of $\sqrt{\text{time}}$, as dictated by the Einstein equation. In these instances, the length of lateral diffusion (and thus the width of the gradient or mixing region) varies along the longitudinal length of the channel as fluid travels downstream over time. The advantage to free-diffusion gradients is that these regions can be easily manipulated by adjusting relative flow rates. Once the system reaches mass transport equilibrium, the dimensions of these mixing zones remain stable. In contrast, the transient gradients created by traditional micropipet delivery of reagents dissipate quickly in all dimensions as the reagent diffuses away from the initial delivery point [63].

This dissertation presents a microfluidic device consisting of two stacked flow cells separated by a thin (7.6 μm) polyimide membrane that also serves as a substrate for cell culture (Figure 1.3). Laser ablation of the membrane by a Q-switched, frequency-doubled (532 nm) Nd:YAG laser creates a narrow ($\sim 2\text{-}\mu\text{m}$ diameter) pore that serves as a conduit between reagent and cell culture flow. Reagent streams emerging

from these pores are integrated within the laminar flow regime in the cell culture region creating narrow dosing streams with steep, stable gradients. Ablation allows for dynamic creation of dosing streams while the laminar flow properties of the reagent solutions allow for dynamic shifts in dosing patterns, including multi-reagent subcellular targeting and stable gradient formation and manipulation.

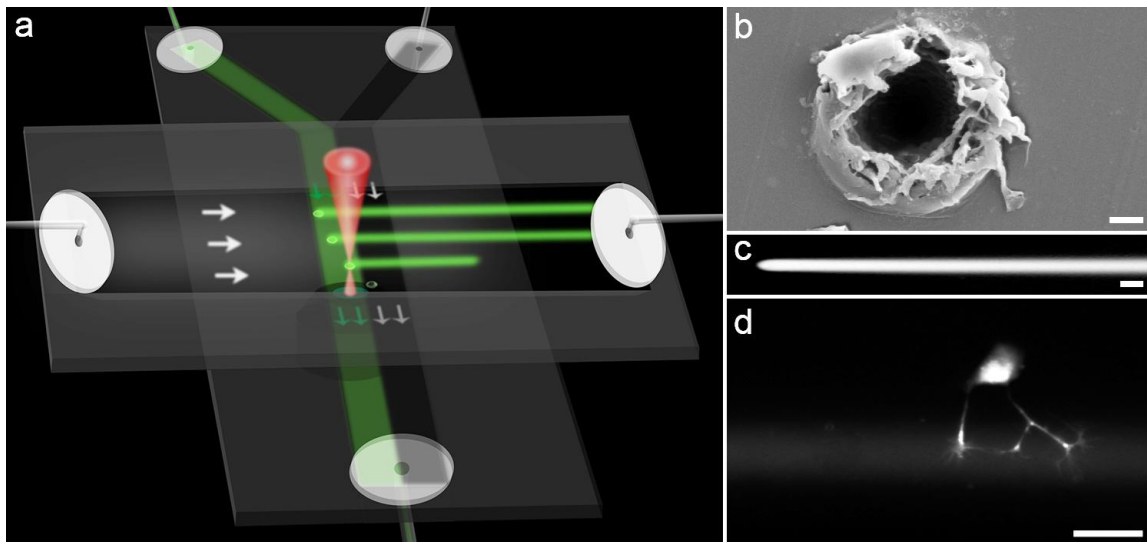


Figure 1.3: Microfluidic subcellular dosing. (a) Graphic showing the general orientation of the microfluidic device presented in this dissertation. Two perpendicular flow cells are separated by a thin (7.6- μm -thick) polyimide membrane that can be ablated by a focused Nd:YAG laser. (b) Scanning electron micrograph of a pore in polyimide film. Scale bar = 2 μm . (c) A single dosing stream (250 μM DAPI) introduced into the laminar flow regime of a cell culture flow chamber. Scale bar = 20 μm . (d) Neuritic arborizations of a neuroblastoma-glioma hybrid cell are selectively dosed with MitoTracker Red CMXRos. The dye has diffused through the cytosol to the cell body. Scale bar = 50 μm .

1.3 MULTIPHOTON LITHOGRAPHY

Traditional photolithography is primarily a 2D technique based on the same principles as early versions of photography (“drawing with light” [64]), where a photoresist is selectively exposed via negative masking to ultraviolet (UV) radiation, resulting in the fabrication of microscale features. The basic concept remains essential for microelectromechanical systems (MEMS) and semiconductor device fabrication, and continues to be adapted to push the boundary of diffraction-limited resolution (e.g., immersion lithography). Photolithography has also been adapted as a precursor for soft lithography, producing polymer stamps for patterning, molding, and embossing [65]. These techniques have been used to create a variety of interesting surface features and geometries for studying the effects of physical microdomains on cell behavior (e.g., the effects of spatial gradients on cancer-cell invasion), but they suffer from two primary drawbacks when applied to studying biological systems. The first is that contact lithography is inherently a 2D patterning technique most useful for producing shallow features on a flat surface. Some researchers have used creative methods for producing pseudo-3D features via molding [66], but these techniques are limited by the inability to remove molds in a non-destructive fashion from beneath or within true 3D features. Additionally, the photolithographic microstructures designed for cell studies are often constructed from materials (e.g., acrylate resins or silicon polymers) that were selected for their fabrication properties, but that have no inherent biological relevance and can be toxic to cells (e.g., chemical leaching of cytotoxic species).

Photolithographic techniques have also been adapted for crosslinking biopolymers (e.g., proteins and peptides) in patterned architectures. Elastomeric stamps created from soft lithography techniques can be used to mold highly concentrated protein solutions that are cured by single-photon (UV or visible)-initiated crosslinking³. These crosslinking reactions occur at the more easily photooxidized residues (Tyr [67], as well as His and Lys [68]), producing a patterned architecture that remains adhered to the surface when the mold is removed. Protein photocrosslinking events also require a photosensitizing molecule that absorbs one or more photon(s) to promote the reaction (Figure 1.4). There are two primary types of photosensitizers used for photocrosslinking that are classified by the reaction mechanism leading to protein crosslinking after photosensitizer excitation. Type I photosensitizers (e.g., flavin adenine dinucleotide) proceed via direct one-electron transfer with the protein, creating a reactive radical by hydrogen abstraction from the more easily oxidized residues. Type II photosensitizers (e.g., xanthene dyes) proceed by transferring energy to ground-state triplet oxygen ($^3\text{O}_2$) from the triplet state of the dye, creating the highly reactive singlet oxygen molecule ($^1\text{O}_2$) [69]. Although type II photosensitizers have been demonstrated as the more robust crosslinking initiators [70], singlet oxygen reactivity with DNA, proteins, and lipids makes this class of sensitizing molecules phototoxic to cells. Techniques such as photodynamic therapy take advantage of this phototoxicity to selectively kill cells *in vivo* [71]. A strategy for reducing this inherent phototoxicity by limiting the diffusion of singlet oxygen is presented in Chapter 5.

³ Unpublished results obtained in the Shear Lab.

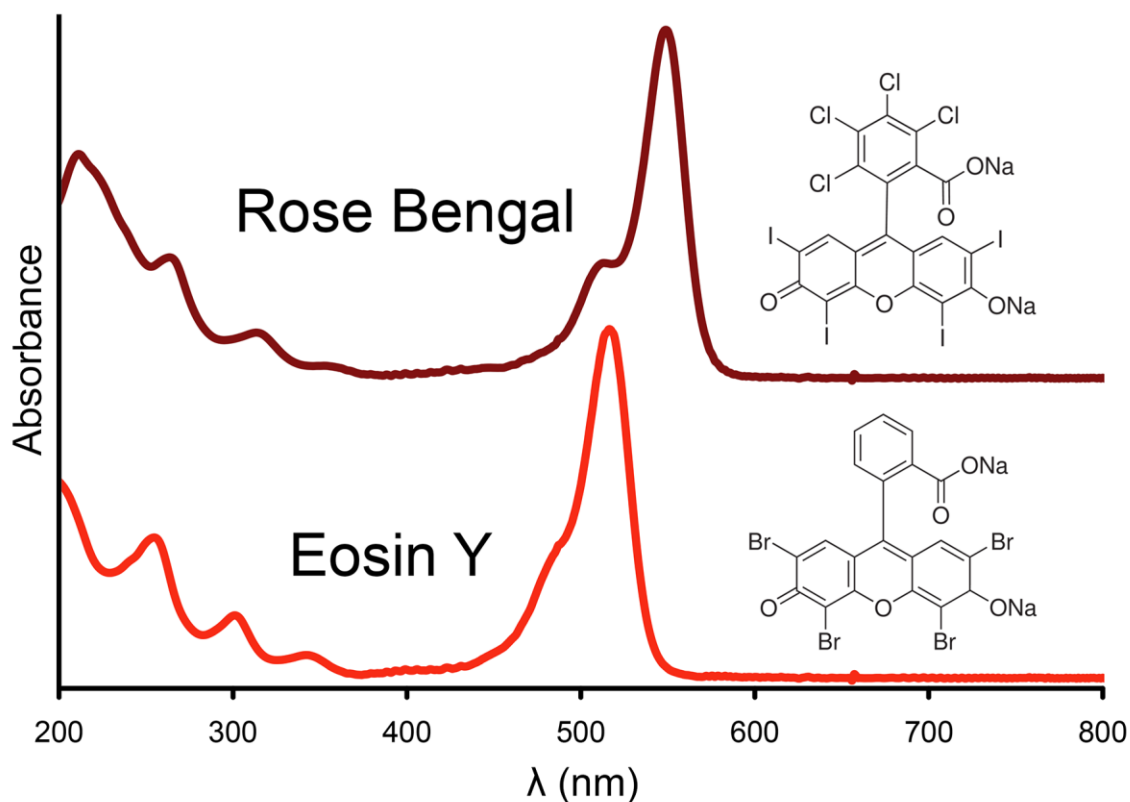


Figure 1.4: Photosensitizers. Chemical structures of the two type II photosensitizers, eosin Y and rose bengal, used for protein photocrosslinking in this dissertation shown with their respective absorbance spectrum in a HEPES-buffered saline (pH = 7.1) solvent. Although neither dye absorbs strongly at 740 nm (rose bengal, $\epsilon = 3.6 \text{ M}^{-1} \text{ cm}^{-1}$; eosin, $\epsilon = 2.2 \text{ M}^{-1} \text{ cm}^{-1}$), both dyes can be excited for multiphoton excitation by a Ti:S oscillator tuned to 740 nm.

While protein photocrosslinking allows for the creation of microstructures from more biologically relevant materials, these techniques are still limited by the axial resolution of traditional lithography. The creation of true 3D structures requires the ability to localize this photochemistry within solution, a technique made possible through

multiphoton excitation. Multiphoton fabrication arose from the realization that the same 3D capabilities of multiphoton fluorescence could be applied to microfabrication. One of the earliest demonstrations of this technique came from Pitts, *et al.* in 2000 by photocrosslinking bovine serum albumin (BSA) photosensitized by rose bengal [72]. In the Shear Lab, multiphoton lithography (MPL) has progressed from a stage-scanned lineographic technique used for drawing lines around motile *E. coli* and directing neurite outgrowth [23] to a laser-scanned mask-directed 3D microprinting technique for fabricating complex, arbitrary 3D structures [24]. Current methods employ a galvanometer-driven scan mirror that raster scans the laser beam across the face of a dynamic reflective mask allowing for plane-by-plane fabrication of complex 3D architectures when synchronized with stage stepping in the axial dimension [25]. In recent years, these MPL platforms have been used to pattern chemical cues in hydrogels for guiding dorsal root ganglion and neural progenitor cells [26] and to create BSA ‘lobster traps’ for isolating and investigating the social behavior of small populations of bacteria [27]. The technique has also been adapted with multi-focal MPL for rapid prototyping [28] and with high-viscosity reagents to create free-floating protein architectures [29]. My work in MPL builds on the knowledge and infrastructure gained from these techniques to present unique strategies for defining the physical microenvironment for somatic cells.

1.4 SUMMARY OF CHAPTERS

This dissertation describes the development of laser-based techniques for manipulating the physical and chemical environments around cultured somatic cells. A microfluidic platform is presented for dynamically manipulating the chemical microenvironment with subcellular resolution. This technique pairs a Q-switched, frequency-doubled (532 nm) Nd:YAG laser to a microfluidic cell culture chip creating a dynamic cell-dosing system that allows for multi-reagent dosing, gradient generation, complex mixing patterns, and sub-second switching. Chapter 2 discusses the development and evolution of a more cell-compatible and cost-effective microfluidic-based cell dosing device. Chapter 3 illustrates how small changes to the microfluidic infrastructure allow for complex dosing regimes and can be used to increase temporal resolution of drug delivery. Additionally, a multiphoton lithographic platform is presented for defining the physical microenvironment for somatic cells in a noninvasive fashion. Chapter 4 describes the fabrication of biocompatible gelatin-based microstructures in arbitrary geometries for the study of cancer-cell migration and invasion in physically confined spaces. Chapter 5 focuses on adapting this technique to accommodate *in situ* fabrication and 3D isolation of single cells by covalently binding the photosensitizing molecule (eosin) to the crosslinked protein (gelatin) prior to fabrication.

1.5 REFERENCES

1. Harrison, R. G.; Greenman, M. J.; Mall, F. P.; Jackson, C. M. Observations of the living developing nerve fiber. *The Anatomical Record* **1907**, *1*, 116–128.
2. Schultheiss, D.; Bloom, D. A.; Wefer, J.; Jonas, U. Tissue engineering from Adam to the zygote: historical reflections. *World Journal of Urology* **2000**, *18*, 84–90.
3. Landecker, H. *Culturing life : how cells became technologies*; Harvard University Press: Cambridge, Mass., **2007**.
4. Finkel, M.; Oddis, C.; Jacob, T.; Watkins, S.; Hattler, B.; Simmons, R. Negative inotropic effects of cytokines on the heart mediated by nitric oxide. *Science* **1992**, *257*, 387–389.
5. Porterfield, S. P.; Hendrich, C. E. The role of thyroid hormones in prenatal and neonatal neurological development – Current perspectives. *Endocrine Reviews* **1993**, *14*, 94–106.
6. Jones, J. I.; Clemmons, D. R. Insulin-like growth factors and their binding proteins: biological actions. *Endocrine Reviews* **1995**, *16*, 3–34.
7. Discher, D. E. Tissue cells feel and respond to the stiffness of their substrate. *Science* **2005**, *310*, 1139–1143.
8. Brunette, D. M. The effects of implant surface topography on the behavior of cells. *The International Journal of Oral and Maxillofacial Implants* **1988**, *3*, 231–246.
9. Kahn, C. R. Membrane receptors for hormones and neurotransmitters. *The Journal of Cell Biology* **1976**, *70*, 261–286.
10. Pelham, R. J.; Wang, Y. Cell locomotion and focal adhesions are regulated by substrate flexibility. *Proceedings of the National Academy of Sciences* **1997**, *94*, 13661–13665.
11. Umesono, K.; Giguere, V.; Glass, C. K.; Rosenfeld, M. G.; Evans, R. M. Retinoic acid and thyroid hormone induce gene expression through a common responsive element. *Nature* **1988**, *336*, 262–265.
12. Kume, N.; Gimbrone, M. A. Lysophosphatidylcholine transcriptionally induces growth factor gene expression in cultured human endothelial cells. *Journal of Clinical Investigation* **1994**, *93*, 907–911.

13. Staehling-Hampton, K.; Jackson, P. D.; Clark, M. J.; Brand, A. H.; Hoffmann, F. M. Specificity of bone morphogenetic protein-related factors: cell fate and gene expression changes in *Drosophila* embryos induced by decapentaplegic but not 60A. *Cell Growth and Differentiation* **1994**, *5*, 585–593.
14. Friedman, N. Inferring cellular networks using probabilistic graphical models. *Science* **2004**, *303*, 799–805.
15. Balkwill, F. R.; Burke, F. The cytokine network. *Immunology Today* **1989**, *10*, 299–304.
16. Spradling, A.; Drummond-Barbosa, D.; Kai, T. Stem cells find their niche. *Nature* **2001**, *414*, 98–104.
17. Kratchmarova, I.; Blagoev, B.; Haack-Sorensen, M.; Kassem, M.; Mann, M. Mechanism of divergent growth factor effects in mesenchymal stem cell differentiation. *Science* **2005**, *308*, 1472–1477.
18. Engler, A. J.; Sen, S.; Sweeney, H. L.; Discher, D. E. Matrix elasticity directs stem cell lineage specification. *Cell* **2006**, *126*, 677–689.
19. Foxman, E. F.; Kunkel, E. J.; Butcher, E. C. Integrating conflicting chemotactic signals. The role of memory in leukocyte navigation. *The Journal of Cell Biology* **1999**, *147*, 577–588.
20. Foxman, E. F.; Campbell, J. J.; Butcher, E. C. Multistep navigation and the combinatorial control of leukocyte chemotaxis. *The Journal of Cell Biology* **1997**, *139*, 1349–1360.
21. Nielson, R.; Shear, J. B. Parallel chemical dosing of subcellular targets. *Analytical Chemistry* **2006**, *78*, 5987–5993.
22. Moorjani, S.; Nielson, R.; Chang, X. A.; Shear, J. B. Dynamic remodeling of subcellular chemical gradients using a multi-directional flow device. *Lab on a Chip* **2010**, *10*, 2139–2146.
23. Kaehr, B.; Allen, R.; Javier, D. J.; Currie, J.; Shear, J. B. Guiding neuronal development with in situ microfabrication. *Proceedings of the National Academy of Sciences* **2004**, *101*, 16104–16108.
24. Kaehr, B.; Shear, J. B. Mask-directed multiphoton lithography. *Journal of the American Chemical Society* **2007**, *129*, 1904–1905.

25. Nielson, R.; Kaehr, B.; Shear, J. B. Microreplication and design of biological architectures using dynamic-mask multiphoton lithography. *Small* **2009**, *5*, 120–125.
26. Seidlits, S. K.; Schmidt, C. E.; Shear, J. B. High-resolution patterning of hydrogels in three dimensions using direct-write photofabrication for cell guidance. *Advanced Functional Materials* **2009**, *19*, 3543–3551.
27. Connell, J. L.; Wessel, A. K.; Parsek, M. R.; Ellington, A. D.; Whiteley, M.; Shear, J. B. Probing prokaryotic social behaviors with bacterial “lobster traps”. *mBio* **2010**, *1*, e00202-10–17.
28. Ritschdorff, E. T.; Nielson, R.; Shear, J. B. Multi-focal multiphoton lithography. *Lab on a Chip* **2012**, *12*, 867–871.
29. Spivey, E. C.; Ritschdorff, E. T.; Connell, J. L.; McLennon, C. A.; Schmidt, C. E.; Shear, J. B. Multiphoton lithography of unconstrained three-dimensional protein microstructures. *Advanced Functional Materials* **2013**, *23*, 333–339.
30. Schawlow, A.; Townes, C. Infrared and optical masers. *Physical Review* **1958**, *112*, 1940–1949.
31. Maiman, T. H. Stimulated optical radiation in ruby. *Nature* **1960**, *187*, 493–494.
32. Javan, A.; Bennett, W.; Herriott, D. Population inversion and continuous optical maser oscillation in a gas discharge containing a He-Ne mixture. *Physical Review Letters* **1961**, *6*, 106–110.
33. Sorokin, P. P.; Lankard, J. R. Stimulated emission observed from an organic dye, chloro-aluminum phthalocyanine. *IBM Journal of Research and Development* **1966**, *10*, 162–163.
34. Geusic, J. E.; Marcos, H. M.; Van Uitert, L. G. Laser oscillations in Nd-doped yttrium aluminum, yttrium gallium and gadolinium garnets. *Applied Physics Letters* **1964**, *4*, 182–184.
35. Kneipp, K.; Wang, Y.; Kneipp, H.; Perelman, L.; Itzkan, I.; Dasari, R.; Feld, M. Single molecule detection using surface-enhanced Raman scattering (SERS). *Physical Review Letters* **1997**, *78*, 1667–1670.
36. Becker, W.; Bergmann, A.; Hink, M. A.; König, K.; Benndorf, K.; Biskup, C. Fluorescence lifetime imaging by time-correlated single-photon counting. *Microscopy Research and Technique* **2004**, *63*, 58–66.

37. Nemes, P.; Vertes, A. Laser ablation electrospray ionization for atmospheric pressure, in vivo, and imaging mass spectrometry. *Analytical Chemistry* **2007**, *79*, 8098–8106.
38. Gray, A. L. Solid sample introduction by laser ablation for inductively coupled plasma source mass spectrometry. *The Analyst* **1985**, *110*, 551–556.
39. Chu, S.; Hollberg, L.; Bjorkholm, J.; Cable, A.; Ashkin, A. Three-dimensional viscous confinement and cooling of atoms by resonance radiation pressure. *Physical Review Letters* **1985**, *55*, 48–51.
40. Jones, D. J.; Diddams, S. A.; Ranka, J. K.; Stentz, A.; Windeler, R. S.; Hall, J. L.; Cundiff, S. T. Carrier-envelope phase control of femtosecond mode-locked lasers and direct optical frequency synthesis. *Science* **2000**, *288*, 635–639.
41. Zewail, A. H. Femtochemistry: Atomic-scale dynamics of the chemical bond. *The Journal of Physical Chemistry A* **2000**, *104*, 5660–5694.
42. Pawley, J. B. *Handbook of biological confocal microscopy*; 3rd ed.; Springer: New York, NY, **2006**.
43. Bacia, K.; Kim, S. A.; Schwille, P. Fluorescence cross-correlation spectroscopy in living cells. *Nature Methods* **2006**, *3*, 83–89.
44. Xu, K.; Babcock, H. P.; Zhuang, X. Dual-objective STORM reveals three-dimensional filament organization in the actin cytoskeleton. *Nature Methods* **2012**, *9*, 185–188.
45. Shear, J. B. Multiphoton-excited fluorescence in bioanalytical chemistry. *Analytical Chemistry* **1999**, *71*, 598A–605A.
46. Denk, W.; Strickler, J. H.; Webb, W. W. Two-photon laser scanning fluorescence microscopy. *Science* **1990**, *248*, 73–76.
47. Spence, D. E.; Kean, P. N.; Sibbett, W. 60-fsec pulse generation from a self-mode-locked Ti:sapphire laser. *Optics Letters* **1991**, *16*, 42–44.
48. Whitesides, G. M. The origins and the future of microfluidics. *Nature* **2006**, *442*, 368–373.
49. Paegel, B. M.; Blazej, R. G.; Mathies, R. A. Microfluidic devices for DNA sequencing: sample preparation and electrophoretic analysis. *Current Opinion in Biotechnology* **2003**, *14*, 42–50.

50. Vemuri, S.; Yu, C.-D.; Wangsatorntanakun, V.; Roosdorp, N. Large-scale production of liposomes by a microfluidizer. *Drug Development and Industrial Pharmacy* **1990**, *16*, 2243–2256.
51. Manz, A.; Graber, N.; Widmer, H. M. Miniaturized total chemical analysis systems: A novel concept for chemical sensing. *Sensors and Actuators B: Chemical* **1990**, *1*, 244–248.
52. Folch, A. *Introduction to BioMEMS*; CRC Press: Boca Raton, FL, **2013**.
53. Kane, R.; Takayama, S.; Ostuni, E.; Ingber, D. E.; Whitesides, G. M. Patterning proteins and cells using soft lithography. *Biomaterials* **1999**, *20*, 2363–2376.
54. Truskey, G. A.; Yuan, F.; Katz, D. F. *Transport phenomena in biological systems*; Pearson/Prentice Hall: Upper Saddle River, NJ, **2004**.
55. Cooksey, G. A.; Sip, C. G.; Folch, A. A multi-purpose microfluidic perfusion system with combinatorial choice of inputs, mixtures, gradient patterns, and flow rates. *Lab on a Chip* **2009**, *9*, 417–426.
56. Atencia, J.; Morrow, J.; Locascio, L. E. The microfluidic palette: A diffusive gradient generator with spatio-temporal control. *Lab on a Chip* **2009**, *9*, 2707.
57. Liao, Y.; Song, J.; Li, E.; Luo, Y.; Shen, Y.; Chen, D.; Cheng, Y.; Xu, Z.; Sugioka, K.; Midorikawa, K. Rapid prototyping of three-dimensional microfluidic mixers in glass by femtosecond laser direct writing. *Lab on a Chip* **2012**, *12*, 746.
58. Weibel, D.; Whitesides, G. Applications of microfluidics in chemical biology. *Current Opinion in Chemical Biology* **2006**, *10*, 584–591.
59. Wang, S.-J.; Saadi, W.; Lin, F.; Minh-Canh Nguyen, C.; Li Jeon, N. Differential effects of EGF gradient profiles on MDA-MB-231 breast cancer cell chemotaxis. *Experimental Cell Research* **2004**, *300*, 180–189.
60. Wang, K.; Wang, K.; Li, W.; Huang, T.; Li, R.; Wang, D.; Shen, B.; Chen, X. Characterizing breast cancer xenograft epidermal growth factor receptor expression by using near-infrared optical imaging. *Acta Radiologica* **2009**, *50*, 1095–1103.
61. Dertinger, S. K. W.; Chiu, D. T.; Jeon, N. L.; Whitesides, G. M. Generation of gradients having complex shapes using microfluidic networks. *Analytical Chemistry* **2001**, *73*, 1240–1246.
62. Kim, S.; Kim, H. J.; Jeon, N. L. Biological applications of microfluidic gradient devices. *Integrative Biology* **2010**, *2*, 584–603.

63. Postma, M.; Haastert, P. J. M. Mathematics of experimentally generated chemoattractant gradients. In *Chemotaxis*; Jin, T.; Hereld, D., Eds.; Humana Press: Totowa, NJ, **2009**; 473–488.
64. Matzer, L. Instructional Resources: Drawing with light: focus on four photographic processes. *Art Education* **2003**, *56*, 25–32.
65. Xia, Y.; Whitesides, G. M. Soft lithography. *Annual Review of Materials Science* **1998**, *28*, 153–184.
66. LaFratta, C. N.; Li, L.; Fourkas, J. T. Soft-lithographic replication of 3D microstructures with closed loops. *Proceedings of the National Academy of Sciences* **2006**, *103*, 8589–8594.
67. Spikes, J. D.; Shen, H.-R.; Kopečková, P.; Kopeček, J. Photodynamic crosslinking of proteins. III. Kinetics of the FMN- and rose bengal-sensitized photooxidation and intermolecular crosslinking of model tyrosine-containing N-(2-Hydroxypropyl)methacrylamide copolymers. *Photochemistry and Photobiology* **1999**, *70*, 130–137.
68. Shen, H.-R.; Spikes, J. D.; Kopečková, P.; Kopeček, J. Photodynamic crosslinking of proteins. I. Model studies using histidine- and lysine-containing N-(2-hydroxypropyl) methacrylamide copolymers. *Journal of Photochemistry and Photobiology B: Biology* **1996**, *34*, 203–210.
69. DeRosa, M.; Crutchley, R. J. Photosensitized singlet oxygen and its applications. *Coordination Chemistry Reviews* **2002**, *233-234*, 351–371.
70. Kaehr, B. Defining cellular microenvironments using multiphoton lithography. PhD Dissertation, University of Texas at Austin, **2007**.
71. Miller, H.; Miller, B. Photodynamic therapy of subretinal neovascularization in the monkey eye. *Archives of Ophthalmology* **1993**, *111*, 855–860.
72. Pitts, J. D.; Campagnola, P. J.; Epling, G. A.; Goodman, S. L. Submicron multiphoton free-form fabrication of proteins and polymers: Studies of reaction efficiencies and applications in sustained release. *Macromolecules* **2000**, *33*, 1514–1523.

Chapter 2: Development of a Microfluidic Device for Real-Time Manipulation of the Subcellular Chemical Environment

2.1 INTRODUCTION

Cells *in vivo* exist in a complex mixture of chemical signals that play a determining role in physiological behavior without ever entering the cell. Through signal transduction cascades [1], chemical cues (e.g., hormones, growth factors, cytokines) bind to integrated transmembrane proteins (e.g., G protein-coupled receptors [2] and receptor tyrosine kinases [3]) and initiate conformational changes in the protein triggering a series of intracellular signaling pathways that mediate a cell response (e.g., division, differentiation, and apoptosis). The type and spatial distribution of receptors across the surface of the membrane varies greatly from cell to cell [4], as well as along the length of a single cell [5]. Many types of cancer cells, for example, upregulate receptors for growth factors that lead to metastatic behavior by disabling the ability to manage receptor distribution by endocytosis [6]. Despite these variabilities, cell biologists often study cellular response by bathing an entire field of cells in an effector solution and measuring response in the form of collective or averaged behavior. While these techniques increase statistical sampling size, they also risk omitting phenotypic variation and result in a “smoothing over” of stochastic behavior [7]. For example, apparent gradual increases in the population average may instead be a result of “all-or-none” switching at a single cell level, such as the MAP kinase cascade in developing oocytes [8]. To obtain information

on the effects of low frequency variants and subcellular distinctions, techniques are required that provide greater spatial and temporal resolution for the chemical dosing of individual cultured cells.

As discussed in Chapter 1, microfluidic dosing techniques can be used to create defined laminar flow patterns within cellular microenvironments, a strategy that has been adopted for *in vitro* chemical dosing of cultured cells. For example, George Whitesides first reported a platform in 1999 [9] in which confluent microfluidic streams in a poly(dimethylsiloxane) (PDMS) microchip could be used to form steep, stable gradients of cellular effectors, an approach that was exploited to direct neutrophil chemotaxis [10] and to quantify mitochondrial redistribution by chemically dosing opposing edges of a single cell [11]. A major limitation of this approach is that the number, position, and orientation of desired dosing regions and gradients are confined by the predetermined geometry of the microfabricated device, and thus cannot be easily adjusted to accommodate the arbitrary geometries and arrangements that cultured cells assume within the device.

Despite the rise in popularity of both microfluidics [12] and laser-based techniques [13] for manipulating and studying cellular environments, there are few techniques that combine the benefits of each approach outside of cell sorting [14] and device fabrication. In 2006, Rex Nielson, a former member of the Shear Lab, developed a microfluidic device that provided spatial and temporal control over cell dosing, a system that served as the foundation for the techniques developed and presented in this dissertation. The initial cell dosing device relied on two parallel flow cells separated by a

2.5- μm -thick Mylar[®] (biaxially-oriented polyethylene terephthalate) membrane that served as the substrate for cell culture. Pores were ablated in the membrane using the output from a pulsed titanium-sapphire (Ti:S) laser focused by a 0.75 numerical aperture (NA) 40X objective. Practical and commercial applications of the technique were ultimately limited by the cost of the laser used in this study, physical properties of the membrane (e.g., instability), and the requirement for pre-fabricated pores. This chapter focuses on an adaptation of Nielson's laminar flow dosing device, using a more cost-effective microchip laser and a more biocompatible, robust membrane (polyimide) to adjust the chemical microenvironments of single cells in real time in incubated flow environments.

2.2 EXPERIMENTAL METHODS

2.2.1 Device Design

The device for all studies discussed in this chapter consisted of two distinct, linear flow cells separated by a 7.6- μm -thick polyimide film (Kapton 30HN, DuPont). Cells were cultured on one side of the membrane and were supplied with media by the corresponding flow cell. On the opposite side of the membrane, a reagent flow cell carried a steady stream of effector solution that could only be presented to the cells via pores that were ablated through the membrane using a focused laser beam. Flow directions in each chamber were positioned in opposing directions to ensure that dosing streams could be differentiated from incidental media backflow into the reagent flow cell. Both flow cells (Grace Bio-Labs, 440889B) measured 31-mm long, 2.5-mm wide, and

0.12-mm tall (9.3 μ L volume), and served to regulate uni-directional flow from inlet to outlet. Inlet and outlet ports were mated to their respective supply tubes via press fit tubing connectors (Grace Bio-Labs, 460003). Flow was controlled by two programmable digital syringe pumps (Stoelting 53130, Braintree Scientific BS-9000, and New Era NE-300/NE-1600) through platinum-cured silicone tubing (Cole-Parmer, 95802-01). Either of the flow cells could be oriented as the bottom flow cell provided the working distance of the objective was sufficient to focus through the bulk solution in the flow chamber. For all cell culture experiments, the device was initially configured such that cells injected into the cell culture flow chamber could settle on the surface of the polyimide membrane (i.e., culture flow cell on top, reagent flow cell on bottom). Once the cells had adhered to the polyimide membrane, the entire device could be operated with either flow cell on top. For fluorescent dye dosing experiments, background fluorescence from the bulk reagent flow was reduced by orienting the reagent flow cell on the top side (i.e. more distant from the objective).

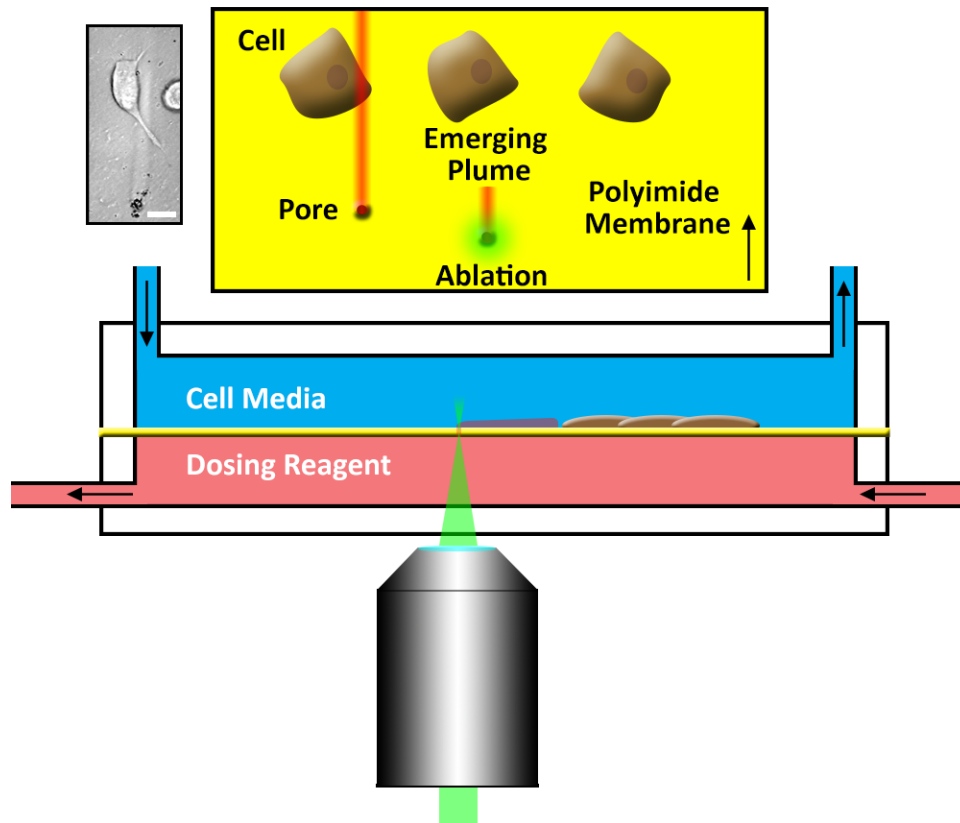


Figure 2.1: Microfluidic dosing device. A 7.6- μm -thick polyimide membrane (yellow) served as a substrate for cell culture within a steady flow of cell media (blue) isolating the cells from dosing reagent flow (pink) beneath the surface. A laser beam (green) focused through the imaging objective was used for site-specific ablation of the membrane, resulting in a small pore in the polyimide film. This pore served as a conduit to introduce narrow ($\sim 20\ \mu\text{m}$) dosing regions into the cell media flow at user-defined positions for subcellular targeting. (Top) A graphical view from above the membrane showing an existing stream dosing the edge of the leftmost cell, a new pore being ablated in the membrane and creating an emerging stream to dose the middle cell, and a completely undosed cell on the right. Arrows denote flow direction. (Inset, top left) An experimental demonstration of the graphic. The edge of a single NG108-15 cell is dosed by a stream of 5% BSA in HBS buffer. Scale bar = $20\ \mu\text{m}$.

To assemble the device, a 10-cm \times 10-cm section of polyimide membrane was stretched taut using an 8-cm aluminum spring tension hoop that provided approximately

equal tension from all directions. The membrane was then attached via double-sided adhesive tape to a 6-cm by 6-cm plastic (polyoxymethylene) frame that was machined with inlets for tubing to mate with each respective flow cell. To maintain tension, a second frame was attached to the opposite side of the membrane through a set of screws at each corner creating a sandwich around the polyimide film that held the membrane flat (Figure 2.2). The membrane was then cleaned and sterilized with 70% ethanol and a 15-minute exposure to UV light in a sterile cell culture fume hood. Flow cells were then adhered to the top and bottom of the polyimide film by their self-adhesive side creating two flow chambers separated only by the membrane.

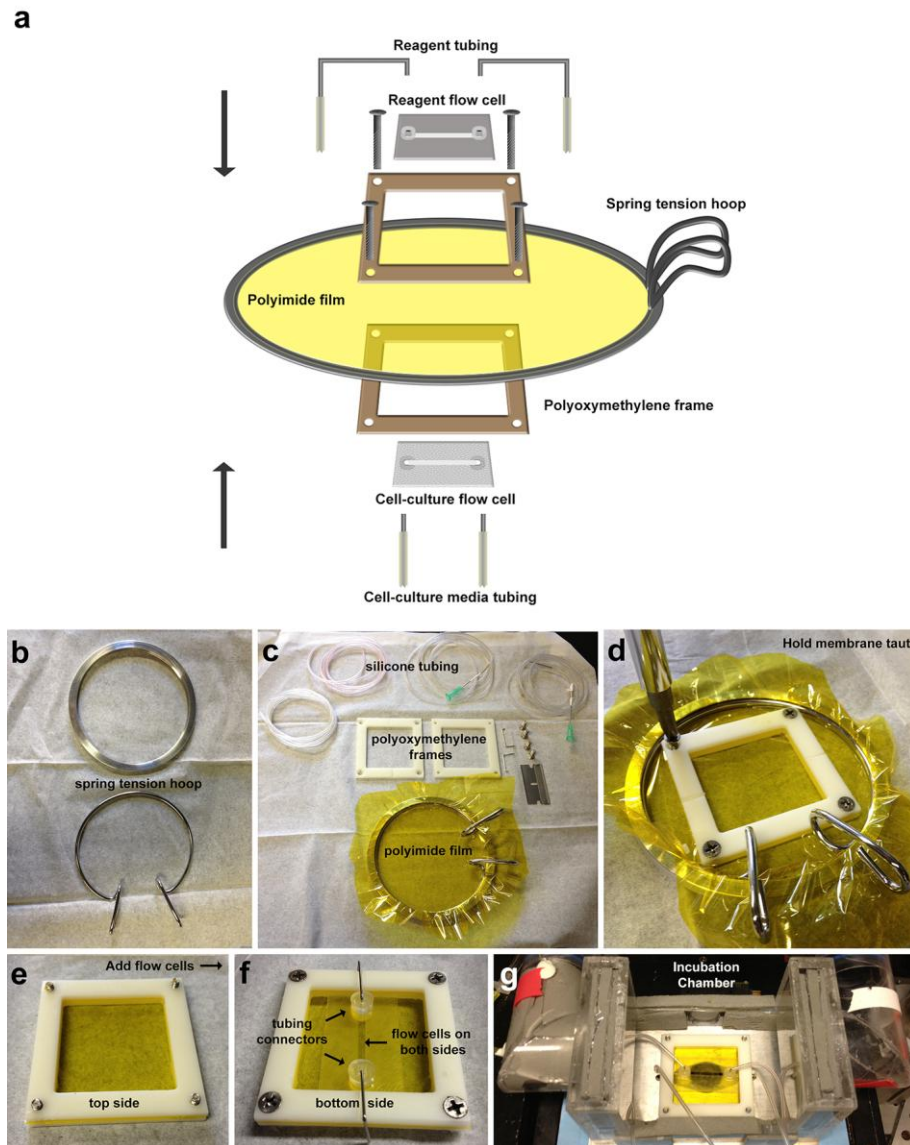


Figure 2.2: Microfluidic device assembly. (a) Polyimide film is held taut by a spring tension hoop while support frames and flow cells are attached to each side of the membrane. (b) The 8-cm aluminum spring tension hoop used to hold the polyimide membrane taut during assembly. (c) The individual components of the microfluidic device. (d) The polyoxymethylene frames were connected by a set of four screws. (e) The spring tension hoop was removed. The polyimide membrane was held taut by the adjoined polyoxymethylene frames. (f) The flow cells and tubing connectors were attached to the polyimide membrane. (g) The microfluidic cell-dosing device was placed inside an incubation chamber on an inverted microscope.

To prepare the flow device for cell culture, one side of the polyimide membrane was soaked with 1.0 mg mL^{-1} rat-tail collagen (BD Biosciences, 354249) in a 30% ethanol/70% water (v/v) mixture overnight by overfilling the fully constructed cell-culture flow chamber. After overnight exposure to collagen, the flow cell was then rinsed with Leibovitz (L-15) media (HyClone, SH30525) and cells were deposited on the surface by overfilling the flow cell with a concentrated solution of cells ($\sim 10^5 \text{ cells mL}^{-1}$) in 1% fetal bovine serum (FBS) L-15 or Dulbecco's modification of Eagle's media (DMEM) (see **2.2.3 Cell Culture**). The entire device was then placed in a cell incubator (0% CO_2 for L-15; 5% CO_2 for DMEM) for 1-2 hours to promote cell attachment. Once a sufficient number of cells had attached to the membrane, the entire flow device was transferred to the microscope and a slow-flowing solution (0.01 mL min^{-1} , average linear flow = 0.4 mm s^{-1}) of media (L-15, DMEM, or HEPES (4-(2-hydroxyethyl)-1-piperazineethanesulfonic acid) buffered saline (HBS)) was flowed over the cells to wash away any remaining free-floating or loosely attached cells. Reagent solutions and their respective tubing were then attached to the reagent flow-cell inlets and flow was initiated at a rate of 0.1 mL min^{-1} for each solution. Once the solution flow had been established on both sides of the membrane, ablations were performed (see **2.2.2 Laser Ablation Parameters**) at specific positions upstream from cells of interest and flow rates were adjusted to fit the desired stream diameter. For most experiments, a flow rate of $0.02\text{-}0.2 \text{ mL min}^{-1}$ within the cell culture flow chamber was found to be optimal for targeting cells, with faster flow rates providing narrower stream diameters within the flow. Flow rates ranging from 0.05 to 0.5 mL min^{-1} in the opposite direction to media flow were used in

the reagent flow cell to easily differentiate streams that may inadvertently arise from media flowing into the reagent flow chamber. As long as the flow rate in the reagent flow cell was greater than the flow rate in the cell-culture flow cell, a positive pressure differential drove reagent solution through individual pores and into the cell-culture flow environment.

2.2.2 Laser Ablation Parameters

Ablation was achieved using a Q-switched frequency-doubled (532 nm) Nd:YAG laser (JDS Uniphase) with an average power output of ~25 mW, a pulse width of ~600 ps, and a repetition rate of 7.65 kHz. The beam was expanded and collimated prior to the back aperture of a 40X objective (Olympus UPlanFl 0.75 NA) situated on a Zeiss Axiovert 135 inverted microscope. Average power, measured just before the back aperture of the objective, was tuned to 5-15 mW by a half-wave plate/polarizing beam splitter pair. A Uniblitz UHS1 shutter (Vincent Associates, VMM-T1) was used to control exposure of the laser, and was set to provide 2-10 10-ms pulses with a 50-ms delay between exposures. This pulsing sequence was sufficient for ablating material in the focal volume of the laser while allowing sufficient time for heat to dissipate in solution (minimizing melting at the surface and damage to adjacent cells). Additionally, pulsing provided shockwaves that served to dislodge bubbles that may have been formed during the first pulse and had become adhered to the lip of the pore.

2.2.3 Cell Culture

Mouse neuroblastoma-rat glioma (NG108-15) hybrid cells were originally purchased from the American Type Culture Collection (ATCC) and stored in their

normal growth media supplemented with 5% (v/v) dimethyl sulfoxide (DMSO) at concentrations of approximately 500,000 cells mL⁻¹ in liquid nitrogen until they were needed for culture. When thawed, cells were cultured in DMEM supplemented with 10% (v/v) fetal bovine serum (HyClone, AVJ82746), 1% (v/v) Penicillin/Streptomycin (MP Biomedicals), and 1X HAT (1.0 × 10⁻⁴ M hypoxanthine, 2.0 × 10⁻⁷ M aminopterin, 1.6 × 10⁻⁴ M thymidine; Corning Cellgro). Flasks were maintained at 37°C in a 5% CO₂ atmosphere at 100% relative humidity with media replacement every two days. The cells were passaged at a 1:4 ratio (cell solution: fresh media) to a new flask every 4-5 days, depending on confluence, up to 40 total passages. Prior to loading into the flow device, cells were passaged from a confluent flask with a 2-minute exposure to 1X Trypsin EDTA (MediaTech), which was quenched with 5 mL of DMEM. Cells were removed from the flask and centrifuged for 3 minutes at a relative centrifugal force (RCF) of 150 g. The supernatant was then removed and replaced with Leibovitz (L-15) media at a volume to concentrate the cells to approximately 100,000 cells mL⁻¹, as determined by hemocytometer counting. At a flow cell volume of 0.009 mL, this resulted in ~900 total cells within the flow chamber, corresponding to ~15 cells mm⁻² when settled.

2.2.4 Microscopy

Both fluorescence and brightfield images were acquired using a Zeiss Axiovert 135 inverted microscope with either a 10X (Zeiss Fluar 0.5 NA), 20X (Zeiss Plan-Neofluar 0.5 NA), or 40X (Olympus UPlanFl 0.75 NA) objective with a Hamamatsu Orca II CCD camera (C4742-98) controlled by MetaMorph Imaging Software (Molecular Devices). Fluorescence images required the use of a Zeiss HBO 100

mercury arc lamp and a three-position fluorescence slider module equipped with both green and red filter sets. Image processing was performed using MetaMorph (Molecular Devices, Downingtown, PA) and ImageJ (National Institutes of Health, Bethesda, MD). Video rate (30 frames s⁻¹) images were acquired with a video CCD (KP-M1U, Hitachi Denshi, Japan) controlled with Sony Giga Pocket software.

Scanning electron microscopy (SEM) images were acquired using a Zeiss Supra 40VP scanning electron microscope. Samples were prepared by removing the flow cell (if necessary) by soaking in acetone, followed by subsequent rinsing with 100% MeOH and 100% EtOH. The film was dried and attached to a SEM post by the carbon adhesive tab and conducting silver dag paint. Samples were coated with Pt/Pd to a nominal thickness of 4.5 nm prior to imaging.

Atomic force microscopy (AFM) data was collected on an Asylum MFD-3D-BIO AFM operating in an intermittent tapping mode with a super sharp improved super cone tip (Team Nanotec, Germany). Polyimide film samples for AFM were adhered to 1-mm thick glass microscope slides (12-544-4; Fisher Scientific) by hot-melt thermoplastic adhesive (DT-20; FPC Corporation, Wauconda, IL).

2.2.5 Chemicals

MitoTracker Green FM (M7514) and MitoTracker Red CMXRos (M7512) were purchased from Molecular Probes (Eugene, OR). Fluorescein (11924) was purchased from Acros Organics (Belgium). Rhodamine B (A13572) was purchased from Alfa Aesar (Ward Hill, MA). Bovine serum albumin (BSA; BAH64) was purchased from Equitech-Bio (Kerrville, TX). HEPES-buffered saline (HBS buffer) was prepared from

140 mM NaCl (S271), 5 mM KCl (P330), 750 μ M Na₂HPO₄·7H₂O (S373), 6 mM C₆H₁₂O₆ (dextrose; D14), and 25 mM 4-(2-hydroxyethyl)-1-piperazineethanesulfonic acid (HEPES; BP310) in 18.2 M Ω water and adjusted to pH 7.1. All HBS buffer reagents were purchased from Thermo Fisher Scientific (Hampton, NH).

2.2.6 Environmental Chamber

To assess the long-term effects of cell dosing in the microfluidic dosing device, an environmental chamber capable of maintaining temperature, CO₂ composition, and relative humidity was constructed to enclose the flow device. Cells at temperatures significantly below their culturing temperature (37 °C) almost immediately exhibit changes in behavior and morphology that complicate the assessment of dosing effects. Additionally, cell culture in ambient conditions precludes the use of carbonate-buffered media that require elevated levels of CO₂ to maintain an appropriate pH. Despite the deleterious effects on cultured cells of ambient conditions, previous demonstrations have been conducted under such experimental conditions [15,16].

Since commercially produced environmental control chambers are prohibitively expensive (~\$20,000), a simple environmental chamber was constructed on site at ~10% the cost. The chamber measured 14-cm wide by 9-cm deep by 2.5-cm tall and was constructed from 6.3-mm plexiglass with a 1.6-mm-thick aluminum base serving as both the floor of the environmental chamber and the fitting to match the microscope stage insert. The environmental chamber had two components that operated simultaneously to control temperature. The first was the heating element and fan obtained from a heat gun (Westward, 4HWK1) that warmed ambient air and forced it through ~1 m of

3.8-cm-diameter polyethylene tubing into a small port added to the top of the environmental chamber. The end of the tubing was equipped with a thermocouple that monitored the air temperature in real time at the inlet of the chamber and communicated through a PID controller (Red Lion, T1620000) back to the heating element to maintain the temperature at a set point determined by the user. At the outlet of the chamber, air was cycled back to the heating element via ~1 m of polyethylene tubing. The environmental chamber sat atop a heated stage insert (Brook Industries) set to 37°C that helped stabilize the air temperature of the chamber and minimized heat loss through the microscope stage. Relative humidity was increased by a bubbler line that fed directly into the heated air inlet, in addition to a collection of water dishes adjacent to the heater and within the environmental chamber. The chamber was also equipped with a CO₂ sensor (GSS, Cozir) that communicated with a separate PID controller to modulate a solenoid valve connected to a steady flow of CO₂. This sensor and CO₂ line were only operational for experiments using a carbonate-based buffer (e.g., DMEM). At a set point of 41°C, the environmental chamber reached 35°C and a relative humidity of 45% in less than 10 minutes and maintained those conditions, provided all humidity dishes were more than half full.

2.3 RESULTS AND DISCUSSION

2.3.1 Cell Culture on Polyimide Film

Initial demonstrations of the microfluidic flow cell dosing device presented in this dissertation used a 2.5- μm -thick Mylar[®] film as the membrane separating the reagent and cell culture flow channels [14]. Mylar[®] film suffers from two primary drawbacks in this

system. The first is that when these films are incorporated within a flow device, the membrane flexes under flow conditions, causing the cell culture surface to oscillate in and out of the imaging plane. This instability makes both ablation of the membrane and imaging of dosing streams and cells on the membrane difficult. Additionally, while cells can be cultured on Mylar[®] film with proper preparation (e.g., protein coating, plasma etching), levels of cell attachment, differentiation, and motility are significantly reduced compared to cultured cells on borosilicate glass and culture plastic. In an effort to address these issues, a more appropriate polymer film was sought that would provide superior properties in a microfluidic laser-ablation dosing device compared to Mylar[®] film.

The biocompatibility of polyimide film has been previously demonstrated [17], and the material has been used for microelectrode arrays in implants [18]. Additionally, the elastic modulus of polyimide (~2.5 GPa) is ~25% less than Mylar[®] film at physiological temperatures (~37°C) [19]. While it is known that neurite extension and branching are enhanced in neurons on low-stiffness gels [20], these effects have not been studied in the GPa ranges of these polymer films. To examine the suitability of polyimide film for these purposes, NG108-15 cells were cultured on sections of 7.6- μm -thick polyimide film. In these experiments, the polyimide film was sectioned into ~1 mm² squares and adhered to a series of 3.5-cm petri dishes with hot-melt thermoplastic adhesive. The polyimide film strips were then coated overnight with 50 $\mu\text{g mL}^{-1}$ rat-tail collagen (type I) in 0.02 M acetic acid. After removal of the collagen solution, cells were plated at a density of ~50,000 cells mL⁻¹ in a low-serum media (1% fetal bovine serum in DMEM) to induce serum-starved differentiation and cultured at 37°C in a 5% CO₂

incubator. Media was replaced once every three days and cells were examined at that time. After three days, cells were well-adhered to the surface and exhibited differentiated behavior (e.g., polarization, neuritic outgrowth). After nine days, cells remained well-adhered to the surface, with many neurites extending greater than 100 μm in length (Figure 2.3). Similar experiments using 2.5- μm -thick Mylar[®] resulted in a large number of cells exhibiting rounded morphology on the surface with very little differentiation, indicating a lower affinity for the surface and providing fewer features for demonstrations of site-specific dosing.

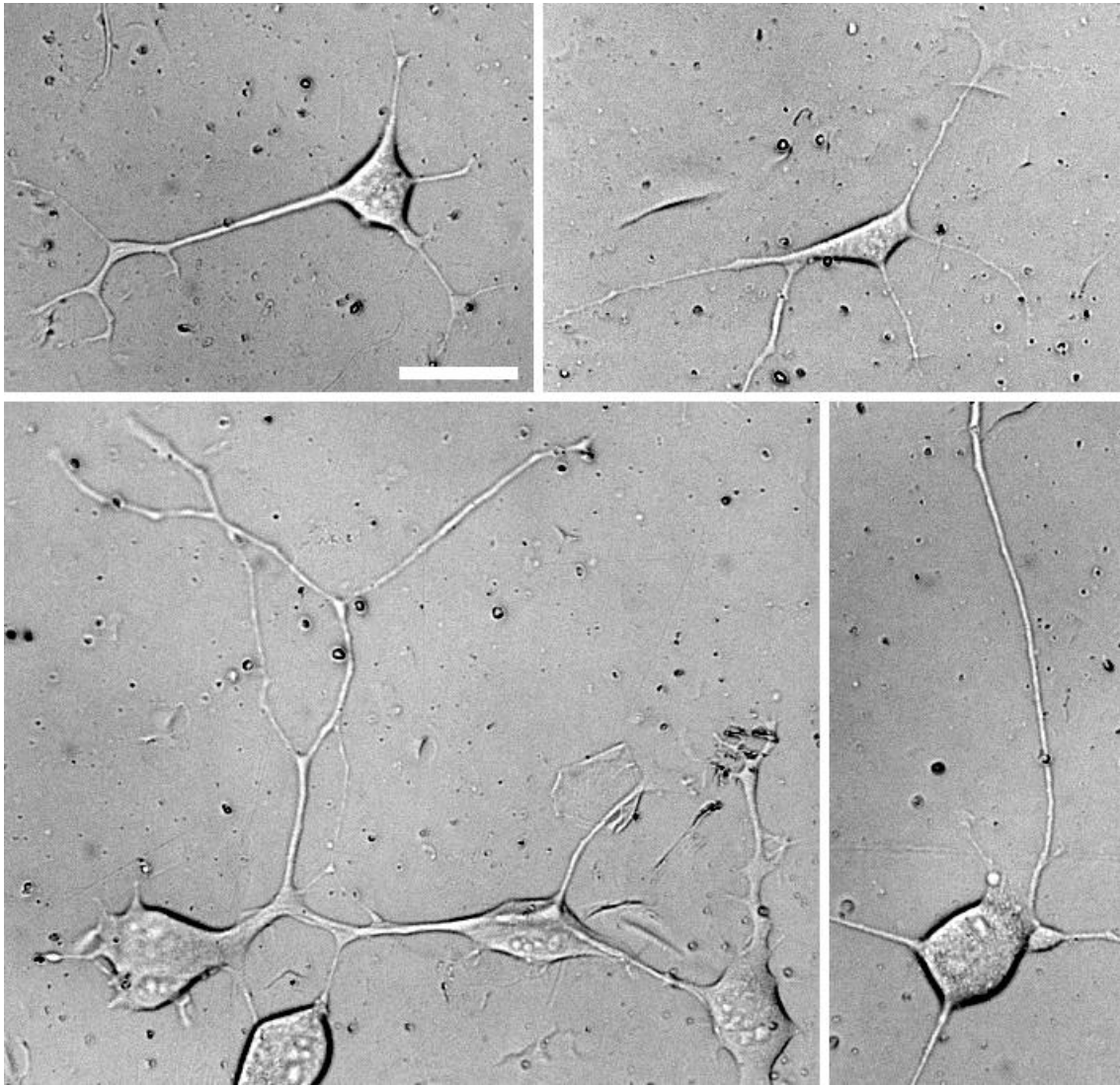


Figure 2.3: Cell culture on polyimide film. Mouse neuroblastoma-rat glioma hybrid (NG108-15) cells cultured for 9 days on 7.6- μm -thick polyimide film (coated with 50 $\mu\text{g mL}^{-1}$ rat-tail collagen). Neurites grew up to hundreds of micrometers in length over this time frame. Scale bar = 50 μm (applies to all images).

2.3.2 Laser Ablation of Polyimide Film

In parallel with cell culture studies on polyimide, the ablation characteristics of the film were examined to determine its suitability within the microfluidic laser-ablation

cell dosing device. Despite the fact that polyimide absorbance decreases significantly above 400 nm (~90% transmittance at 500 nm), pores can be created within the film with both Nd:YAG (532 nm) and Ti:S (740 nm) pulsed sources, suggesting a multiphoton process is involved. Laser ablation of polyimide is likely a combination of photochemical and photothermal mechanisms [21], where temperatures at the ablation site can momentarily exceed 500 K, even at a polymer-liquid interface [22], and fully dissipate in less than 50 μ s [23]. This process leads to significant and rapid heating in a stress-confined region around the ablation site creating spallation of material and considerable melting around the edge of the pore. These effects are visible in SEM micrographs, as well as in brightfield imaging where a dark edge around the pore is visualized, indicating a greater amount of material.

Initial investigations showed that when irradiated with average powers greater than ~8 mW with the Nd:YAG laser, ablation pores could be created with good reproducibility in the polyimide film that generated dosing streams at the introduction of flow. The characteristics of these pores were further examined using scanning electron microscopy. In these experiments, a series of pores were created in dry polyimide film at powers of 3 mW, 6 mW, 9 mW, and 12 mW (measured at the back aperture of the objective) using a 0.75 NA 40X air objective and a 0.95 NA 40X air objective, with either a single 10-ms exposure or a series of ten 10-ms exposures separated by 50 ms. The pores were examined using SEM and it was determined that for both objectives, 3 mW and 6 mW ablation powers failed to produce entire through-holes, while 9 mW and 12 mW ablation powers produced complete through-holes that were similar shape and

size for each objective. For 6 mW ablations, well-formed divets were produced on the bottom side of the membrane while the top side of the membrane showed no evidence of an ablation event. On average, the inner diameter ($\sim 2 \mu\text{m}$) of successful pores was similar to previous results obtained using Mylar[®] film as an ablation medium, but the burr formed around pores from material at the edge of ablation was significantly greater and less uniform in appearance (Figure 2.4). Pores that were ablated by a series of exposures consistently displayed less burr material surrounding the pore than a single exposure, but more material on the surface surrounding the pore was noted. Additionally, an apparent shockwave of damage to the membrane surrounding the pore was observed, likely created by thermoelastic stress waves normal to the surface [22].

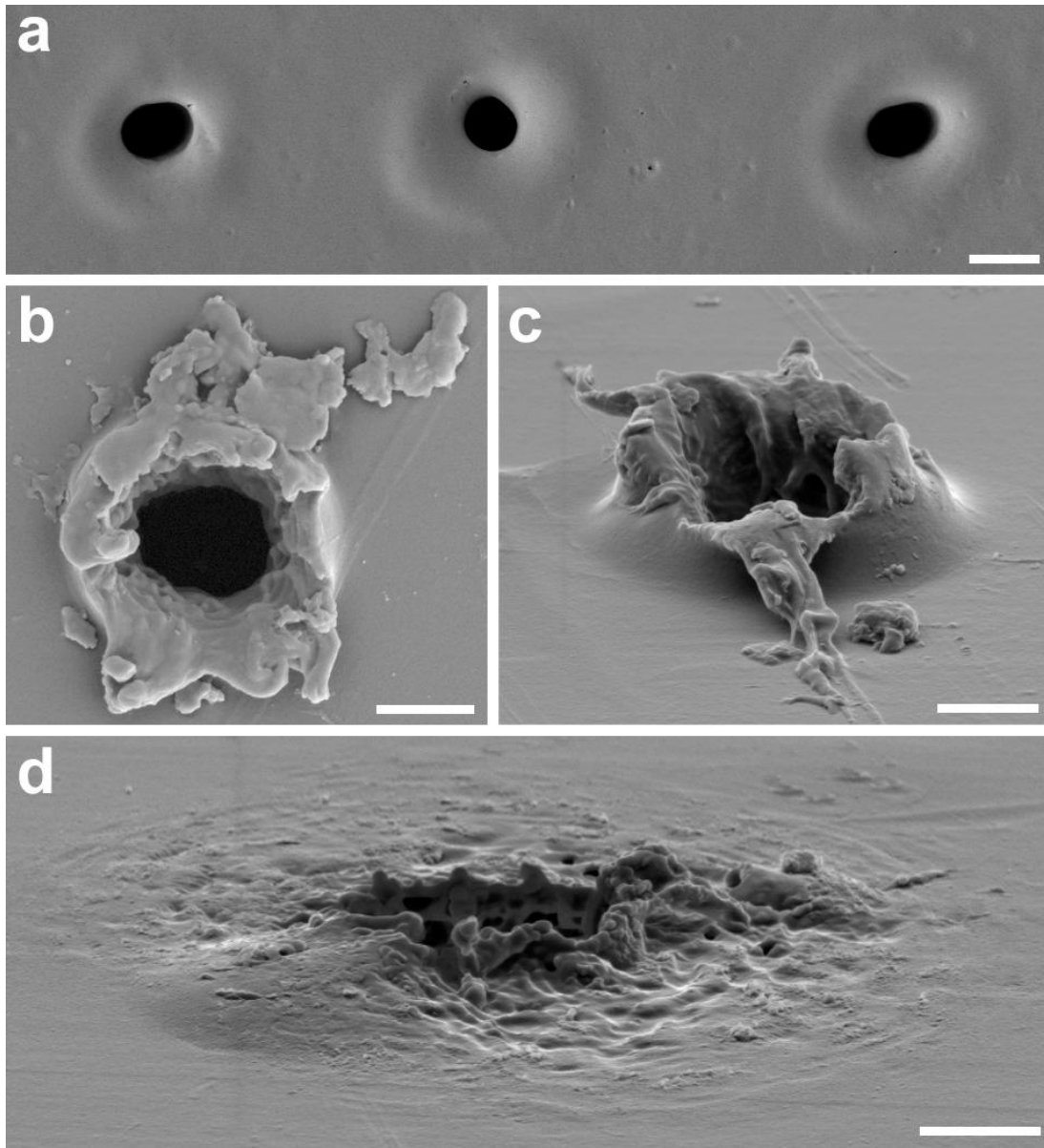


Figure 2.4: SEM of polyimide pores. The ablation characteristics of polyimide film were examined by creating a series of pores in dry polyimide film (7.6- μm -thick) at a 9 mW ablation power while varying the number of exposures with a pulsed shutter. The bottom side of the film (a) displayed little surface damage outside the ablation site and a slight oval shape at the point of ablation, while the top side of the film (b,c) showed a significant lip of ablated material rising several micrometers above the surface around the pore. This material could be partially removed by ablating a pore over a train of pulses (10 pulses, each separated by 50 ms) that resulted in more significant surface damage surrounding the pore (d). Scale bars = 2 μm .

2.3.3 Real-Time Pore Ablation

In the first demonstration of this technique, Nielson performed laser ablations in a Mylar[®] membrane with an empty reagent reservoir that was filled with dosing reagent only after pore formation because the settings for laser ablation did not produce successful pores with solution on both sides of the membrane [14]. This empty flow cell approach was not ideal for cell dosing studies because of the time delay (minutes) from ablation to emergence of the dosing stream, when a cell could move several micrometers, changing the desired dosing conditions. Additionally, subsequent dosing patterns after the initial series of ablations required that the reagent chamber be flushed with air, ablated, and re-filled with reagent solution. Initial attempts to ablate pores in both Mylar[®] and polyimide membranes with solution flowing on both sides of the membrane proved to be highly unsuccessful (<5% success rate where an ablation attempt resulted in the formation of a steady downstream stream in the cell-culture flow cell). A variety of laser settings and alignments, including changes to laser power, exposure train duration, and positioning of the focal spot on the membrane, were investigated to accommodate real-time ablation that would allow for dynamic spatial and temporal control of dosing streams, but these changes provided little to no enhancement in the success rate of stream formation.

Typically, for most multiphoton-excited processes (e.g., fluorescence), the laser beam is expanded by a series of lenses prior to being directed into the microscope objective, such that the beam overfills the back aperture of the objective providing a more even distribution of irradiance across the face of the entrance pupil of the objective. In

these cases, a diffraction-limited focal spot is achieved whose axial and radial dimensions are determined by the numerical aperture of the objective and the wavelength of the laser beam. In these laser ablation studies, however, where the purpose of the focused laser beam was to drill a small diameter (x-y dimension) pore uniformly through the thickness of the film (2.5- μm -thick Mylar[®], 7.6- μm -thick polyimide), it was not ideal to minimize the axial component of the focused laser beam. Rather, the beam was adjusted to slightly underfill (back aperture = 6.5 mm; 95% power through a pinhole = 4.9 mm) the back aperture of the objective, providing a Gaussian intensity distribution at the beam waist that sacrificed resolution relative to the diffraction-limited regime [24]. For laser drilling purposes, this Gaussian regime has proven superior because the entire intensity cross-section of the beam was used and the loss in resolution was proportionally much greater in the axial dimension than the radial dimension (~5-fold greater loss in axial resolution compared to radial resolution [24]). With these settings, pores were ablated through the membrane with solution flowing on both sides, resulting in near instantaneous stream formation after ablation (Figure 2.5).

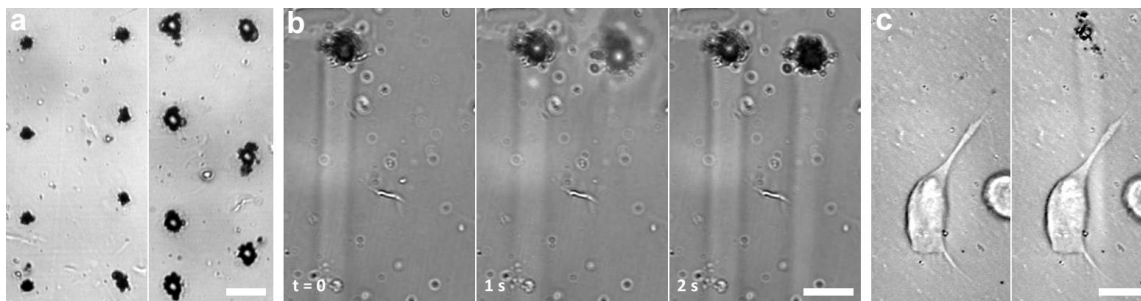


Figure 2.5: Real-time pore ablation. (a) Overfilling the back aperture of a 40X objective (at 15 mW) resulted in incomplete pore formation with solution on both sides of the membrane (left) while underfilling the same objective (at 10 mW) creates full pores (right). (b) With solution flowing on both sides of a polyimide membrane, successful pores were ablated using the underfilled regime (1 second between adjacent frames). (c) This allowed for selective, real-time targeting of cells and subcellular features (NG108-15 shown) on the membrane with dosing reagents (5% BSA shown). Scale bars = 20 μm .

In these experiments, a pulsed shutter was used to define a train of 10 mW exposures that allowed for heat to dissipate between each shuttered exposure. The pulse train contained between two and ten 10-ms pulses separated by 50 ms. In most cases, the first exposure was sufficient to ablate the membrane and subsequent exposures served to dislodge debris and/or bubbles that remained adhered to the inside of the pore. After establishing that pores could be ablated with solution flow on both sides of the membrane, a video-rate (30 fps) CCD was interfaced with the ablation microscope to observe the real-time pore formation in polyimide membrane. A series of experiments were then performed with HBS buffer in the cell-culture flow chamber and 5% (v/v) BSA in HBS buffer in the reagent chamber (Figure 2.6). Small differences in the refractive indices of both solutions (HBS buffer = 1.33, ~5% BSA solution = 1.34 at 578 nm [25]) allow for simple visualization of dosing streams by optical microscopy. As a follow-up,

similar samples were examined using SEM to observe the pore characteristics and comparisons were made to pores generated by the laser ablation of Mylar[®] membranes. These parameters (underfilled 40X 0.75 NA, 10 mW, 10-ms exposures) resulted in successful pore generation that produced a persistent stream of reagent solution with a 70% success rate for pores ablated during experimental conditions involving standard flow rates (cell-culture flow rate = 0.02-0.2 mL min⁻¹; reagent flow rate = 0.05-0.5 mL min⁻¹). The mean diameter of these pores as determined by SEM was 3.9 ± 0.9 μm (n=50).

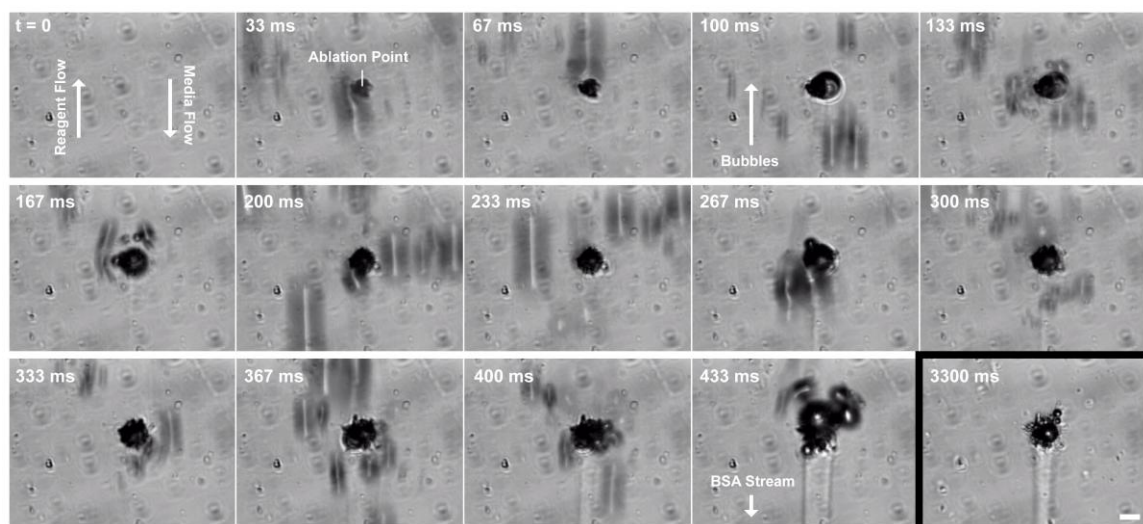


Figure 2.6: Video-rate imaging of pore formation. Video-rate imaging of the ablation of a single pore with an underfilled (10 mW before the back aperture) 0.75 NA 40X objective and 5 consecutive laser exposures lasting 10 ms each and separated by 50 ms. Flow direction in the cell-culture flow chamber is top to bottom in each image. Flow direction in the reagent flow chamber is bottom to top in each image. There was significant bubble formation with each laser exposure likely due to localized, extreme, isochoric heating. The velocity of the bubbles relative to the exposure time of the CCD results in their blurred appearance in each image. As seen in adjacent frames, the majority of bubbles were swept away in the reagent chamber (bottom to top of the image). Media flow rate = 0.1 mL min⁻¹. Reagent flow rate = 0.2 mL min⁻¹. Scale bar = 20 μm.

2.3.4 Chemical Etching of the Polyimide Membrane

While the thicker (relative to Mylar[®]) polyimide film was suitable for inclusion in a laser-ablation microfluidic dosing device, there are inherent advantages to a thinner membrane (e.g., less material to potentially occlude pores, lower powers required for ablation). Though the 7.6- μm -thick polyimide film used for these experiments is the thinnest commercially available film of its kind, there are coating techniques that allow for thinner layers of polyimide to be spread across a flat surface [26]. Unfortunately, these films are resistant to removal from their surface and difficult to handle when they are separated from a supporting structure. As an alternative, chemical etching of selected portions of the 7.6- μm -thick polyimide was explored as a technique for creating stable portions of a thinner polyimide film.

To etch the polyimide membrane, a 10-cm by 10-cm section of the film was stretched across an 8-cm tension hoop and the wrinkles were removed manually. A solution reservoir to constrict the etching region was fashioned by punching a 1-cm diameter hole from a \sim 2-cm thick block of PDMS. The perimeter of the PDMS block was trimmed to fit within the stretched region of polyimide film and the well was rinsed with deionized water followed by an ethanol rinse and then dried at 60°C for \sim 1 hour. After drying, this well was placed at the center of the stretched portion of polyimide membrane. The well was then filled with 8 M NaOH, initially at 90°C. After 10 minutes, the well was rinsed thoroughly with deionized water and a solution of room temperature 6 M HCl was added to the well for 10 minutes. The HCl was then removed and the well was rinsed

with deionized water and each step was repeated once. Following the last soak, the well was thoroughly rinsed with deionized water until solution pH in the well was approximately neutral. The PDMS reservoir was then removed from the film leaving behind an etched portion of the polyimide membrane matching the interior shape of the reservoir. These steps provided a section of polyimide film that measured $\sim 5 \mu\text{m}$ thinner than the original film as determined by AFM. Thinner films could be achieved by repeating each step for a third iteration, but the majority of these attempts resulted in the formation of holes or membrane sections that were too unstable to handle.

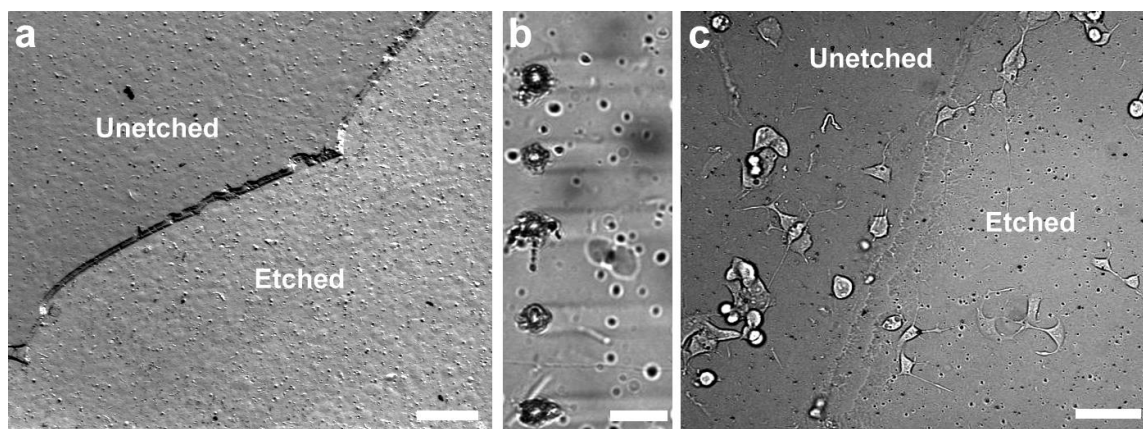


Figure 2.7: Chemically etched polyimide film. A section of $7.6\text{-}\mu\text{m}$ -thick polyimide film was chemically etched with NaOH and HCl to investigate the effects of a thinner film. (a) A 5X image of the boundary between unetched (darker, left) and etched (lighter, right) polyimide film showed a distinct cliff between segments. The difference in thickness between etched and unetched portions of the film was $\sim 5 \mu\text{m}$. Scale bar = $200 \mu\text{m}$. (b) A 40X image of pores ablated at 8 mW (measured prior to the back aperture of the objective) in etched polyimide film inside of the microfluidic flow device. Streams consisted of a 5% BSA solution (bulk flow = 0.2 mL min^{-1}) flowing into HBS buffer (bulk flow = 0.1 mL min^{-1}). Scale bar = $20 \mu\text{m}$. (c) Cells (NG108-15) cultured near the edge of etched (lighter, right) and unetched (darker, left) polyimide film. Cells displayed indistinguishable levels of surface attachment and differentiation on both surfaces. Scale bar = $100 \mu\text{m}$.

One advantage of chemically etching polyimide film to create a thinner membrane was that lower laser powers could be used to ablate pores. These lower powers created a less disruptive shockwave at the surface and produced fewer bubbles in solution. To systematically examine this effect, a range of ablation powers was examined for both etched and unetched portions of the same polyimide film. In these experiments, HBS buffer was pumped at a rate of 0.1 mL min^{-1} in the top flow cell and a solution of 5% BSA in HBS buffer was pumped at a rate of 0.2 mL min^{-1} in the opposite direction in the reagent flow cell. For each laser power setting, 50 ablation events were attempted (ten 10-ms exposures separated by 50 ms each). In these experiments, the success rate for ablation (stream formation from a single ablation attempt) on unetched portions of the polyimide film reached was less than 50% at powers below 10 mW (measured prior to the back aperture of the objective). For etched portions of the same polyimide film, the success rate reached 50% with ablation powers of 7 mW. At ablation powers of 8 mW, the success rate of ablation was 76% with an average stream diameter of $10 \text{ }\mu\text{m}$ (measured from minimum transmission to minimum transmission at the refractive edges of a 5% BSA stream in HBS buffer). On an unetched portion of the same membrane, the success rate was just 14% ($n=50$). While the standard $7.6\text{-}\mu\text{m}$ -thick polyimide film was used for the majority of experiments presented within this dissertation, future work in the area may be able to create narrower dosing streams by using the thinner, etched polyimide film as the membrane separating reagent and cell-culture flow cells.

2.3.5 Open-Top Flow

While the goal of the microfluidic laser-ablation flow device presented here was to manipulate chemical microenvironments around cells, consideration must also be given to the practical application of probing cell response to experimentally defined changes in the local chemical environment. Many of these responses can be measured through observation in optical microscopy, but there are techniques that require physical access to the cell itself, such as electrophysiology and collection of cells for polymerase chain reaction (PCR) analysis. Recent advances have provided voltage-sensitive dyes (e.g., microbial rhodopsin [27]) for measuring electrophysiological events within cells, but the majority of electrophysiologists rely on traditional patch clamping techniques that require physical access to the cell [28]. Because most microfluidic dosing devices are enclosed systems, these techniques have been slow to replace traditional puffer pipet delivery of dosing effectors that allow for patch clamping in parallel with cell dosing. For laminar flow to be maintained in an open system, the Reynolds number must be below approximately 500 (as opposed to ~2,000 for closed systems) [29], which is well above the calculated values for the microfluidic cell dosing device presented in these studies. Thus, it would be advantageous to have a system that could provide stable gradients of effectors while maintaining the ability to patch clamp the cell. Microfluidic solutions have been proposed for introducing patterned dosing streams into open wells [30], but turbulence at the microfluidic outlets leads to significant disruption in the laminarity of flow providing dosing regions that are limited to areas in close proximity to outlet ports in a pre-determined geometry. For neuronal cells, the density of γ -aminobutyric acid

(GABA, one of the primary inhibitory neurotransmitters [31]) and L-glutamate (a primary excitatory neurotransmitter [32]) receptors vary depending on the location on dendrites and the distance from the soma [33]. A technique that could specifically target these receptors with both nootropic (cognitive-enhancing) drugs and GABA or L-glutamate would provide a significant tool in understanding these processes at a single cell level [34]. While the microfluidic dosing device presented in this dissertation could easily accommodate the dosing regimes required for these studies, measuring electrophysiological response required modifications (i.e., removal of the flow chamber ceiling) that would provide physical access to the cell.

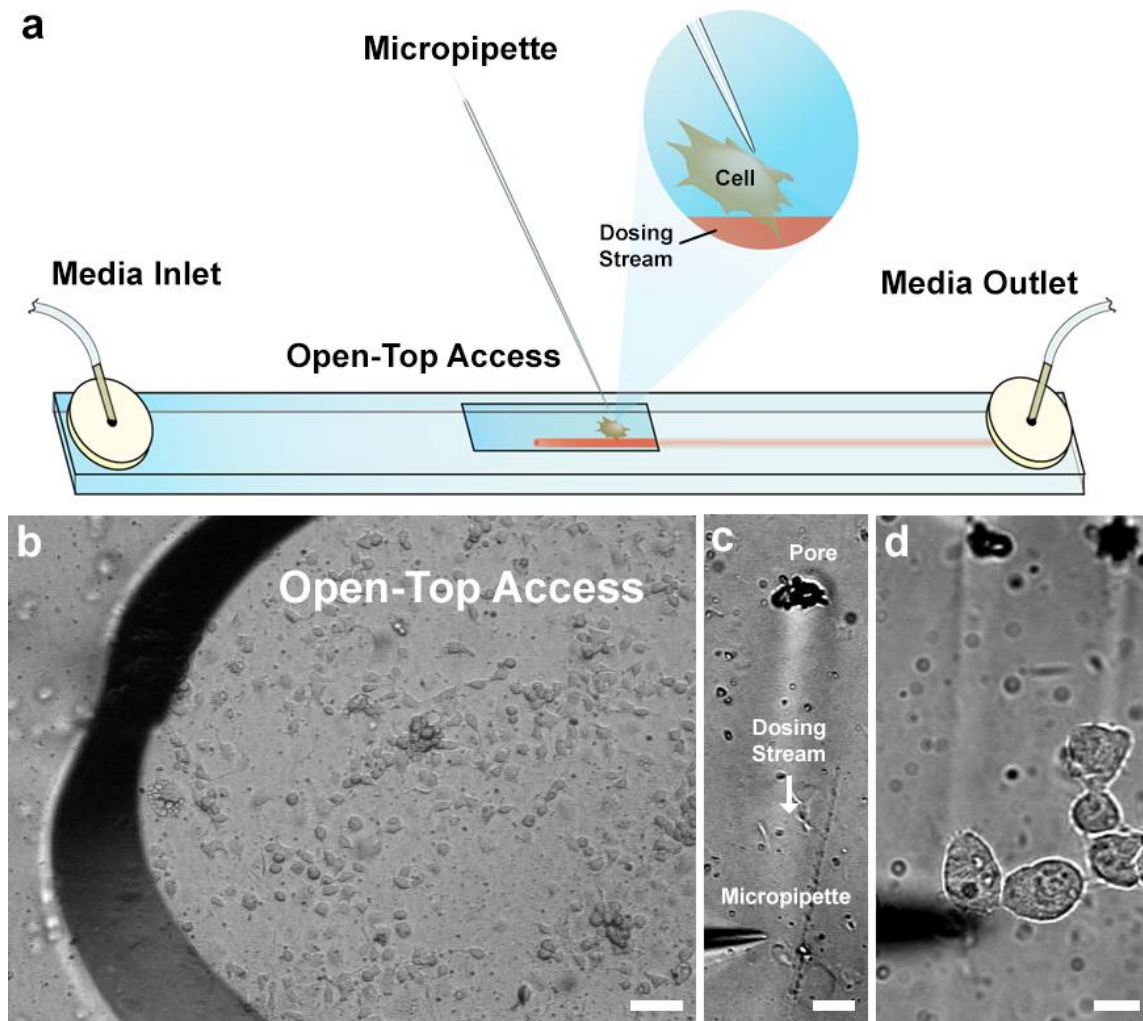


Figure 2.8: Open-top access to cells. (a) A graphic demonstrating the ability to position a micropipette near a cell within a narrow dosing stream in an open-top cell culture flow chamber. (b) An open-top flow cell was created to give physical access to cultured cells in the microfluidic cell dosing device. Image (5X magnification) shows the edge of an open-access region of a cell-culture flow cell. Scale bar = 100 μm . (c) A pulled glass pipet was positioned next to a dosing stream of 5% BSA in HBS buffer. Scale bar = 20 μm . (d) A pipet is positioned just above a cluster of cells (NG108-15), where the left edge of a single cell was dosed by a stream of 5% BSA. Scale bar = 20 μm .

As a proof of concept, a portion of the cell culture flow chamber was left open to the environment (Figure 2.8). To achieve the open-top flow cell for these experiments, a ~1 mm diameter section of the cell dosing flow chamber was removed by punching a needle through the bottom of the roof. All other conditions of the flow device remained the same, with the exception that negative pressure was applied to the outlet of the cell-culture flow cell (via syringe pump extraction) to suction solution through the outlet and prevent solution from overflowing through the open roof of the flow cell. A series of experiments was carried out where dosing streams were created and a micromanipulator was used to position glass micropipettes around these streams and adjacent to cells in dosing streams to demonstrate the physical access to cells. While large micropipettes (~50 μm) created turbulent mixing at the surface and divert dosing streams, small tapered micropipettes (~1 μm at the tip) did not significantly disrupt the flow dynamics at the surface (Figure 2.8c). Ultimately, these experiments had a much higher rate of failure when compared to the standard dosing device (particularly during cell experiments) due to leaking and introduction of bubbles that created turbulence in the flow. It should be plausible to perform patch-clamping measurements around dosed cells in the future, but these issues must be addressed before these demonstrations become feasible. As an alternative, it may be possible to construct the roof of the cell culture flow chamber from a septum that could be selectively penetrated by a sheathed, patch-clamping micropipette.

2.3.6 Single-Cell Targeting

With flow cell conditions optimized for a more cost-effective and biocompatible dosing method using a Nd:YAG laser and polyimide film, experiments were performed

to exhibit the subcellular site-specific targeting ability of the flow device. These demonstrations were performed on the standard 7.6- μm -thick polyimide film in a closed system using cell-permeable fluorescent labels. In these experiments, the goal was to demonstrate the ability of this microfluidic laser-based cell dosing device to selectively target subcellular portions of single cells with a variety of reagents. Figure 2.9 shows a series of individual cells targeted with MitoTracker[®] Red CMXRos, an x-rosamine derivative that exhibits low fluorescence until oxidized within the cell, and MitoTracker[®] Green FM, a carbocyanine-based dye with low levels of fluorescence in aqueous solution that increase substantially in the lipid environment of a cell. Dosing streams were supplemented with 5% BSA or low levels of a fluorescent dye (e.g., fluorescein, rhodamine B) to allow for visualization of the stream.

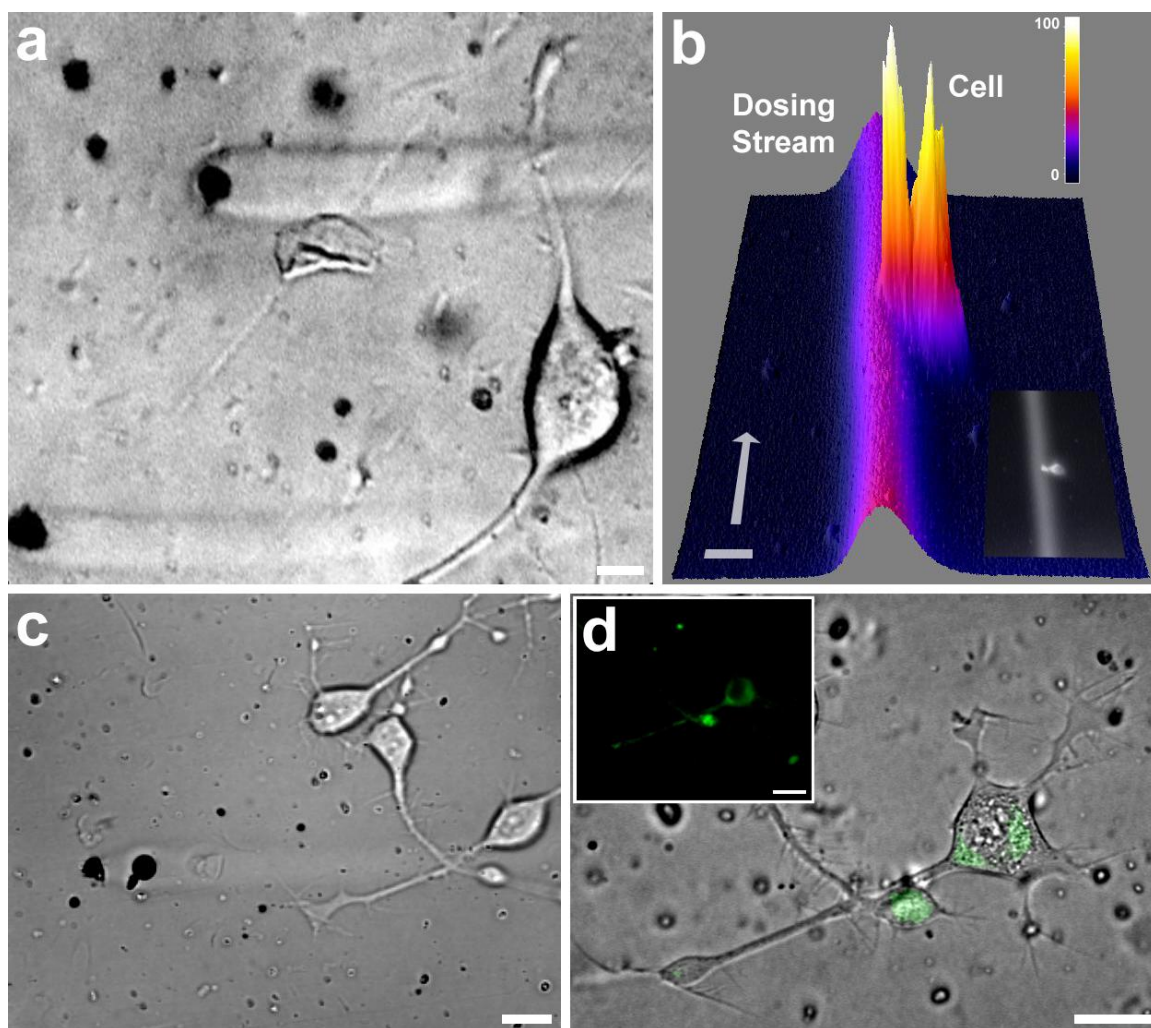


Figure 2.9: Subcellular dosing. (a) Opposing neuritic processes on a single NG108-15 cell were dosed with 5% BSA streams. Scale bar = 10 μm . (b) The edge of a single NG108-15 cell was dosed by MitoTracker Red CMXRos supplemented with 10 μM rhodamine B to visualize stream. 3D surface intensity plot shows the spike in intensity created by dye internalized by the cell. Fluorescence counts in arbitrary units indicated by color-encoded z-axis. Legend indicates fluorescence counts from minimum (0) to maximum (100) across the entire plot area. Scale bar = 20 μm . (c) Subcellular portions of adjacent cells were dosed with a solution of 5% BSA and 500 nM MitoTracker Green FM. (d) 15 minutes after dosing, a collection of mitochondria within the dosed portions of each cell remained fluorescent. Inset: Raw fluorescence image with false coloring (green) added. Scale bars = 20 μm .

2.4 CONCLUSIONS

In summary, adaptations to the microfluidic dosing device originally presented by Nielson, et al. in 2006 produced a cell dosing device that is lower cost, more biocompatible, and allowed for real-time dosing of cells. Adjustments to laser parameters provided the ability to dynamically create pores that reliably produced dosing streams in the presence of cultured cells. Wet chemical etching of the polyimide film was demonstrated for altering the thickness of membranes, a property that may be useful for creating narrowed dosing streams with lower laser powers in the future. Initial open-top flow cell geometries were also explored for providing physical access to cells during dosing experiments.

While $\sim 20\text{-}\mu\text{m}$ wide dosing streams were sufficient for demonstrating subcellular dosing with differentiated NG108-15 cells in these studies, there are many cell types (e.g., rounded epidermal cells) and cellular features (e.g., receptor clusters) smaller than these streams could specifically target. Future work in this area will focus on increasing spatial resolution of the technique by narrowing dosing stream widths. This may be achieved with smaller pore sizes and decreased material at the edge of pores, introducing less localized turbulence at the beginning of a dosing stream, or by hydrodynamic focusing to narrow the diameter of larger dosing streams. Thinner films (achieved by chemical etching) may also be used to produce pores at a lower ablation power with less potential damage to neighboring cells. Additionally, a demonstration of the capabilities of

an open-access flow system (e.g., patch clamping) would be experimentally relevant to cell biologists that would provide an alternative to puffer pipet delivery of dosing reagents.

In this chapter, the microfluidic device used for dosing was designed as two anti-parallel, unidirectional, laminar flow cells that provided both cell culture media and dosing reagents. Chapter 3 examines different geometries for the reagent flow cell and shows how these geometries can be used to provide multi-reagent dosing, controlled gradient dosing, and subsecond switching of reagents while maintaining the advantages of the microfluidic dosing device that were discussed in Chapter 2.

2.5 REFERENCES

1. Dixon, R. A.; Kobilka, B. K.; Strader, D. J.; Benovic, J. L.; Dohlman, H. G.; Frielle, T.; Bolanowski, M. A.; Bennett, C. D.; Rands, E.; Diehl, R. E.; Mumford, R. A.; Slater, E. E.; Sigal, I. S.; Caron, M. G.; Lefkowitz, R. J.; Strader, C. D. Cloning of the gene and cDNA for mammalian beta-adrenergic receptor and homology with rhodopsin. *Nature* **1986**, *321*, 75–79.
2. Mooibroek, M. J.; Wang, J. H. Integration of signal-transduction processes. *Biochemistry and Cell Biology* **1988**, *66*, 557–566.
3. Cadena, D. L.; Gill, G. N. Receptor tyrosine kinases. *The FASEB Journal*. **1992**, *6*, 2332–2337.
4. Feinerman, O.; Jentsch, G.; Tkach, K. E.; Coward, J. W.; Hathorn, M. M.; Sneddon, M. W.; Emonet, T.; Smith, K. A.; Altan-Bonnet, G. Single-cell quantification of IL-2 response by effector and regulatory T cells reveals critical plasticity in immune response. *Molecular Systems Biology* **2010**, *6*, 1–16.
5. Chen, Y.; Munteanu, A. C.; Huang, Y.-F.; Phillips, J.; Zhu, Z.; Mavros, M.; Tan, W. Mapping receptor density on live cells by using fluorescence correlation spectroscopy. *Chemistry — A European Journal* **2009**, *15*, 5327–5336.
6. Mosesson, Y.; Mills, G. B.; Yarden, Y. Derailed endocytosis: An emerging feature of cancer. *Nature Reviews Cancer* **2008**, *8*, 835–850.
7. Kilfoil, M. L.; Lasko, P.; Abouheif, E. Stochastic variation: From single cells to superorganisms. *HFSP Journal* **2009**, *3*, 379–385.
8. Ferrell, J. E., Jr; Machleder, E. M. The biochemical basis of an all-or-none cell fate switch in *Xenopus* oocytes. *Science* **1998**, *280*, 895–898.
9. Kane, R.; Takayama, S.; Ostuni, E.; Ingber, D. E.; Whitesides, G. M. Patterning proteins and cells using soft lithography. *Biomaterials* **1999**, *20*, 2363–2376.
10. Li Jeon, N.; Baskaran, H.; Dertinger, S. K. W.; Whitesides, G. M.; Van de Water, L.; Toner, M. Neutrophil chemotaxis in linear and complex gradients of interleukin-8 formed in a microfabricated device. *Nature Biotechnology* **2002**, *20*, 826–830.
11. Takayama, S.; Ostuni, E.; LeDuc, P.; Naruse, K.; Ingber, D. E.; Whitesides, G. M. Subcellular positioning of small molecules. *Nature* **2001**, *411*, 1016.
12. Young, E. W. K.; Beebe, D. J. Fundamentals of microfluidic cell culture in controlled microenvironments. *Chemical Society Reviews* **2010**, *39*, 1036–1048.
13. Brehm-Stecher, B. F.; Johnson, E. A. Single-cell microbiology: Tools, technologies, and applications. *Microbiology and Molecular Biology Reviews* **2004**, *68*, 538–559.

14. Wang, M. M.; Tu, E.; Raymond, D. E.; Yang, J. M.; Zhang, H.; Hagen, N.; Dees, B.; Mercer, E. M.; Forster, A. H.; Kariv, I.; Marchand, P. J.; Butler, W. F. Microfluidic sorting of mammalian cells by optical force switching. *Nature Biotechnology* **2004**, *23*, 83–87.
15. Nielson, R.; Shear, J. B. Parallel chemical dosing of subcellular targets. *Analytical Chemistry* **2006**, *78*, 5987–5993.
16. Moorjani, S.; Nielson, R.; Chang, X. A.; Shear, J. B. Dynamic remodeling of subcellular chemical gradients using a multi-directional flow device. *Lab on a Chip* **2010**, *10*, 2139–2146.
17. Richardson, R. R.; Miller, J. A.; Reichert, W. M. Polyimides as biomaterials: preliminary biocompatibility testing. *Biomaterials* **1993**, *14*, 627–635.
18. Seo, J.-M.; Kim, S. J.; Chung, H.; Kim, E. T.; Yu, H. G.; Yu, Y. S. Biocompatibility of polyimide microelectrode array for retinal stimulation. *Materials Science and Engineering: C* **2004**, *24*, 185–189.
19. Li, R. S.; Jiao, J. The effects of temperature and aging on Young's moduli of polymeric based flexible substrates. In IMAPS 2000: International Symposium on Microelectronics, **2000**, 68–73.
20. Georges, P. C.; Janmey, P. A. Cell type-specific response to growth on soft materials. *Journal of Applied Physiology* **2005**, *98*, 1547–1553.
21. Lippert, T. K.; Georgiou, S. *Polymers and light*; Advances in polymer science; Springer: Berlin ; New York, **2004**.
22. Elaboudi, I.; Lazare, S.; Belin, C.; Talaga, D.; Labrugère, C. Underwater excimer laser ablation of polymers. *Applied Physics A* **2008**, *92*, 743–748.
23. Dyer, P. E.; Pervolaraki, M.; Lippert, T. Experimental studies and thermal modelling of 1064- and 532-nm Nd:YVO₄ micro-laser ablation of polyimide. *Applied Physics A* **2004**, *80*, 529–536.
24. Webb, R. H. Confocal optical microscopy. *Reports on Progress in Physics* **1996**, *59*, 427–471.
25. Perlmann, G. E.; Longworth, L. G. The specific refractive increment of some purified proteins. *J. Am. Chem. Soc.* **1948**, *70*, 2719–2724.
26. Grunze, M.; Lamb, R. N. Preparation and adhesion of ultrathin polyimide films on polycrystalline silver. *Chemical Physics Letters* **1987**, *133*, 283–287.
27. Kralj, J. M.; Douglass, A. D.; Hochbaum, D. R.; Maclaurin, D.; Cohen, A. E. Optical recording of action potentials in mammalian neurons using a microbial rhodopsin. *Nature Methods* **2011**, *9*, 90–95.
28. Zhao, Y.; Inayat, S.; Dikin, D. A.; Singer, J. H.; Ruoff, R. S.; Troy, J. B. Patch clamp technique: review of the current state of the art and potential contributions

- from nanoengineering. *Proceedings of the Institution of Mechanical Engineers, Part N: Journal of Nanoengineering and Nanosystems* **2008**, *222*, 1–11.
29. Truskey, G. A.; Yuan, F.; Katz, D. F. *Transport phenomena in biological systems*; Pearson/Prentice Hall: Upper Saddle River, N.J., **2004**.
 30. Olofsson, J.; Pihl, J.; Sinclair, J.; Sahlin, E.; Karlsson, M.; Orwar, O. A microfluidics approach to the problem of creating separate solution environments accessible from macroscopic volumes. *Analytical Chemistry* **2004**, *76*, 4968–4976.
 31. Hyson, R. L.; Reyes, A. D.; Rubel, E. W. A depolarizing inhibitory response to GABA in brainstem auditory neurons of the chick. *Brain Research* **1995**, *677*, 117–126.
 32. Van den Pol, A. N.; Trombley, P. Q. Glutamate neurons in hypothalamus regulate excitatory transmission. *The Journal of Neuroscience* **1993**, *13*, 2829–2836.
 33. Craig, A. M.; Blackstone, C. D.; Haganir, R. L.; Banker, G. Selective clustering of glutamate and gamma-aminobutyric acid receptors opposite terminals releasing the corresponding neurotransmitters. *Proceedings of the National Academy of Sciences* **1994**, *91*, 12373–12377.
 34. Foster, A.; Kemp, J. Glutamate- and GABA-based CNS therapeutics. *Current Opinion in Pharmacology* **2006**, *6*, 7–17.

Chapter 3: Complex Multi-Reagent Dosing Patterns¹

3.1 INTRODUCTION

Living cells reside within anisotropic microenvironments that orchestrate a broad range of polarized responses to a complex milieu of time-varying chemical gradients that regulate processes from differentiation until cell death. In many circumstances, cells must integrate instructions from a host of cues that modulate activity in nonlinear and often conflicting fashion (e.g., neutrophil chemotaxis [1], axonal pathfinding [2], and neuronal chemotaxis [3,4]). Neurons in the central nervous system, for example, can receive numerous excitatory (glutamatergic) and inhibitory (dopaminergic) inputs along their dendritic tree that contribute differentially to the firing status of the cell [5]. Migration of immune cells is orchestrated by a range of attractive factors, including cytokines (e.g. interleukin 8 and leukotriene B4) and foreign peptides (e.g., fMet-Leu-Phe), which act through gradients that may be simultaneously presented to the surface of a leukocyte [6,7]. Neurons also rely on co-existing gradients of attractive and repulsive factors, both for migration and axonal pathfinding [8,9]. Although there has been growing realization of the influence of microscopic chemical gradients on cellular behavior [10], creating complex distributions of cellular effectors using traditional methods (e.g., diffusion in hydrogels, micropipette delivery, transwell assays) is limited by an inability to quickly

¹ Portions adapted from [40]. Hoppe performed experiments, created figures, and wrote the manuscript; Moorjani contributed to the conceptual development and performed preliminary feasibility experiments; Shear edited the manuscript and served as principal investigator for the work.

create stable gradients and manipulate concentrations with spatial and temporal control. To unravel how localized chemical signals influence complex behaviors, tools must be developed for establishing patterns of chemical gradients that vary over subcellular dimensions.

To assess effects from subcellular chemical signals systematically, various strategies have been developed for creating chemical gradients on micrometer dimensions. Micropositioned puffer pipets are commonly used to expel subnanoliter volumes of effectors near a cell membrane; [11-13] however, the physical constraints of micromanipulators limits both the number of parallel dosing sites and the speed at which a pipet can be repositioned to a new site of interest. Boyden chambers (and the more recently developed transwell assay) rely on passive diffusion through a porous membrane, and are useful for creating simple gradients and measuring migration of large numbers of cells, but they cannot be used to directly visualize these cells during migration or to create complex gradients [14]. Zigmond chambers allow for the creation of steady-state gradients around observable cells, but these gradients only last for ~1 hour and cannot be dynamically shifted after creation [15]. Whether introduced via pipet or within diffusion chambers, delivery of dosing reagents rely on diffusion of simple gradients, preventing use of these approaches for characterizing cellular responses to sustained, complex chemical gradients.

As an alternative, microfluidic systems can be used to create defined laminar flow patterns within cellular microenvironments, allowing for dynamic spatial and temporal control of chemical dosing patterns and gradients. As discussed in Chapter 2, Whitesides

and coworkers were the first to report a platform in which confluent microfluidic streams in a poly(dimethylsiloxane) (PDMS) microchip could be used to form steep, stable gradients of cellular effectors for reshaping the cytoskeleton and imaging dye uptake in single cells [16,17]. Similar microfluidic devices have since been adapted for patterning cell dosing patterns [18], defining and manipulating diffusive gradients [19], long-term cell culture [20], cell sorting [21], and dynamic repositioning of dosing streams [22].

To extend the capabilities of laminar flow systems for *in vitro* chemical dosing, Chapter 2 presented a stacked laminar flow system based on technical improvements to a previously reported microfluidic cell dosing device [23] in which a dosing reagent is separated from a cell culture region by a thin polyimide membrane that can be ablated at user-defined positions using the focused output of a pulsed laser. Ablation pores serve as conduits for reagent entry into the cell-culture environment, where laminar-flow conditions result in the formation of well-defined dosing streams that can extend for up to hundreds of micrometers with minimal diffusion. A given stream diameter depends on the size of a pore, the solution flow rate, and how far the stream has traveled from its inception at a pore. Optimization of these parameters allows targets to be dosed over regions as small as 10 μm . By incorporating a means to rotate flow directionality within the cell culture region, it is possible to re-orient dosing streams, and hence, chemical gradients, with millisecond resolution [24].

A defining limitation of this approach is its reliance on a single reservoir to supply all pores with the same dosing reagent. While this design principle provides great flexibility for multi-site dosing, many applications require the ability to dose cells with

different reagents at well-defined subcellular positions (e.g, receptor targeting, chemotactic hierarchies). Multi-reagent dosing opens the possibility for studies aimed at quantifying proximity effects of multiple synergistic or competing cues for processes such as membrane depolarization or for tracking redistribution of subcellular organelle populations (e.g., vesicle pools).

This chapter reports a strategy for generating multiple reagent streams within cell-culture environments that can deliver distinct dosing species to different, targeted subcellular regions. This approach can be used to maintain steep, stable gradients for hours or longer, or, alternatively, produce streams whose composition can be modified on sub-second time scales.

3.2 EXPERIMENTAL

3.2.1 Flow Device Design and Assembly

The dosing system used in these studies (Figure 3.1) consisted of two distinct flow cells separated by a 7.6- μm -thick polyimide membrane (Kapton 30HN, DuPont). The dosing (cell-culture) flow chamber, obtained from Grace Bio-Labs (440889B) has dimensions of 32 mm (length) \times 2.5 mm (width) \times 0.12 mm (height), and is provided with Secure-Seal adhesive (Grace Bio-Labs, SA-S-1L) for affixing the chamber to a substrate to define the final boundary of the flow environment. The reagent flow chamber is fabricated from 0.12-mm thick sheets of Secure-Seal adhesive using a 60-W CO₂ laser cutter (Universal Laser Systems, X-660) to have multiple inlet channels measuring 1.5-mm wide and 10-mm long converging to a single confluent channel measuring

1.5-mm wide and 19-mm long. The adhesive is then attached to a polycarbonate coverslip that is drilled with corresponding 2-mm diameter inlet ports leading to a single outlet at the respective ends of the flow cell. Inlet and outlet ports are mated to supply and drain tubes, respectively, via press-fit tubing connectors (Grace Bio-Labs, 460003). Flow is controlled using a pair of programmable digital syringe pumps (Stoelting 53130, Braintree Scientific BS-9000, and New Era NE-300/NE-1600) connected to flow-cell inlets through platinum-cured silicone tubing (Cole-Parmer, 95802-01). For all experiments presented in this chapter, the reagent flow cell is situated above the polyimide membrane. In the case of cell-culture studies, cells were loaded with the stacked flow cells inverted to allow adequate adhesion to the membrane, before flipping the device into its normal orientation.

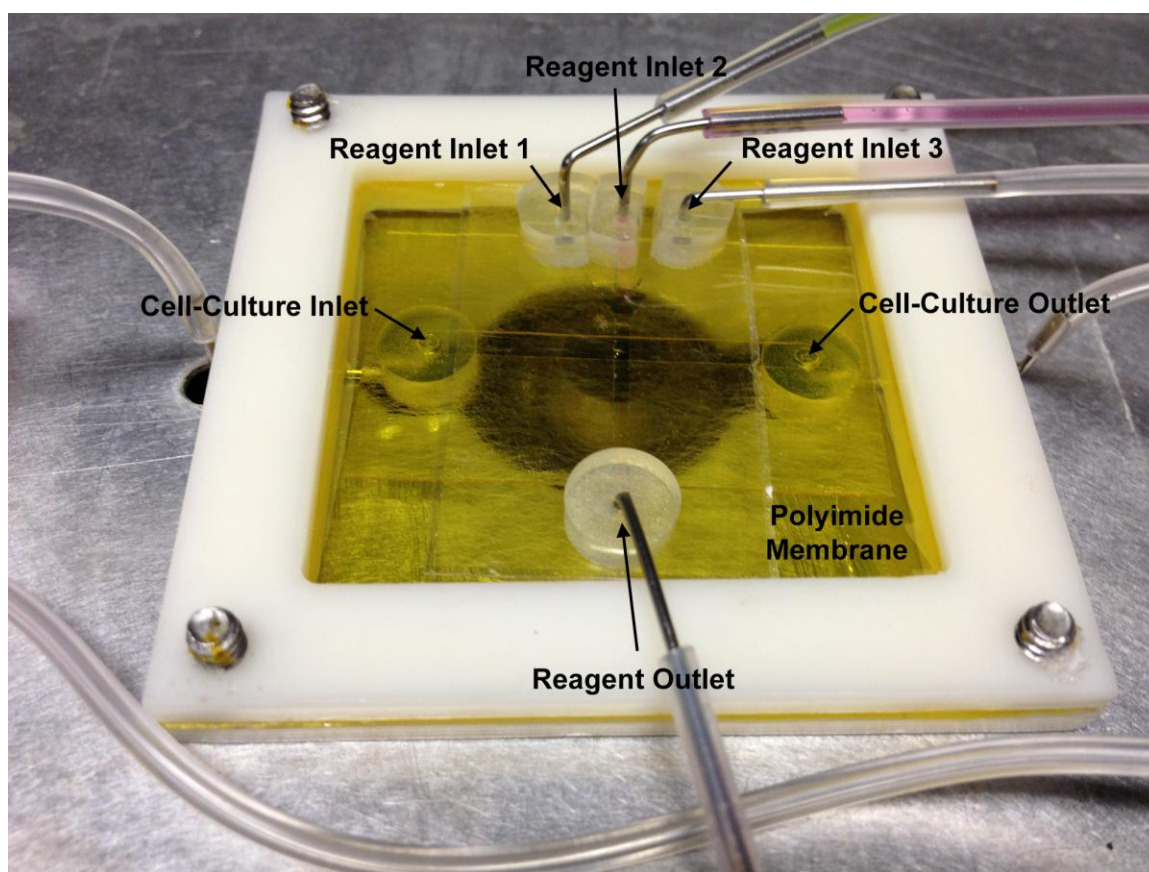


Figure 3.1: Fully assembled flow device. Polyimide membrane (yellow) is sandwiched between two support frames holding the membrane taut. The cell-culture flow cell is placed beneath the membrane and runs left to right in the image while the reagent flow cell contains three separate inlets and lies above the membrane flowing from top to bottom in the image. The reagent inlets are flowing fluorescein (Inlet 1), rhodamine B (Inlet 2), and buffer (Inlet 3). The intersection of cell culture and reagent flow cells is positioned just above the ablation/imaging objective (center).

In the initial step of assembling the device, the polyimide membrane was stretched taut using an 8-cm-diameter aluminum spring-tension hoop that provided approximately equal tension from all directions. The membrane was then attached via double-sided adhesive tape to a 6 cm \times 6 cm plastic (polyoxymethylene) frame. To maintain tension, a second frame was attached to the opposite side of the membrane

through a set of screws at each corner, creating a sandwich around the polyimide membrane that held the membrane flat and taut. The membrane was then cleaned and sterilized using a swipe of 70% ethanol and a 15-minute exposure to UV light in a cell-culture hood. Flow cells were then adhered to both sides of the polyimide membrane.

For cell dosing studies, the cell culture side of the membrane was soaked with 1.0 mg mL^{-1} rat-tail collagen (BD Biosciences, 354249), prepared in a 30% ethanol/70% water (v/v) mixture, overnight by overfilling the fully constructed cell-culture flow cell chamber. After overnight exposure to collagen, this flow cell was then rinsed with Leibovitz (L-15) medium (HyClone, SH30525) and cells were deposited on the surface by overfilling the flow cell with a concentrated solution of cells in L-15 medium (see **3.2.3 Cell Culture**). The entire device was then placed in a home-built incubation chamber (see **2.2.6 Environmental Chamber**) on the microscope stage that was set to maintain cell temperatures at 34-35 °C and ~45% relative humidity. Attachment and general appearance of cells were monitored for ~1 h, then L-15 medium was gently flowed over the cells (0.01 mL min^{-1} , corresponding to an average linear flow velocity of 0.5 mm s^{-1}), which washed away remaining free-floating or loosely attached cells.

After filling the reagent flow cell (typically at an initial rate of 0.1 mL min^{-1} for each solution), pores were ablated in the polyimide membrane using a focused Q-switched Nd:YAG laser beam and flow rates were adjusted to produce desired stream characteristics (width, composition, and concentration). For all studies, solution was delivered at 0.10 mL min^{-1} within the cell culture chamber. Total initial flow rates ranging from $0.20\text{-}0.60 \text{ mL min}^{-1}$ were used in the reagent flow cell, with the overall rate

affecting both the pressure within the reagent channel (which must be sufficient to drive solution through pores into the cell culture channel) and the width of reagent boundaries. In three-component reagent flow cells, the initial overall flow rate was 0.6 mL min^{-1} , with a constant HEPES-buffered saline (HBS buffer) flow rate of 0.3 mL min^{-1} . In five-component reagent flow cells, the initial overall flow rate was 1.0 mL min^{-1} . Individual flow rates of confluent reagents were adjusted to move the lateral position of the boundary.

3.2.2 Laser Ablation

Localized ablation of the polyimide membrane was achieved using a Q-switched frequency-doubled (532 nm) Nd:YAG laser (JDS Uniphase, NG-10320-110) that has an average power output of $\sim 25 \text{ mW}$, a pulse width of $\sim 600 \text{ ps}$, and a repetition rate of 7.65 kHz . The beam was expanded and collimated before being directed into the back aperture of a 40X objective (Olympus UPlanFl 0.75 NA). To achieve the most reproducible ablation, it was preferable to produce a Gaussian focus by slightly underfilling this objective (see **2.3.3 Real-Time Pore Ablation**). This approach reduced the maximum intensity at the focal point but extended the ablation voxel along the optical axis to more effectively ablate pores through the entire $7.6\text{-}\mu\text{m}$ -thick membrane. A half-wave plate/polarizing beam splitter pair situated immediately after the laser was used to adjust the average power of the beam before the objective back aperture to $8\text{-}10 \text{ mW}$.

A pulsed Uniblitz UHS1 shutter (Vincent Associates, VMM-T1) controlled exposure during ablation of a pore, delivering a train of 10-ms exposure periods (~ 76 laser pulses) repeated 2-5 times with 50-ms delays between adjacent exposures.

This exposure procedure was sufficient to efficiently ablate pores in the polyimide membrane while allowing time for heat to dissipate in solution between exposures. Additionally, the use of multiple exposure periods appeared to help dislodge bubbles that were formed during the first pulse that can become stuck to the lip of the pore. Use of these parameters resulted in a successful pore (i.e., one that produces a consistent reagent stream) in approximately 70% of attempts. The average diameter of pores, as determined by SEM, was $3.9 \pm 0.9 \mu\text{m}$ (n=50). Full width half maximum stream diameters shown in figures 2-7 ranged from $\sim 10\text{--}40 \mu\text{m}$, depending primarily on the solution flow rate in the dosing cell and the distance of the stream from a pore. Dosing stream widths are larger than the diameter of their pores due to turbulent mixing at the pore and lateral diffusion in both directions downstream from the pore.

3.2.3 Cell Culture

Mouse neuroblastoma-rat glioma (NG108-15) hybrid cells were originally purchased from the American Type Culture Collection (ATCC) and stored in their normal growth media supplemented with 5% (v/v) dimethyl sulfoxide (DMSO) at concentrations of approximately $500,000 \text{ cells mL}^{-1}$ in liquid nitrogen until they were needed for culture. When thawed, cells were cultured in Dulbecco's Modified Eagle's Medium (DMEM; Corning Cellgro) supplemented with 10% (v/v) fetal bovine serum (HyClone, AVJ82746), 1% (v/v) penicillin/streptomycin (MP Biomedicals), and 1x HAT (1.0×10^{-4} hypoxanthine, 2.0×10^{-7} aminopterin, 1.6×10^{-4} thymidine; 50X HAT solution was purchased from MediaTech). Flasks were maintained at 37°C in a 5% CO_2 atmosphere at 100% relative humidity with media replacement every two days and cells

were split to a new flask every 4-5 days (depending on confluence) for up to 40 total passages. For loading into the flow device, cells were passaged from a confluent flask by exposure to 1mL of 1X Trypsin EDTA (MediaTech) for 2 minutes (quenched with 5 mL of DMEM). Cells were removed from the flask and centrifuged for 3 minutes at a relative centrifugal force (RCF) of 150 g. The supernatant was then removed and replaced with sufficient L-15 medium to produce a suspension of $\sim 10^5$ cells mL^{-1} . At a volume of 9.3 μL within the cell-culture flow cell, this procedure delivered approximately 10^3 cells to the flow chamber (corresponding to ~ 13 cells per mm^2 when settled). The cell field (intersection of cell-culture and reagent flow cells) for these experiments was 3.75 mm^2 .

3.2.4 Chemicals

MitoTracker Green FM (M7514), MitoTracker Red CMXRos (M7512), and Syto 13 fluorescent nucleic acid stain (S7575) were purchased from Molecular Probes (Eugene, OR). Fluorescein (11924) and 4',6'-Diamidino-2-phenylindole dihydrochloride (DAPI; 20271) were purchased from Acros Organics (Belgium). Rhodamine B (A13572) was purchased from Alfa Aesar (Ward Hill, MA). Bovine serum albumin (BSA; BAH64) was purchased from Equitech-Bio (Kerrville, TX). HEPES-buffered saline (HBS buffer) was prepared from 140 mM NaCl (S271), 5 mM KCl (P330), 750 μM $\text{Na}_2\text{HPO}_4 \cdot 7\text{H}_2\text{O}$ (S373), 6 mM $\text{C}_6\text{H}_{12}\text{O}_6$ (dextrose; D14), and 25 mM 4-(2-hydroxyethyl)-1-piperazineethanesulfonic acid (HEPES; BP310) in 18.2 M Ω water and adjusted to pH 7.1. All HBS buffer reagents were purchased from Thermo Fisher Scientific (Hampton, NH).

3.2.5 Microscopy

Both fluorescence and brightfield images were acquired on a Zeiss Axiovert 135 inverted microscope using either a 10X objective (Zeiss Fluar 0.5 NA) or a 20X objective (Zeiss Plan-Neofluar 0.5 NA) and a Hamamatsu Orca II CCD camera (C4742-98) controlled by MetaMorph Imaging Software (Molecular Devices). Fast switching images were acquired on a Hamamatsu Orca-Flash2.8 digital CMOS camera (C11440-10C) controlled by HCImage Live software (Hamamatsu). Fluorescence images required the use of a Zeiss HBO 100 mercury arc lamp and a three-position fluorescence slider module equipped with both red and green filter sets. Images were processed using MetaMorph and ImageJ (National Institutes of Health, Bethesda, MD).

3.3 RESULTS AND DISCUSSION

3.3.1 Multi-Reagent Device Design

To implement this concept, a reagent flow cell comprised of multiple variable flow rate inlets and a single outlet is stacked with a cell-culture chamber flowing at 90° to the reagent chamber (Figure 3.2a). A 7.6- μm thick polyimide membrane served as a barrier between the two flow cells, providing a biocompatible surface for cell culture [25,26] and an efficient substrate for ablating low-micrometer-diameter pores using a tightly focused pulsed (Nd:YAG) laser beam. A pressure gradient between the two flow cells forced reagents through pores into the cell culture chamber, where they became entrained by laminar flow into narrow streams that were directed at downstream subcellular targets. Relatively rapid laminar flow in the reagent flow cell limited mixing across boundaries separating confluent reagents. As a consequence, distinct reagent

"reservoirs" were established that are individually sampled by focal ablation of pores to create dosing streams of distinct composition.

3.3.2 Reagent Switching

The boundary position between confluent, laminar streams in a rigid flow channel is dictated by the relative volumetric flow rates [27], a characteristic that can be exploited experimentally to alter, in real time, which species in the reagent flow cell of the microfluidic cell dosing device is positioned beneath specific pores in the polyimide membrane. For example, if the flow rate of one reagent is increased relative to that of a second reagent, the boundary will encroach on the latter reagent. Hence, as the boundary passes beneath a pore, the solution traveling through the pore into the cell culture chamber will also change in composition. This phenomenon is depicted schematically (Figure 3.2b) and experimentally using a confluent system of fluorescein and nonfluorescent HEPES-buffered saline (HBS) in the reagent flow cell (Figure 3.2c). Initially, fluorescein supplies the "top" pore (positioned to the left of the imaged area), with HBS overlapping the middle and lowest pores, yielding a single fluorescein dosing stream across the top of the image (Figure 3.2b and 3.2c, top panels). By increasing the supply rate of fluorescein to the reagent flow cell, the boundary between fluorescein and HBS shifts rightward, first passing a pore positioned near the bottom left in the image (Figure 3.2b and 3.2c, middle panels), and finally the right-most pore positioned near the vertical center of the image (Figure 3.2b and 3.2c, lower panels). In this manner, reagent streams can be reversibly introduced to the cell culture chamber at desired positions and times, with temporal ordering dictated by the horizontal arrangement of pores.

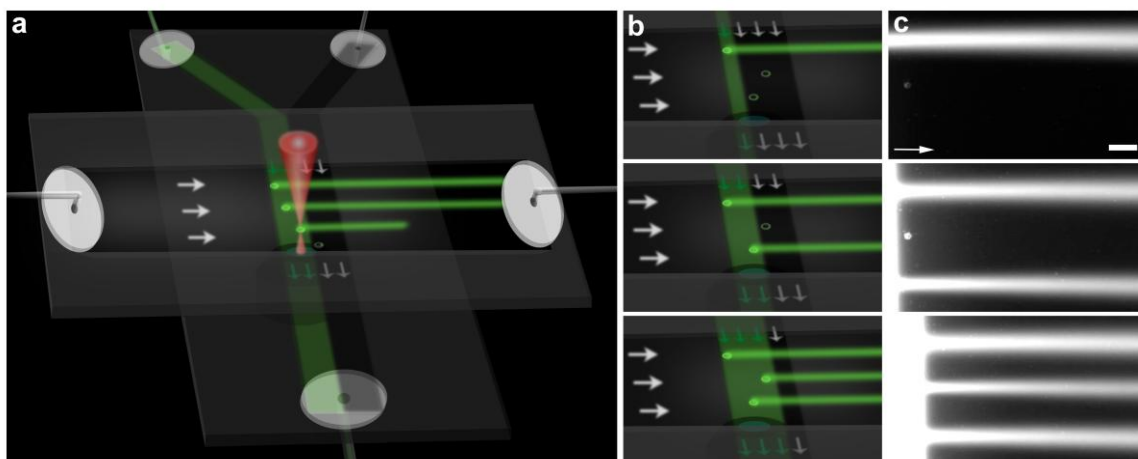


Figure 3.2: Reagent switching. (a) Device schematic. In this diagram, two dosing solutions (fluorescein, green; buffer, black) converge within the reagent channel under high-flow, low-mixing conditions, generating a stable pattern of dosing compounds with a defined boundary. By positioning the focus from a pulsed Nd:YAG laser beam (shown as red cone) on the membrane upstream from desired targets in the dosing channel, narrow dosing streams are produced that propagate from left to right in the diagram. The content of the dosing stream is controlled by the position of the boundary in the reagent channel, which is manipulated by altering the relative flow rates of the different reagents. (b) Composition of a dosing stream is independent of its placement. Here, flow in the reagent channel creates a fluorescein-buffer boundary that can be moved horizontally in the diagram to sequentially overlap pores shown at the top, bottom, then middle of the drawing. Because flow in the dosing channel is orthogonal to that in the reagent channel, fluorescein streams emerge horizontally in the diagram in the same sequence: top, bottom, then middle. (c) Experimental implementation of part (b). A series of staggered pores were ablated in a polyimide membrane separating a dosing chamber containing HBS buffer (left-to-right flow at 0.1 mL min^{-1}) from a reagent chamber containing $50 \text{ }\mu\text{M}$ fluorescein in HBS buffer (top-to-bottom flow at a total rate of 0.6 mL min^{-1}). As the flow rate of fluorescein in the reagent channel is increased, the boundary moves left to right in the image and fluorescein replaces HBS in the streams, emerging next from the lowest pore and finally from the middle pore. Scale bar = $50 \text{ }\mu\text{m}$.

This proof-of-concept experiment demonstrates the ability to supply distinct components to different pores using two visually distinct reagents, a nonfluorescent

buffer and a dye. However, the only fundamental limitation on stream composition is that reagents must be soluble in the solvent system(s) that are employed. It should be possible, for example, to investigate neuronal signal integration by targeting streams of excitatory and inhibitory ligands to defined sites on a neuronal process, and to dynamically substitute one type of input for the other.

These results illustrate a key design consideration in this microfluidic platform and a unique advancement from previous versions of the laser ablation microfluidic cell-dosing device. By establishing flow in the two channels along axes orthogonal to each other, position and composition of dosing streams can be controlled independently of one another. In this way, placement of a pore along the axis normal to solution flow in the dosing chamber determines the location of a resultant stream, while placement normal to solution flow in the reagent chamber (relative to the reagent boundary) dictates stream content. If flow in the two channels were set parallel to each other, it would not be possible to interdigitate streams of differing composition (Figure 3.2b, middle panel). This advancement allows for any combination of reagent streams to be patterned across the cell-culture field with user-defined spatial and temporal control.

3.3.3 Variable Concentration Control

While the laminar flow regime in the microfluidic cell dosing device prevents turbulent mixing of parallel reagent streams, small amounts of mixing do occur at the interface due to mass transport orthogonal to the flow direction (dependent on position downstream in the reagent flow cell and variable as a function of diffusivity (D) of the reagent species and flow rate (as it relates to \sqrt{t}) and turbulence at the convergence point

of inlets ($\sim 15\text{-}20\ \mu\text{m}$ depending on the flow cell). These effects at the boundary of two confluent laminar streams yield a narrow region of variable reagent concentration which can be expanded by slowing the flow rate within the reagent chamber (and increasing lateral diffusion by increasing t). By controlling the position of this more diffuse interfacial region such that it overlaps pores, it is possible to create dosing streams consisting of any ratio of two reagents supplied separately in the two confluent streams, or to tune the concentration of a single reagent at the boundary of confluent buffer (Figure 3.3a).

As a demonstration, $50\ \mu\text{M}$ fluorescein and nonfluorescent HBS buffer were flowed in parallel within a two-inlet reagent flow cell where the mixing region could be imaged as a steady decrease in fluorescence near the center of the flow cell over $\sim 100\ \mu\text{m}$. Pores were positioned along this gradient to produce multiple dosing streams of variable composition (created by a fractional dilution in fluorescein by HBS buffer) in the cell culture flow region (Figure 3.3b). By moving the reagent boundary via changes in relative flow rates of reagents, the fluorescein concentration in multiple parallel streams was ramped with different time dependencies (Figure 3.3c).

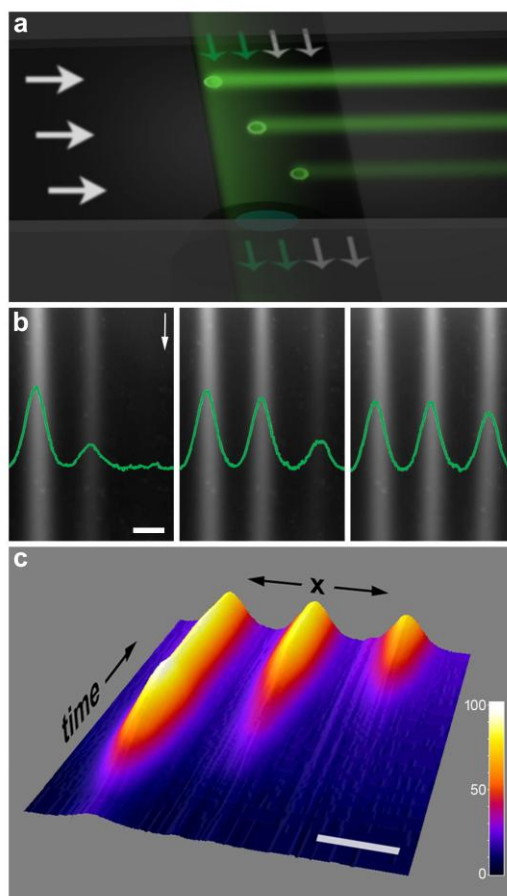


Figure 3.3: Variable concentration control. (a) Schematic depicting the overlay of dosing pores with a shallow gradient produced at the boundary of two slow-flowing reagent streams. (b) Placement of pores at different positions relative to a fluorescein-HBS buffer boundary produces dosing streams of differing composition. In the first image, undiluted fluorescein ($50 \mu\text{M}$), fluorescein-HBS gradient, and HBS alone, supply the left, middle, and right pores, respectively. As the boundary moves toward the imaged region (middle image), undiluted fluorescein overtakes the middle pore and the gradient now supplies dosing solution to the right pore. Overlays show plots of fluorescence (arbitrary units) as a function of distance across the image at points $\sim 100 \mu\text{m}$ from the bottom of the image. (c) Time evolution of fluorescence acquired along the horizontal dimension of part (b). The plot was created by extracting a fluorescence line profile at the same points across the image as part (b) from a movie acquired at 1 fps, where the color-encoded z-axis corresponds to fluorescence counts (AU). Total time for the plot is 40 s. Legend indicates color scale for minimum (0) to maximum (100) fluorescence across all time points. Scale bars = $50 \mu\text{m}$.

3.3.4 Arbitrary Mapping of Reagents

This high-resolution dosing strategy can be adapted to generate complex reagent patterns composed of multiple reagents in an interdigitated fashion. As a demonstration of this capability (Figure 3.4), a 5-inlet reagent flow cell fed by five confluent streams of HBS buffer, 250 μM DAPI, 25 μM rhodamine B, 25 μM fluorescein, and HBS buffer was used to produce dosing streams containing DAPI (blue; 1), rhodamine B (red; 2), and fluorescein (green; 3) in a dosing flow cell containing only HBS buffer. The upper left panel of Figure 3.4 shows a false-color composite image of the reagent flow cell, with rectangular regions of interest demonstrating where three dosing streams are subsequently produced within the dosing flow cell (white dotted lines) by pore ablation within the distinct reagent environments (upper right). By creating a set of pores at appropriate coordinates relative to the reagent reservoir (lower left), this configuration can be used to generate dosing maps of any arbitrary sequence (lower right). In this case, the orthogonal arrangement of the reagent and dosing flow cells means that composition of the dosing streams is determined only by the position of a pore in the lateral dimension of the reagent flow cell, and the location of the dosing stream is determined only by its lateral positioning in the dosing flow cell. This concept is demonstrated in Figure 3.4 (lower right) where an arbitrary, interspersed arrangement of DAPI, rhodamine, and fluorescein dosing streams was created by strategically aligned pores upstream from the dosing region.

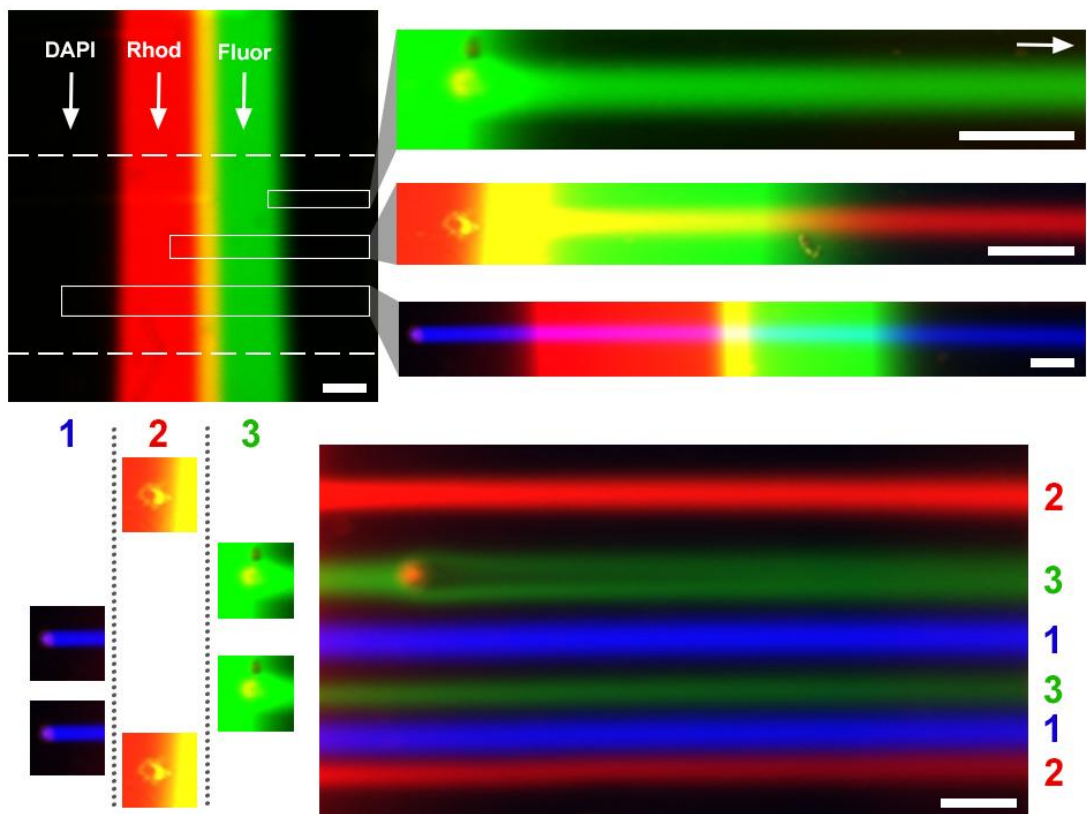


Figure 3.4: Generation of arbitrary multi-reagent dosing maps. Upper left: In a 5-inlet reagent flow cell, laminar flow streams of (left-to-right) HBS buffer, 250 μM DAPI, 25 μM rhodamine B, 25 μM fluorescein, and HBS buffer flow in parallel from top to bottom. This flow cell is separated from a dosing flow cell flowing left-to-right by a thin polyimide membrane. The strong absorbance of UV wavelengths by polyimide film effectively filters the excitation wavelengths of DAPI (340-380 nm), preventing it from being imaged in the top flow cell. The diffusional overlap of fluorescein and rhodamine streams appears as a narrow yellow region in a color-composite image. By patterning the pores in a user-designed arrangement, any conceivable pattern of interdigitated streams can be produced for downstream dosing. For example, the arrangement of pores shown in the lower left panel produces the pattern of streams shown in the lower right image. The uppermost green stream can be seen passing over and splitting around a surface feature on the membrane. Concentration variability in red streams results from pore occlusion/incomplete ablation. False color added in post-acquisition image processing for visualization. Scale bar (upper left) = 100 μm . All other scale bars = 50 μm .

3.3.5 Subcellular Targeting with Multiple Reagents

To evaluate applicability of this strategy for multi-component targeting of subcellular domains, a reagent flow cell was constructed using three confluent inlets (two reagents and a buffer line), a configuration that can be used to initiate and terminate dosing at desired times by overlapping the buffer region with a given pore. As a proof-of-concept for subcellular dosing, individual cells or clusters of cells were dosed at distinct sites with membrane-permeant reagents that display low intrinsic fluorescence outside the cytosol. Figure 3.5 demonstrates the result of simultaneously dosing differentiated mouse neuroblastoma-rat glioma hybrid (NG108-15) cells with multiple cellular trackers (MitoTracker Green FM, MitoTracker Red CMXRos, and Syto 13 nucleic acid stain). This procedure results in selective labeling of subcellular domains and opposing NG108-15 arborizations. At the relatively high concentrations used in this study (1.0-2.5 μM of each reagent), appearance of all dyes is observed in the cytosol as the dye accumulates over time.

The versatile dosing strategy described here provides a means to define extracellular chemical environments with high spatiotemporal resolution, opening opportunities for assessing how cells integrate instructions from a host of cues that modulate activity. Unlike previous methods [28-31], this approach enables the extracellular medium to be tailored at many sites in parallel with no necessary relationship between the cellular position and the content of the extracellular dosing solution.

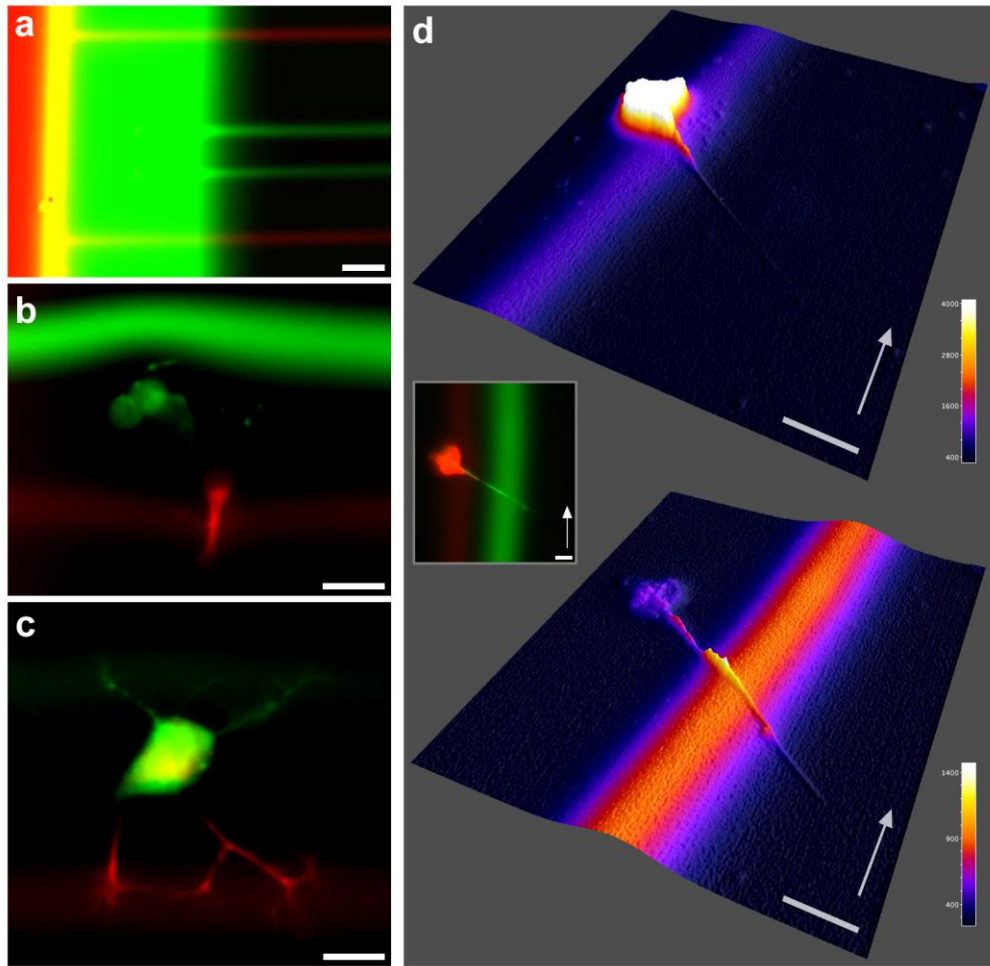


Figure 3.5: Multi-reagent targeting. Dosing streams of cellular labeling dyes can be created arbitrarily in a field of cells (a) that allow for site-specific targeting of individual cells (b) and subcellular dosing (c,d). (b) A cluster of cells (NG108-15) is dosed with $2.5 \mu\text{M}$ Syto 13 while a nearby cell is dosed with $1.0 \mu\text{M}$ MitoTracker Red CMXRos. Scale bar = $50 \mu\text{m}$. (c) A single NG108-15 cell is dosed on opposing neuritic arborizations using $1.0 \mu\text{M}$ MitoTracker Green FM and $1 \mu\text{M}$ MitoTracker Red CMXRos. Scale bar = $20 \mu\text{m}$. (d) Separate red (top) and green (bottom) fluorescence channels from inset image depicted as fluorescence-intensity surface plots. Green fluorescence (Syto) at the soma relative to its neuritic process is more than 40-fold below the levels seen in control experiments. Red fluorescence (MitoTracker) at the soma is saturated at the exposure time required for visualizing low-level staining in the neurite. Reagents contain $10 \mu\text{M}$ fluorescein and $10 \mu\text{M}$ rhodamine B, respectively, to aid visualization of the streams.

Although dosing in this unconstrained fashion is most readily performed when the reagent and cell culture chambers support orthogonal flow, the independence of dosing composition and position can be maintained so long as flow in the two channels is not fully parallel. This key development opens the possibility, for example, to dose alternating segments of a neurite with an agonist and antagonist, or to expose cells to arbitrarily defined step gradients of essentially any effector. As a consequence, it also should be feasible to combine the multi-reagent dosing described in the current work with stream-steering capabilities achieved by introducing multi-directional flow within the cell culture chamber [24].

Subcellular targeting can also be useful tool for investigating diffusion of molecular probes within cells (Figure 3.6). The dynamics of cell staining at different intracellular positions can be investigated by moving reagent boundaries such that the solution emerging from a given pore is switched from buffer to a MitoTracker dye. Over the course of ~30 seconds, a single cell will redistribute dye to portions of the cell outside the dosing stream. When the dosing stream is turned off, dye concentration equilibrates throughout the cell and eventually photobleaches under continuous illumination.

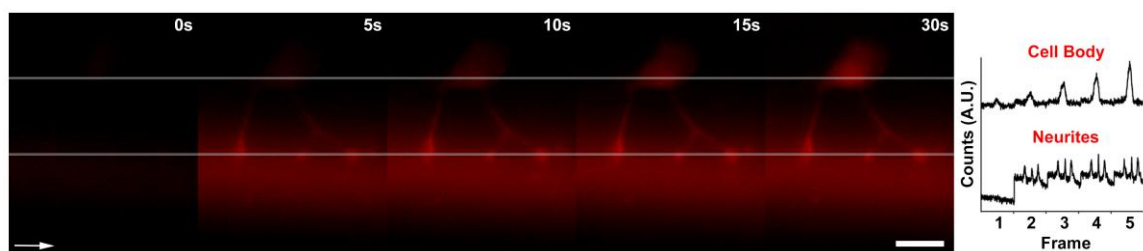


Figure 3.6: Dynamics of dye localization. A single NG108-15 cell is dosed with 1 μM MitoTracker Red CMXRos and images are acquired once every 5 s. The panel on the right plots fluorescence (arbitrary units) along the two horizontal lines drawn through the series of five frames. Note that fluorescence measured within the neurites increases more rapidly than that within the cell body, nearly reaching a maximum by the third frame (10 s post-initiation). The arrow represents flow direction. Media (L-15) flow rate = 0.1 mL min^{-1} . Total reagent flow rate = 0.4 mL min^{-1} . Scale bar = 25 μm .

3.3.6 Reagent Stream Overlap

In addition to distinct subcellular targeting, the multi-reagent microfluidic cell dosing platform opens the possibility for reagent mixing and the creation of complex dosing patterns with overlapping gradients of effectors. This makes it possible to study potential synergistic or antagonistic effects of dosing effectors in close proximity to dosing streams of the individual reagents in isolation, as well as adding the ability to create complex overlapping gradients similar to those cells encounter *in vivo*. For example, topographically mapped axonal connections in the visual system require highly specific and precise overlapping gradients of tectal guidance molecules (e.g., ephrin-A) in order to properly map from the retina to the midbrain conserving spatial integrity when transferring information from the retina to the visual centers [32]. In early embryo formation, the mesoderm develops into heart tissue over blood only in distinct regions of

overlap in the gradients of haematopoietic and cardiogenic signals (bone morphogenetic proteins) and inhibitors of a signaling pathway that promotes development of blood over cardiogenesis (the Wnt gene inhibitor, crescent) in the anterior of the embryo known as the heart-forming zone [33].

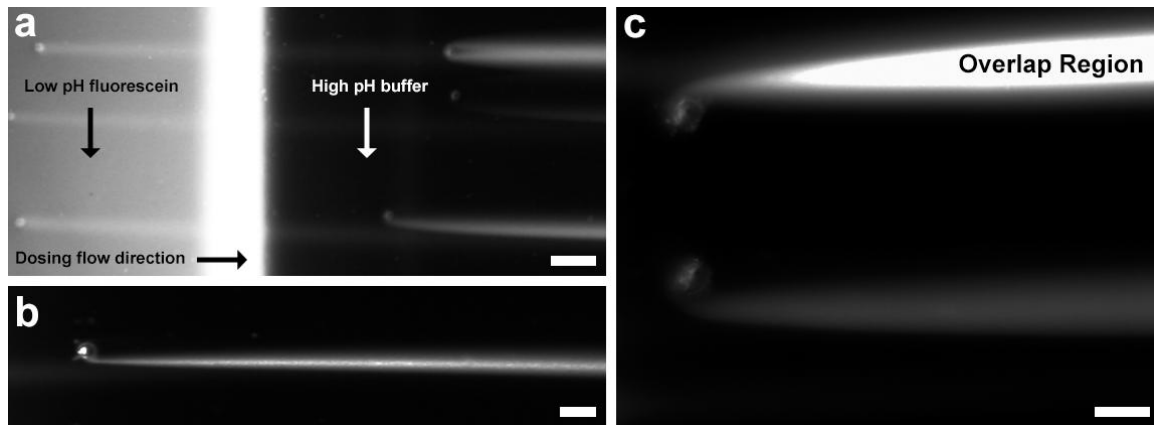


Figure 3.7: Overlapping streams. A two-inlet reagent flow cell is used to flow parallel streams of fluorescein in 0.02 M acetate buffer and 0.2 M Tris buffer taking advantage of the pH-dependent fluorescence properties of fluorescein. (a) Streams of low pH fluorescein that flow over or adjacent to streams of high pH, high ionic strength buffer exhibit a significant increase in fluorescence at the overlap region. Scale bar = 50 μm . (b) Overlapping edges of these laminar dosing streams persist for hundreds of micrometers downstream. Scale bar = 20 μm . (c) Mixing regions are defined by both streams and can appear on either side of the second pore. Initial flow rates are 0.1 mL min^{-1} in the cell-culture flow cell and 0.4 mL min^{-1} total in the reagent flow cell. Rates are adjusted during the experiment to properly place the boundary and to ensure a positive pressure differential from reagent to cell culture flow. Scale bar = 20 μm .

To demonstrate the capability of creating overlapping gradients, the varying pH-dependent fluorescence properties of fluorescein dye were used to visually illustrate stream overlap. The protonated form of fluorescein has a much lower fluorescence

quantum yield ($\Phi = 0.2-0.3$) than the deprotonated form ($\Phi = 0.9-1.0$) with an emission maximum at 521 nm and a pK_a of 6.4 [34]. As a result, when a stream of acetate-buffered (pH = 4.0) fluorescein solution (low fluorescence) is flowed adjacent to a stream of nonfluorescent Tris buffer (pH = 9.0), a small overlap region of high fluorescence appears (Figure 3.6a) in the two-inlet reagent flow cell. While mixing due to turbulent flow is negligible in this laminar flow regime, there is still lateral diffusion across the flow in addition to a small amount of mixing created at the junction when both inlet ports meet to create the bulk flow within the reagent flow cell that creates this narrow overlap region. As a demonstration of the technique, pores created on opposing sides of this boundary at the same lateral position in the dosing flow cell overlap, exhibiting a spike in stream fluorescence in the mixing region (Figure 3.7). If these pores are slightly offset (5-10 μm) in either direction (Figure 3.7c) then an even narrower mixing region is created that is smaller than the individual streams that extends hundreds of micrometers downstream (Figure 3.7b).

This proof-of-concept demonstration shows how a multi-reagent dosing system can be used to create more complex dosing patterns from overlapping gradients that may be useful for studying emergent synergistic and antagonistic effects of dosants and for studying cell behavior amongst competing gradients. While the reaction used in this demonstration is a simple protonation/deprotonation, more complex reactions (e.g., redox chemistry, FRET interactions) could be pursued in future studies whether as a chemical reactor or for creating chemical effectors from precursor solutions *in situ* just prior to cell exposure.

3.3.7 Reagent Switching with High Temporal Resolution

A number of cell processes are dictated not only by the chemical composition of the microenvironment around the cell, but also by the temporal distribution (e.g., periodicity, duration, and delay) of chemical signals in the environment. As surrounding cells communicate via chemical pathways, the environment around a single cell can change drastically over short time frames. A number of prominent signaling molecules and proteins (e.g., calcium, p53, Msn2, and NF- κ B) carry encoded information for cell signaling in their temporal patterns, as well as their absolute concentrations [35]. For example, rat basophilic leukemia cells exhibit varying levels of gene expression when exposed to the same concentration of released intracellular calcium with varying periodicity. In this case, it was found that photolytically released spikes in intracellular Ca^{2+} at 1-minute intervals produced significantly higher levels of β -lactamase gene expression than 30-second and 2-minute intervals [36]. For PC-12 cells, receptor desensitization by a 20-ms pulse of adenosine-5'-triphosphate (ATP) expresses markedly different characteristics than a 2-ms pulse at the same concentration [37]. With these processes in mind, a variation of the flow device presented here was adapted to produce fast switching streams (as short as 50 ms), offering the ability to investigate temporally periodic processes in future studies with the same flexibility and spatiotemporal resolution presented in previous sections with this approach.

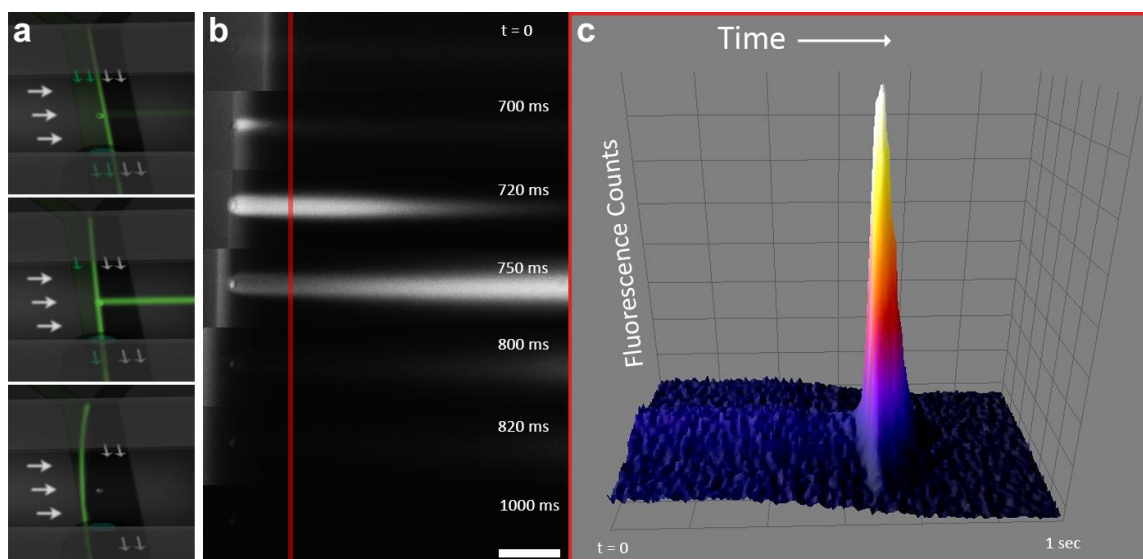


Figure 3.8: Fast switching of reagents. (a) A two-inlet reagent flow cell was used to flow parallel streams of $100\ \mu\text{M}$ fluorescein in $0.02\ \text{M}$ acetate buffer ($\text{pH} = 4$) and $0.2\ \text{M}$ Tris buffer ($\text{pH} = 9$) taking advantage of the pH-dependent fluorescence properties of fluorescein. The boundary between reagent flow was placed adjacent to a pore by adjusting the relative flow rates of the two reagents. When the fluorescein (left) source pump is turned off, the boundary quickly shifts from right to left in the reagent flow cell, sweeping across the pore (b) Experimental demonstration of part (a), resulting in a transient dosing stream with a FWHM of $48\ \text{ms}$. (c) A 3D surface plot showing a fluorescence line profile across the dosing stream $\sim 50\ \mu\text{m}$ downstream (red line) from the pore. The spike in intensity occurs when the dosing stream is briefly switched to fluorescent solution as the boundary sweeps across the pore. Media flow rate = $0.25\ \text{mL min}^{-1}$. Fluorescein flow rate = $0.80\ \text{mL min}^{-1}$. Tris buffer flow rate = $0.50\ \text{mL min}^{-1}$. Image acquisition rate = $250\ \text{frames s}^{-1}$. Scale bar = $50\ \mu\text{m}$.

Similar to the stream overlap studies, a two-inlet reagent flow cell is used to flow a solution of fluorescein parallel in $0.02\ \text{M}$ acetate buffer ($\text{pH} = 4$) to a solution of $0.2\ \text{M}$ Tris buffer ($\text{pH} = 9$) with HBS buffer on the opposite side of a membrane with flow cells oriented perpendicular to each other (Figure 3.8). The reagent flow regime creates a narrow ($\sim 10\ \mu\text{m}$ diameter) mixing region, where fluorescence increases as a result of

co-localization of fluorescein and relatively high $[\text{OH}^-]$. This narrow mixing region translates laterally when the relative flow rates of each reagent are changed. Since the dosing flow cell is arranged perpendicular to the reagent flow cell, a shift in this boundary allows for the high fluorescence region to sweep across pores that have been ablated in the polyimide membrane separating the two flow cells. In this case, the fastest switching events occur when one of the source pumps is shut off completely and the second reagent is allowed to fill the entire chamber. In this regime, the fastest switching events that have been observed lasted 48 ms (FWHM) at an image acquisition rate of 250 frames s^{-1} . The limiting factor in further reducing switching times is the expansion of the interface region as it sweeps across the pore. This technique allows for fast switching of mixed reagent solutions that would be useful for studying agonist/antagonist interactions with high temporal resolution.

To investigate single-reagent switching, a variety of multi-inlet flow cells were developed to create a central stream that is hydrodynamically focused by the sheath flow created by the outermost flow inlets. In a three-inlet flow cell, a 1-mm central stream of fluorescein (0.1 mL min^{-1}) can be focused down to $\sim 50 \text{ }\mu\text{m}$ by exterior focusing streams of HBS buffer ($\sim 1.5 \text{ mL min}^{-1}$). By changing the relative flow rates of the buffer streams, this centrally located fluorescein stream is shifted from left to right across a series of pores, where the composition of the streams emitted by these pores observably shifts from buffer to dye. The fastest switching times in these studies were acquired using a five-inlet reagent flow cell where a central fluorescein dosing stream (0.03 mL min^{-1}) was focused down to a $50 \text{ }\mu\text{m}$ width with HBS buffer (0.6 mL min^{-1}) continuously flowing in

the first, second, and fourth inlets. The fifth inlet was attached to a static syringe containing HBS buffer that could be manually pumped to instantaneously increase pressures in the reagent flow cell and deflect the central dosing stream. The fastest switching times observed in this regime lasted ~80 ms (FWHM). Ultimately, the lower end of switch times was limited by the high flow rates and pressures used in these experiments, where the reagent flow cell often failed leading to solution leaks. Future studies will focus on using narrower channels to maximize the effect of the focusing ratio while maintaining a higher-volume central channel for fast sweeping of the stream as well as demonstrating cell dosing for studying temporal dosing effects on cellular processes (e.g., Ca²⁺ signaling).

3.4 CONCLUSIONS

The strategy described here, based on stacked laminar flow reagent and cell culture chambers, provides a means to define extracellular chemical environments with high spatial resolution (~10 μm) and temporal control (50 ms – hours). Unlike previous methods, this approach provides the possibility to define the extracellular medium at many sites in parallel with no necessary relationship between the cellular position and the content of the extracellular dosing solution. This key development opens the possibility, for example, to dose alternating segments of a neurite with an agonist and antagonist, or to expose cells to arbitrarily defined step gradients of essentially any effector. Additional functionality may be achieved by pairing the technique with previously reported stream-steering capabilities [24] and valving by controlled pore occlusion [23].

Moreover, the laser ablation properties of bulk PDMS [37] and methods for fabricating ultra-thin sheets from the material [38] suggest that an integrated device, including the polymer membrane, could be fabricated entirely from a single material.

Future work will focus on transitioning the entire dosing device to a single modular unit that would be more accessible to commercialization. Additionally, there is room for improvement in minimizing switching times by further narrowing the dosing stream via hydrodynamic focusing. The technique also could be adapted to study cellular response in the time domain (e.g., frequency-based Ca^{2+} signaling) by controlled oscillatory dosing through a modulated pumping cycle.

3.5 REFERENCES

1. Li Jeon, N.; Baskaran, H.; Dertinger, S. K. W.; Whitesides, G. M.; Van De Water, L.; Toner, M. Neutrophil chemotaxis in linear and complex gradients of interleukin-8 formed in a microfabricated device. *Nature Biotechnology* **2002**.
2. Raper, J.; Mason, C. Cellular Strategies of Axonal Pathfinding. *Cold Spring Harbor Perspectives in Biology* **2010**, 2, a001933–a001933.
3. Bargmann, C. I.; Horvitz, H. R. Chemosensory neurons with overlapping functions direct chemotaxis to multiple chemicals in *C. elegans*. *Neuron* **1991**, 7, 729–742.
4. Marin, O. Directional guidance of interneuron migration to the cerebral cortex relies on subcortical Slit1/2-independent repulsion and cortical attraction. *Development* **2003**, 130, 1889–1901.
5. Maldve, R. E.; Zhang, T. A.; Ferrani-Kile, K.; Schreiber, S. S.; Lippmann, M. J.; Snyder, G. L.; Fienberg, A. A.; Leslie, S. W.; Gonzales, R. A.; Morrisett, R. A. DARPP-32 and regulation of the ethanol sensitivity of NMDA receptors in the nucleus accumbens. *Nature Neuroscience* **2002**, 5, 641–648.
6. Foxman, E. F.; Kunkel, E. J.; Butcher, E. C. Integrating conflicting chemotactic signals. The role of memory in leukocyte navigation. *J. Cell Biol.* **1999**, 147, 577–588.
7. Lin, F.; Nguyen, C. M.-C.; Wang, S.-J.; Saadi, W.; Gross, S. P.; Jeon, N. L. Neutrophil migration in opposing chemoattractant gradients using microfluidic chemotaxis devices. *Ann Biomed Eng* **2005**, 33, 475–482.
8. Forbes, E. M.; Thompson, A. W.; Yuan, J.; Goodhill, G. J. Calcium and cAMP levels interact to determine attraction versus repulsion in axon guidance. *Neuron* **2012**, 74, 490–503.
9. Marin, O.; Valiente, M.; Ge, X.; Tsai, L.-H. Guiding Neuronal Cell Migrations. *Cold Spring Harbor Perspectives in Biology* **2010**, 2, a001834–a001834.
10. Keenan, T. M.; Folch, A. Biomolecular gradients in cell culture systems. *Lab on a Chip* **2008**, 8, 34.
11. Prager, D. J.; Bowman, R. L.; Vurek, G. G. Constant volume, self-filling nanoliter pipette: Construction and calibration. *Science* **1965**, 147, 606–608.
12. Stosiek, C. In vivo two-photon calcium imaging of neuronal networks. *Proceedings of the National Academy of Sciences* **2003**, 100, 7319–7324.
13. Ming, G.; Song, H.; Berninger, B.; Holt, C. E.; Tessier-Lavigne, M.; Poo, M. cAMP-dependent growth cone guidance by netrin-1. *Neuron* **1997**, 19, 1225–1235.

14. Boyden, S. The chemotactic effect of mixtures of antibody and antigen on polymorphonuclear leucocytes. *Journal of Experimental Medicine* **1962**, *115*, 453–466.
15. Zigmond, S. H. Ability of polymorphonuclear leukocytes to orient in gradients of chemotactic factors. *Journal of Cell Biology* **1977**, *75*, 606–616.
16. Takayama, S.; Ostuni, E.; LeDuc, P.; Naruse, K.; Ingber, D. E.; Whitesides, G. M. Laminar flows: Subcellular positioning of small molecules. *Nature* **2001**, *411*, 1016.
17. Takayama, S.; Ostuni, E.; LeDuc, P.; Naruse, K.; Ingber, D. E.; Whitesides, G. M. Selective chemical treatment of cellular microdomains using multiple laminar streams. *Chemistry & Biology* **2003**, *10*, 123–130.
18. Olofsson, J.; Bridle, H.; Jesorka, A.; Isaksson, I.; Weber, S.; Orwar, O. Direct access and control of the intracellular solution environment in single cells. *Analytical Chemistry* **2009**, *81*, 1810–1818.
19. Atencia, J.; Cooksey, G. A.; Locascio, L. E. A robust diffusion-based gradient generator for dynamic cell assays. *Lab on a Chip* **2012**, *12*, 309–316.
20. Tourovskaia, A.; Figueroa-Masot, X.; Folch, A. Differentiation-on-a-chip: A microfluidic platform for long-term cell culture studies. *Lab on a Chip* **2005**, *5*, 14.
21. Sims, C. E.; Allbritton, N. L. Analysis of single mammalian cells on-chip. *Lab on a Chip* **2007**, *7*, 423.F
22. Santillo, M. F.; Arcibal, I. G.; Ewing, A. G. Flow characterization of a microfluidic device to selectively and reliably apply reagents to a cellular network. *Lab on a Chip* **2007**, *7*, 1212.
23. Nielson, R.; Shear, J. B. Parallel Chemical Dosing of Subcellular Targets. *Analytical Chemistry* **2006**, *78*, 5987–5993.
24. Moorjani, S.; Nielson, R.; Chang, X. A.; Shear, J. B. Dynamic remodeling of subcellular chemical gradients using a multi-directional flow device. *Lab on a Chip* **2010**, *10*, 2139.
25. Kawakami, H.; Hiraka, K.; Nagaoka, S.; Suzuki, Y.; Iwaki, M. Neuronal attachment and outgrowth on a micropatterned fluorinated polyimide surface. *Journal of Artificial Organs* **2004**, *7*.
26. Richardson, R. R.; Miller, J. A.; Reichert, W. M. Polyimides as biomaterials: preliminary biocompatibility testing. *Biomaterials* **1993**, *14*, 627–635.
27. Truskey, G. A. *Transport Phenomena in Biological Systems*; Pearson/Prentice Hall: Upper Saddle River, N.J, 2004.

28. Cooksey, G. A.; Sip, C. G.; Folch, A. A multi-purpose microfluidic perfusion system with combinatorial choice of inputs, mixtures, gradient patterns, and flow rates. *Lab on a Chip* **2009**, *9*, 417.
29. VanDersarl, J. J.; Xu, A. M.; Melosh, N. A. Rapid spatial and temporal controlled signal delivery over large cell culture areas. *Lab on a Chip* **2011**, *11*, 3057.
30. Taylor, A. M.; Blurton-Jones, M.; Rhee, S. W.; Cribbs, D. H.; Cotman, C. W.; Jeon, N. L. A microfluidic culture platform for CNS axonal injury, regeneration and transport. *Nature Methods* **2005**, *2*, 599–605.
31. Dertinger, S. K. W.; Chiu, D. T.; Jeon, N. L.; Whitesides, G. M. Generation of gradients having complex shapes using microfluidic networks. *Analytical Chemistry* **2001**, *73*, 1240–1246.
32. Flanagan, J. G. Neural map specification by gradients. *Current Opinion in Neurobiology* **2006**, *16*, 59–66.
33. Olson, E. N. Development. The path to the heart and the road not taken. *Science* **2001**, *291*, 2327–2328.
34. Martin, M. M.; Lindqvist, L. The pH dependence of fluorescein fluorescence. *Journal of Luminescence* **1975**, *10*, 381–390.
35. Purvis, J. E.; Lahav, G. Encoding and decoding cellular information through signaling dynamics. *Cell* **2013**, *152*, 945–956.
36. Li, W.; Llopis, J.; Whitney, M.; Zlokarnik, G.; Tsien, R. Y. Cell-permeant caged InsP3 ester shows that Ca²⁺ spike frequency can optimize gene expression. *Nature* **1998**, *392*, 936–941.
37. Khiroug, L.; Giniatullin, R.; Talantova, M.; Nistri, A. Role of intracellular calcium in fast and slow desensitization of P2-receptors in PC12 cells. *British Journal of Pharmacology* **1997**, *120*, 1552–1560.
38. Kim, T. N.; Campbell, K.; Groisman, A.; Kleinfeld, D.; Schaffer, C. B. Femtosecond laser-drilled capillary integrated into a microfluidic device. *Applied Physics Letters* **2005**, *86*, 201106.
39. Thangawng, A. L.; Ruoff, R. S.; Swartz, M. A.; Glucksberg, M. R. An ultra-thin PDMS membrane as a bio/micro–nano interface: fabrication and characterization. *Biomedical Microdevices* **2007**, *9*, 587–595.
40. Hoppe, T. J.; Moorjani, S. G.; Shear, J. B. Generating arbitrary chemical patterns for multi-point dosing of single cells. *Analytical Chemistry* **2013**, *85*, 3746–3751.

Chapter 4: Biocompatibility of Photofabricated Protein Microstructures for Studying Cancer-Cell Migration and Invasion

4.1 INTRODUCTION

One of the defining characteristics of cancer cells is their ability to proliferate rapidly and indefinitely beyond the Hayflick limit inside the body, eventually resulting in malignancy that overwhelms the immune system [1]. When the body is able to contain these cells, it can more reasonably manage the disease and targeted treatment (both internally [2] and externally [3]) can be attempted. In many cases, however, as collections of these cells grow more abundant in confined spaces they undergo the epithelial-mesenchymal transition (EMT) [4] and become increasingly adept at finding weaknesses in the basal membrane. By exploiting these weaknesses, cells can migrate into the bloodstream and lymph system, taking advantage of the body's natural transportation mechanisms to metastasize [5]. Many cancer-cell lines develop invadopodia [6], actin-based cellular structures similar to podosomes used by normal cells to cross tissue barriers (e.g., diapedesis by macrophages [7]) and to remodel tissue (e.g., bone resorption by osteoclasts [8]). These invasive structures exhibit high levels of proteolysis and allow cells to rearrange the extracellular matrix (ECM), creating pathways for invasion [9]. While these openings are often much smaller than the cells themselves, cancer cells exhibit a remarkable ability to induce conformational changes (e.g., in spindle morphology [10]) that allow them to invade, even those with abnormally large nuclei (up to 1:1 nucleus:cytoplasm in anaplastic cells [11]).

Several existing methods have been adopted for studying cancer-cell invasion and metastasis (e.g., Boyden chambers [12] and microfabricated channel arrays [13]). Transwell migration assays (the modern version of Boyden chambers) are a simple way to test cell migration and invasion through layers of ECM or similar material (e.g., collagen, laminin) in response to a chemotactic gradient. For example, transwell assays have been used to show that mesenchymal (bone marrow-derived) stem cells are recruited by certain breast-cancer cell lines, which then stimulate a ~60-fold increase in paracrine chemokine signals (specifically CCL5) from nearby stem cells that increase cancer-cell invasion in the transwell assays by as much as 150% [14]. While these assays provide valuable information on behavioral changes in populations of cells, they offer no information on a single-cell level or on the mechanisms of invasion, as cells cannot be directly observed during the assay. This limitation is relatively insensitive to the importance of rare variants in triggering metastasis, where primary tumors with a “good prognosis” (gene expression suggesting little to no metastasis) can metastasize due to proliferation of highly metastatic phenotypes within a heterogeneous cancer-cell population [15].

For single-cell studies of invasion, soft-lithography techniques have been adopted for creating complex geometries of micrometer-scale channels to investigate the tendencies and mechanisms of invasion for highly metastatic cell lines. Microchannels made from poly(dimethylsiloxane) (PDMS) have led to the discovery that cancer-cell invasion can be driven not only by chemical gradients, but also spatial gradients in their physical microenvironment [16]. Additionally, some cancer cells exhibit self-signaling

patterns in confined environments that allow them to remotely sense and consequently avoid physically constricted environments by integrating these self-generated gradients. As a result, epithelial cancer cells can efficiently navigate complex mazes in the absence of other cells or external chemoattractants [17]. Unfortunately, these studies were performed within materials that differ significantly in both physical and chemical properties from the tissue that cancer cells encounter in the body. For example, the elastic modulus of PDMS microstructures (~1 MPa [18]) is at least an order of magnitude larger than most biological tissue (with the exception of bone) and maintains little of the viscoelastic properties of tissue that cancer cells exploit to invade small channels and none of the permeability to proteins and cofactors. While these techniques elicit interesting information about cancer cells and their invasive behavior, it remains uncertain how these results translate to *in vivo* conditions.

As discussed in Chapter 1, previous work in the Shear Lab has led to the development of a novel technique for rapidly prototyping protein-based 3D microstructures by multiphoton fabrication [19]. These materials possess properties more in line with biological material [20], can be chemically functionalized [21], have tunable mechanical properties in the range of biological tissues [22], and are rapidly (i.e. on minute time scales) fabricated with sub-micron resolution. Applications of the technique for studying somatic-cell behavior in previous studies have focused exclusively on protein microstructures as physical and chemical cell guidance cues, but multiphoton fabrication allows for more complex 3D microstructures (e.g., confined microchambers with roofs) to be constructed for studying single-cell behavior in physically constrained

environments. The work presented here focuses on the fabrication of highly permeable 3D microstructures, from biological molecules (crosslinked protein), for use in invasion and migration assays. Additionally, the biocompatibility of these microstructures is established for a variety of cancer-cell lines. This work exhibits the feasibility of using photofabricated protein microstructures as a means for observing cancer-cell migration and invasion on a single-cell level in defined 3D physical environments.

4.2 EXPERIMENTAL METHODS

4.2.1 Fabrication Solutions

Bovine serum albumin (BSA) fabrication solutions were prepared by combining BSA (400 mg mL⁻¹ unless otherwise noted) and rose bengal (5 mM unless otherwise noted) in phosphate-buffered saline (PBS). Gelatin fabrication solutions were prepared by combining type A gelatin (200 mg mL⁻¹), BSA (25 mg mL⁻¹), and rose bengal (5 mM) in PBS and warming to 60°C for ~5 minutes before transferring to a thermomixer set to 1,000 RPM and 37°C for ~1 hour. All fabrication solutions were centrifuge-filtered in 0.22 µm PVDF centrifugal filter units (Millipore, Billerica, MA) at an RCF of 16,100 g for 5-15 minutes (depending on viscosity) immediately before transferring to a 4-well chambered #1 coverglass (Nunc Lab-Tek[®], 155383).

4.2.2 Multiphoton Fabrication

The process used for the photofabrication of 3D protein microstructures is an adaptation of instrumentation presented by Ritschdorff, et al. in 2012 [23]. Here, the collimated beam of a mode-locked titanium:sapphire laser (Coherent Mira 900), tuned to

740 nm, was aligned to a two-axis galvanometer-driven scan mirror (Leica TCS-4D, Bensheim, Germany) that raster-scanned the beam at 0.1 Hz on the slow axis and 110.0 Hz on the fast axis across an 800×600 digital micromirror device (DMD) from a DLP projector (BenQ, MP510). Each mirror ($\sim 16 \mu\text{m} \times \sim 16 \mu\text{m}$) within the DMD chip was individually adjusted to the “on” (white) or “off” (black) position by its corresponding pixel in a binary mask displayed by the controlling PC. Mirrors in the black position redirected the beam to a beam block while mirrors in the white position directed the beam to overfill the back aperture of a 1.30 numerical aperture (NA) 40X Zeiss Plan-NeoFluar oil-immersion microscope objective. By positioning the DMD in a plane conjugate to the specimen plane of the objective, a 1:1 mapping was achieved between the DMD display and the fabrication pattern in solution at a magnification equal to the inverse of the objective magnification (40X). 3D objects were fabricated within the solution by synchronizing optical axis steps of the microscope stage with changes in the mask displayed to the DMD using software written in LabView™ (National Instruments, Austin, TX), where each individual mask corresponded to a single layer of fabrication in solution.

Fabrication was performed on a Zeiss Axiovert 135 inverted microscope equipped with a three-axis translational stage (562, Newport Corp., Irvine, CA) driven by motorized actuators (LTA-HS, Newport Corp., Irvine, CA) that were controlled using a motion driver (ESP300, Newport Corp., Irvine, CA). Binary masks were created using Adobe Photoshop and ImageJ (National Institutes of Health, Bethesda, MD). After fabrication, protein microstructures were rinsed with 60°C PBS until no apparent

photosensitizer (red color) remained in the rinsing solution (~20-30 rinses). Structures were then coated with 1.0 mg mL⁻¹ rat-tail type I collagen (BD Biosciences) in a 30% ethanol/70% water (v/v) mixture overnight at room temperature in a sterile cell-culture hood. Prior to cell plating, structures were rinsed three times with plating media.

4.2.3 Cell Culture

Mouse neuroblastoma-rat glioma (NG108-15) hybrid cells were originally purchased from the American Type Culture Collection (ATCC) and stored in their normal growth media supplemented with 5% (v/v) dimethyl sulfoxide (DMSO) at concentrations of approximately 500,000 cells mL⁻¹ in liquid nitrogen until they were needed for culture. When thawed, NG108-15 cells were cultured in Dulbecco's Modified Eagle's Medium (DMEM; Corning Cellgro) supplemented with 10% (v/v) fetal bovine serum (HyClone, AVJ82746), 1% (v/v) penicillin/streptomycin (MP Biomedicals), and 1X HAT (1.0 × 10⁻⁴ M hypoxanthine, 2.0 × 10⁻⁷ M aminopterin, 1.6 × 10⁻⁴ M thymidine; 50X HAT solution was purchased from MediaTech). MDA-MB-231 cells were cultured in Roswell Park Memorial Institute (RPMI 1640; HyClone) medium supplemented with 10% (v/v) fetal bovine serum. Flasks were maintained at 37°C in a 5% CO₂ atmosphere at 100% relative humidity with media replacement every two days. Cells were passaged to a new flask every 4-5 days (depending on confluence) for up to 40 total passages.

For plating on protein microstructures, cells were passaged from a confluent flask by exposure to 1 mL of 1X Trypsin EDTA (MediaTech) for 2-5 min (longer times were required for MDA-MB-231) and quenched with 5 mL of media. Cells were removed from the flask and centrifuged for 3 minutes at a relative centrifugal force (RCF) of

150 g. The supernatant was then removed and replaced with sufficient medium (1% FBS L-15 unless otherwise noted) to produce a suspension of 10^4 - 10^5 cells mL^{-1} (depending on desired density on the surface). 500 μL of cell solution was then transferred into microstructure-containing wells resulting in $\sim 5,000$ - $50,000$ cells on the surface of a single well. The dish was placed on a microscope stage situated in a home-built incubation chamber (see **2.2.6 Environmental Chamber**) set to maintain cell temperatures at ~ 35 °C and $\sim 45\%$ relative humidity.

4.2.4 Microscopy

Brightfield images were acquired on a Zeiss Axiovert 135 inverted microscope equipped with an incubation chamber using either a 10X objective (Zeiss Fluor 0.5 NA), 20X objective (Zeiss Plan-Neofluar 0.5 NA), or 40X objective (Olympus UPlanFl 0.75 NA) with a Hamamatsu Orca II CCD camera (C4742-98) controlled by MetaMorph Imaging Software (Molecular Devices). Images were acquired once every 1-5 minutes with exposure times of 10-200 ms. The illumination was shuttered between acquisitions using a pulsed Uniblitz UHS1 shutter (Vincent Associates, VMM-T1).

4.2.5 Chemicals

Bovine serum albumin (BAH64) was purchased from Equitech-Bio (Kerrville, TX). Rose bengal (330000) and type A gelatin from porcine skin (G2500) were purchased from Sigma-Aldrich (St. Louis, MO). All reagents were used as received without purification.

4.3 RESULTS AND DISCUSSION

4.3.1 Biocompatibility of Photofabricated Protein Microstructures for Somatic Cells

To investigate the feasibility of using photocrosslinked protein microstructures as a tool for studying cell migration and invasion, a series of microchambers with roofs were fabricated from either BSA or gelatin, and cells were plated in wells containing the structures. Figure 4.1 shows three arrays of different invasion and migration geometries fabricated from gelatin (4.1a) or BSA (4.1b and 4.1c) with 5 mM rose bengal as the photosensitizer. Both MDA-MB-231 breast cancer cells and NG108-15 cells survived around, within, and on top of these photofabricated structures. Somatic-cell viability has previously been demonstrated in the presence of BSA lines (1-2 μm tall) fabricated on a surface [24], but the 3D structures used in these studies were 20-30 μm tall and often surrounded cells in multiple dimensions. Additionally, bacterial viability has been established within these larger photofabricated microstructures [25], but somatic cells are more sensitive to the cytotoxicity of type II photosensitizers and cannot be conditioned to survive in the presence of these species. While the use of a type II photosensitizer (i.e., rose bengal) allowed for robust fabrication of these complex 3D structures, singlet oxygen production from excitation of the sensitizer at the high concentrations used during fabrication (~ 5 mM) was toxic to cells. For this reason, the *in situ* fabrication technique used to fabricate structures around gelatin-suspended bacteria [25] was not compatible with somatic cells. To reduce post-fabrication cytotoxicity in these studies, microstructures were thoroughly rinsed before plating cells and light exposure occurred only during image acquisition (~ 10 -200 ms exposures every 1-5 minutes).

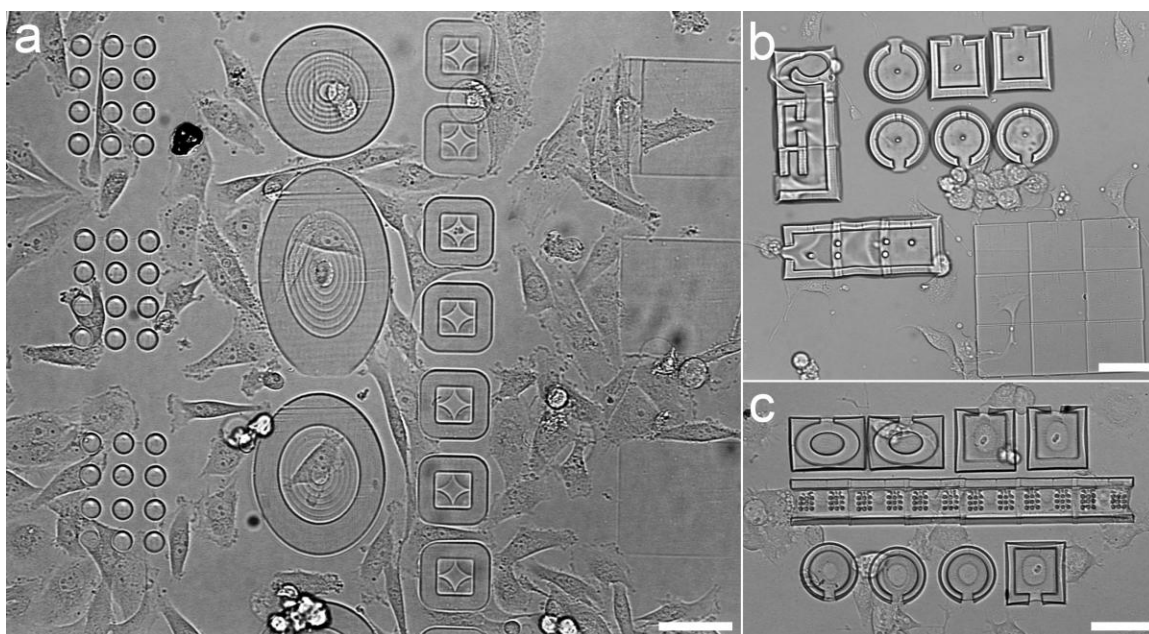


Figure 4.1: Protein microstructures for studying cell behavior. A variety of user-defined 3D geometries were photofabricated from concentrated solutions of BSA or gelatin. (a) MDA-MB-231 breast cancer cells were plated around a series of posts, wells, and pads fabricated from gelatin and rose bengal. (b,c) NG108-15 cells were plated around a series of cell traps and chambers fabricated from BSA and rose bengal. All microstructures shown above were 10-30 μm tall. Scale bars = 50 μm .

Cells (NG108-15 and MDA-MB-231) plated around large (up to 500- μm diameter) arrays of photofabricated microstructures made from gelatin and BSA showed no observable differences in behavior (e.g., motility, morphology, mortality) as they contacted and migrated within the structures as compared to cells in control dishes and cells on the borosilicate glass surface away from the structures. In particular, cells continued to exhibit normal division (i.e., rate and morphology) on and around protein structures, a strong indicator that cells were proceeding through the steps of the cell cycle and that cell health was unaffected by the structures. Figure 4.2a shows a single

NG108-15 cell that landed on a BSA microstructure and proceeded to divide while atop the structure. Figure 4.2b shows an NG108-15 cell that divided over the course of 20 minutes while in direct contact with the edge of a BSA microstructure. In the first frame of each time sequence, the chromosomes can be seen aligning immediately prior to division. Multiple cells in each experiment divided over the course of 48-hour experiments, even in serum-free media where the expected doubling time was 6-7 days for this cell type [26].

In these studies, the only apparent toxicity of structures occurred during fluorescence imaging when residual photosensitizer was presumably excited by the high irradiance of the mercury-arc lamp, creating toxic levels of singlet oxygen. In these cases, all cells within the field of illumination almost immediately exhibited necrosis, while cells outside the illumination field remained viable. As a precaution, brightfield illumination was shuttered at all times except when an image was being acquired. Separate experiments using SKBR3 human breast cancer cells, HepG2 human liver cancer cells, SKOV3ip.1 human ovarian cancer cells, and IC-21 mouse macrophage cells displayed similar behavior in and around photofabricated microstructures with no apparent toxicity (data not shown), suggesting that these results are transferable across a wide variety of cell types.

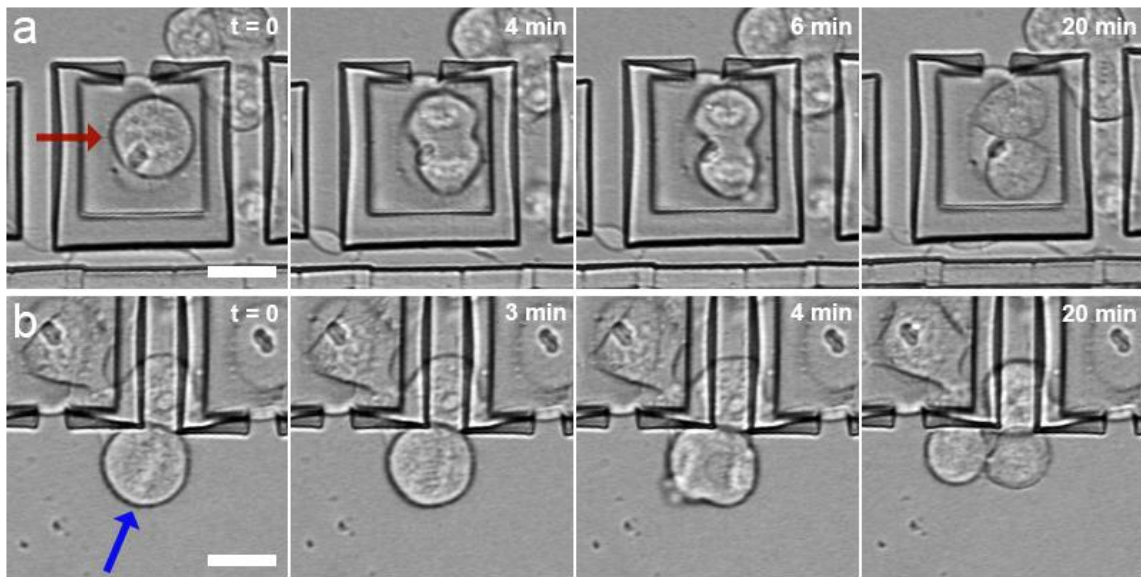


Figure 4.2: Cell division. In contact with protein microstructures, cells continued to display behavior typical of the cell type, including division. (a) Image sequence of a single NG108-15 cell (red arrow) sitting atop a 30 μm tall protein microstructure that displayed normal division. Total time = 20 min. (b) Image sequence of a single NG108-15 cell (blue arrow) in contact with a protein microstructure that displayed normal division. Total time = 20 min. Scale bars = 20 μm .

4.3.2 Cellular Interaction with Fabrication Materials

To investigate how cells would interact with 3D structures, a variety of flat, rectangular pads (3 μm tall) were constructed from gelatin or BSA. (Figure 4.3) Cells that landed on BSA pads, as well as cells that migrated onto BSA pads, displayed typical morphology and behavior, including motility, but moved quickly off the BSA structures to the glass. Figure 4.3a shows a neuritic process that extended across a series of BSA pads. After 90 minutes, the neurite had retracted off the BSA surface and a different cell migrated across the BSA pads with a distinct leading edge indicative of lamellipodia formation directing the cell's motility. By frame 3, all cells had migrated off the BSA

pads and were migrating only along the edges of the structure. The preference for glass over BSA is particularly apparent at high cell densities, where cells typically surrounded short (3- μm -tall) pads of BSA on each side without migrating onto the pad.

In contrast, cells on gelatin pads often remained on the pads for long periods of time (hours), but displayed a significantly different morphology than on the glass or BSA pads including limited lamellipodia and neurite formation (NG108-15). Figure 4.3b shows a single NG108-15 cell that migrated from the BSA edge of a photofabricated pad to the gelatin center of the pad. The cell displayed a less distinct lamellar leading edge and exhibited very little differentiation on the gelatin surface. This was typical behavior of the cells observed in these studies. Differences in cell morphology between hard (glass, tissue culture plastic) and soft (tissues, gels) surfaces are common, particularly in the formation of cytoskeletal elements (large, flat, leading lamellae on glass; small, pointed extensions in tissue) and cell roundedness (more flattened on glass) [27]. For this initial demonstration of the technique in invasion studies, it was determined that glass was the preferable surface for studying cells interacting with protein microstructures. Future work will focus on invasion in true 3D structures by coating the surface surrounding these structures with a layer of fabricated material or by directly plating the cells on protein microstructures.

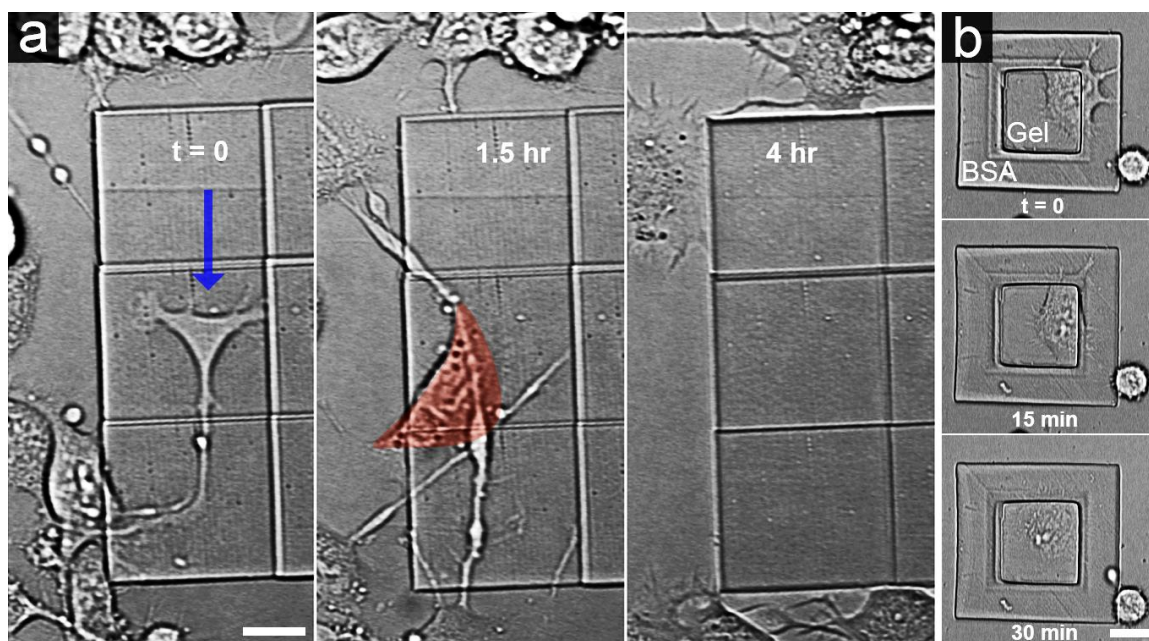


Figure 4.3: Cells on photofabricated protein pads. (a) Multiple NG108-15 cells displayed typical morphology on BSA pads (5 μm tall) including neurites (left; blue arrow) and lamellipodia (middle; different cell highlighted in red), but these cells migrated quickly (in minutes) off the pad and displayed long-term preference for the glass (right). Scale bar = 20 μm . (b) A single NG108-15 cell migrated from atop the outer ring (3- μm -tall BSA) of a photofabricated pad to the inner circle (3- μm -tall gelatin). These cells showed a greater affinity for gelatin (Gel) over BSA, but also exhibited reduced motility on gelatin surfaces. Total time = 30 min. Scale bar = 20 μm .

In contrast to crosslinked protein surfaces, cells interacted much differently with the edges of photofabricated material on the surface of the glass. NG108-15 cells would often attach to loosely crosslinked gelatin and disrupt the integrity of the material as they migrated away from the structures. Figure 4.4 shows a single NG108-15 cell that deformed the top of a gelatin wall and then pulled at the material. MDA-MB-231 breast cancer cells have been observed lifting gelatin structures from the glass surface that were not securely adhered. For both cell types, cellular interaction with the material was much higher for gelatin structures than BSA structures. In the future, these interactions with

crosslinked gelatin microstructures, along with their tunable mechanical properties [22], may be used to further investigate how cancer cells manipulate the materials in their vicinity for invasion. For example, one of the limiting factors in obtaining biologically relevant information from microchannel studies of cancer-cell invasion is the low compliance of the materials used to fabricate the channels [16]. These materials are not deformable under cellular-level forces and are impermeable to cell-signaling factors, resulting in a limiting case where cells are forced to reorient their cytoskeletal morphology and channels act only as rectified physical guidance cues, or “cellular ratchets” [28]. In invasion assays presented in these studies, the initial aperture sizes and geometries as they were fabricated are discussed, but cells in some instances were able to deform and manipulate the material (much as they do *in vivo*) to migrate through narrow openings.

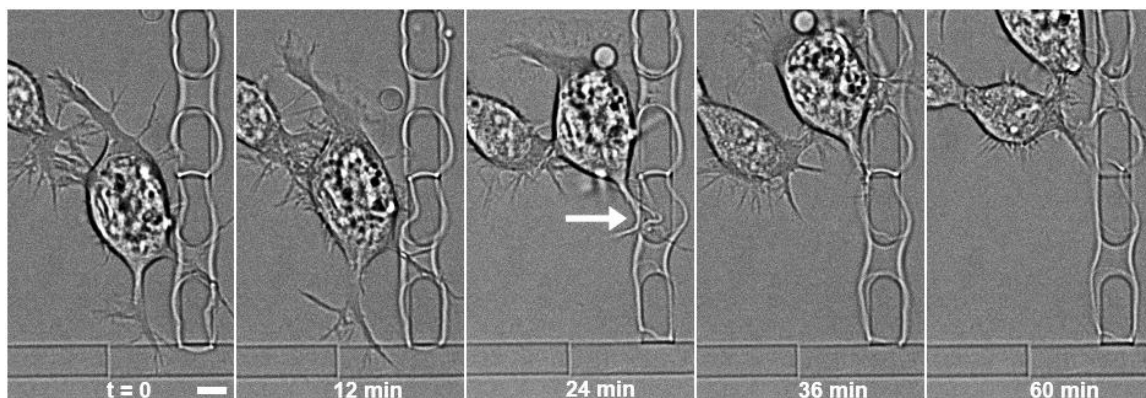


Figure 4.4: Gelatin interaction. A single NG108-15 cell interacted with and deformed a photofabricated gelatin wall. The top of the wall buckled significantly against these cellular forces (white arrow). Total time = 60 minutes. Scale bar = 10 μm .

4.3.3 Invasion of Protein Microstructures

Previously, photofabricated protein microstructures have been used exclusively as guidance cues for somatic cells, primarily in 2D geometries at the surface of the cell substrate [21,23]. For these studies, a variety of 3D trap geometries were created with both BSA and gelatin to investigate how cells would interrogate and invade open protein microstructures. Importantly, these microchambers were enclosed architectures that could not be fabricated using molding or soft lithography techniques. Figures 4.5 and 4.6 show NG108-15 cells that migrated into enclosed protein microchambers through narrow openings at the surface. Generally, a cell only invaded microstructure chambers when confined in high local densities of cells. However, once a cell invaded a chamber, there was little apparent effort to leave the space even when cells outside the chamber had migrated away from the opening. Figure 4.5a shows a single NG108-15 cell that migrated into a BSA microchamber due to high cell density and crowding at the opening. That cell proceeded to compress its entire cell body into the structure. For openings smaller than an individual cell could invade, cells often extended cytoskeletal structures to interrogate the interior of the chambers.

In serum-starved conditions intended to induce differentiation, NG108-15 cells demonstrated the ability to extend neurite-like processes hundreds of micrometers along walls inside protein structures that they were unable to invade. Figure 4.5b shows a single neuritic process extending from an NG108-15 cell that stretched along a covered BSA microstructure for nearly 300 μm . In contrast to previous applications, these studies demonstrated the ability of photofabricated protein microstructures to act as enclosed 3D microchambers for observing cell invasion and containment.

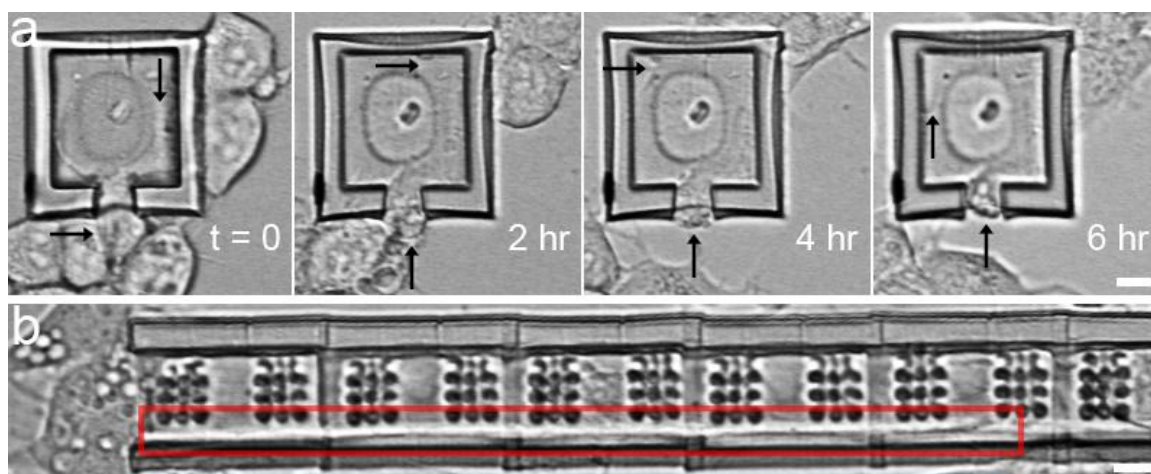


Figure 4.5: NG108-15 invasion in protein microstructures. Crowded cells near the openings of protein microstructures interrogated and invaded the spaces inside structures. (a) A single NG108-15 cell extended lamellipodia into a BSA microchamber before fully migrating into the chamber (black arrows). The cell remained in the chamber even after other cells had migrated away. Total time = 6 hours. (b) A neurite from a single NG108-15 cell (red box) extended within an enclosed BSA microstructure along the wall for more than 250 μm . Scale bars = 20 μm .

Most importantly for these initial studies, cells that migrated into and around these chambers showed no apparent deleterious effects from the photocrosslinked protein structures, even when surrounded (or in direct contact) on all sides with protein structure. At lower densities, cells that fully migrated into and back out of a protein microchamber exhibited typical migration behavior and morphology. Figure 4.6 shows a cell division where one progeny entered a chamber and the other daughter cell migrated around the outside of these chambers. The cell that entered the chamber remained inside for ~ 3 hours before migrating out of the structure. Both cells exhibited similar motility and morphology on the open glass surface. Similar experiments have been extended up to one week with daily media renewal.

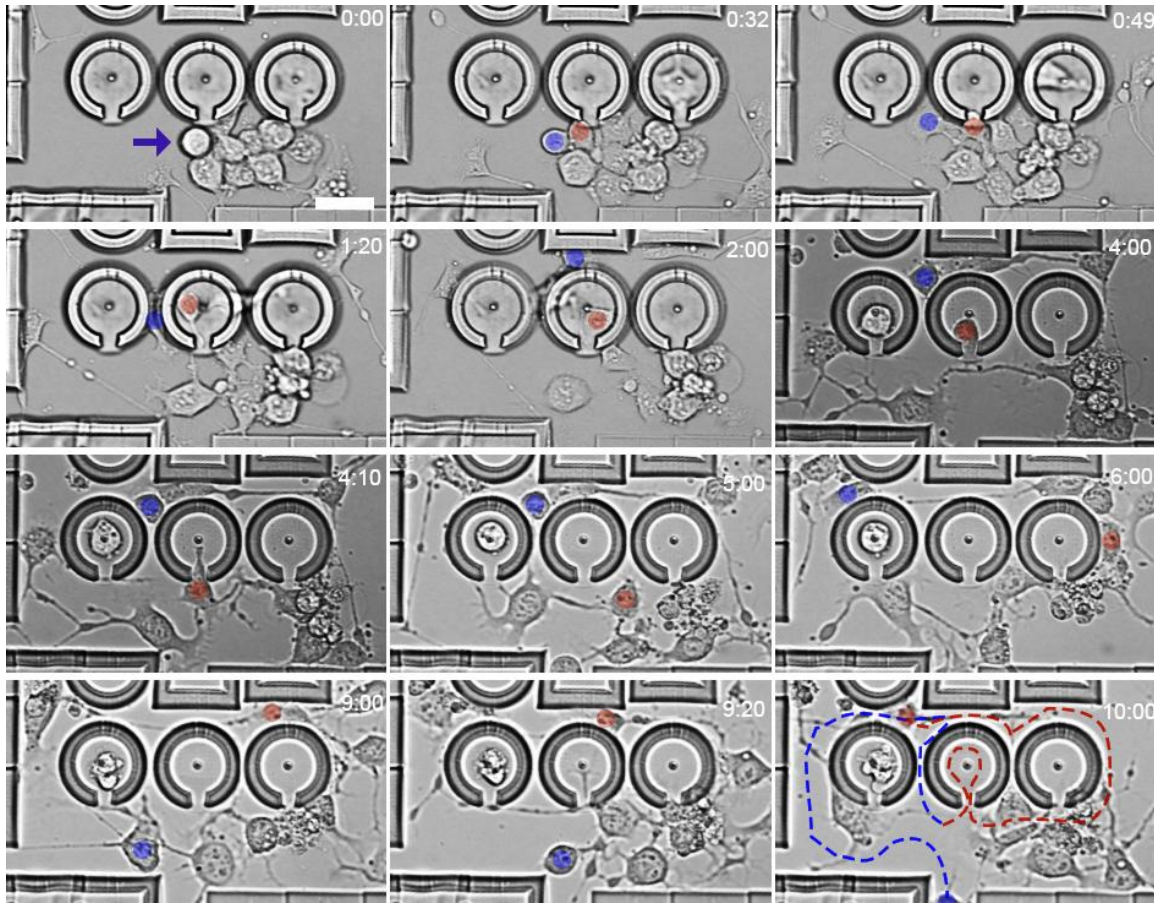


Figure 4.6: Invasion and migration. NG108-15 cells were plated around a series of BSA microchambers to investigate their invasive behavior. A single NG108-15 cell (purple arrow) divided and the progeny migrated separately away from the division site. One cell (highlighted in red) entered the adjacent BSA microstructure (through a 10- μm -wide opening), migrated around the central support post, and left the structure after ~ 4 hours. The other daughter cell (highlighted in blue) squeezed through a ~ 5 - μm -wide opening between structures and migrated out of the field of view. The final frame shows a trace of the migration pattern of each cell, respectively, over the 10-hour imaging sequence. Scale bar = 40 μm .

4.3.4 Migration through Narrow Openings

After demonstrating somatic-cell viability and invasive behavior for the first time in photofabricated protein microstructures, a more standardized assay was sought to provide a simple demonstration of the narrowest openings that could be navigated by cells. These invasion “grids” were constructed from either BSA or gelatin. Initial experiments involved plating cells within an array of 7- μm -tall walls with openings of various sizes positioned at regular intervals along the grid. Cells that migrated through these openings were adhered to the surface, but appeared to partially lift above the openings when moving the large cell body and nucleus through the openings. Figure 4.7 shows a single NG108-15 cell that migrated through a 4- μm -wide opening in a BSA wall. The leading edge of the cell migrated through the opening at the surface where cytoskeletal elements could quickly rearrange to fit through the narrow space, but the cell body lifted above the opening and migrated partially through the opening and partially over the wall. In many cases, NG108-15 cells were large enough to migrate over these walls (5-10 μm tall) at locations with no opening. The narrowest channels invaded by NG108-15 cells in these experiments were 4 μm wide.

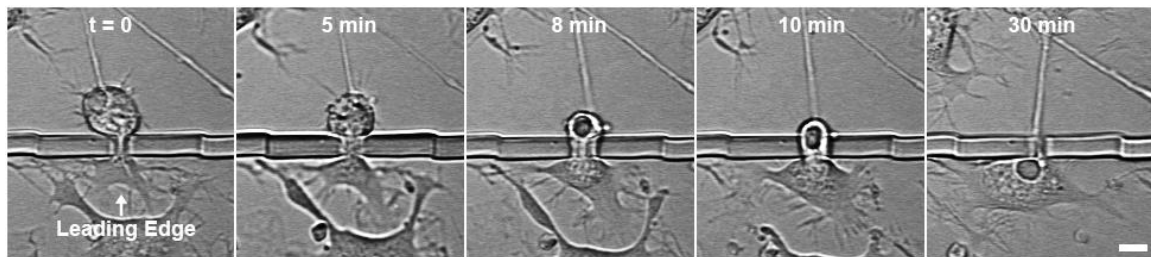


Figure 4.7: Open narrow channel migration. A single NG108-15 cell squeezed through a 4- μm -wide opening in a 7- μm -tall BSA wall. Portions of the cell body appeared to lift off above the wall during migration through the aperture. Total time = 30 minutes. Scale bar = 10 μm .

To position cells where they would be forced to migrate through narrow openings, an array of closely spaced 20- μm tall gelatin spikes was created. In these instances, cells plated directly within the array filled the spaces between spikes and migrated through these narrow openings. Because the distance between spikes increased from the surface of the glass to the top of the spike, cells were afforded the opportunity to migrate through a range of aperture sizes. NG108-15 cells were unable to create wide lamellar leading edges to direct motility, but the cells did exhibit flattened cytoskeletal structures that interrogated the surface and spaces between spikes before the entire cell migrated. Figure 4.8 shows a single NG108-15 cell that migrated through an array of spikes over the course of ~ 4 hours. The guiding actin cytoskeletal elements of the cell appeared to be adhered to the surface of the glass while the cell body remained above the surface in larger openings between the spikes. These studies emphasize the ability of single cells to navigate narrow openings with the cell body constrained above the surface of the substrate. This is a unique intermediate between 2D invasion (determined by tractile and adhesion forces at the surface with highly organized actin-based cytoskeletal structures [29]) and 3D invasion (determined by cell/matrix interactions across the entire surface of the cell [30]), where cells adapt an entirely different morphology in order to migrate through gels.

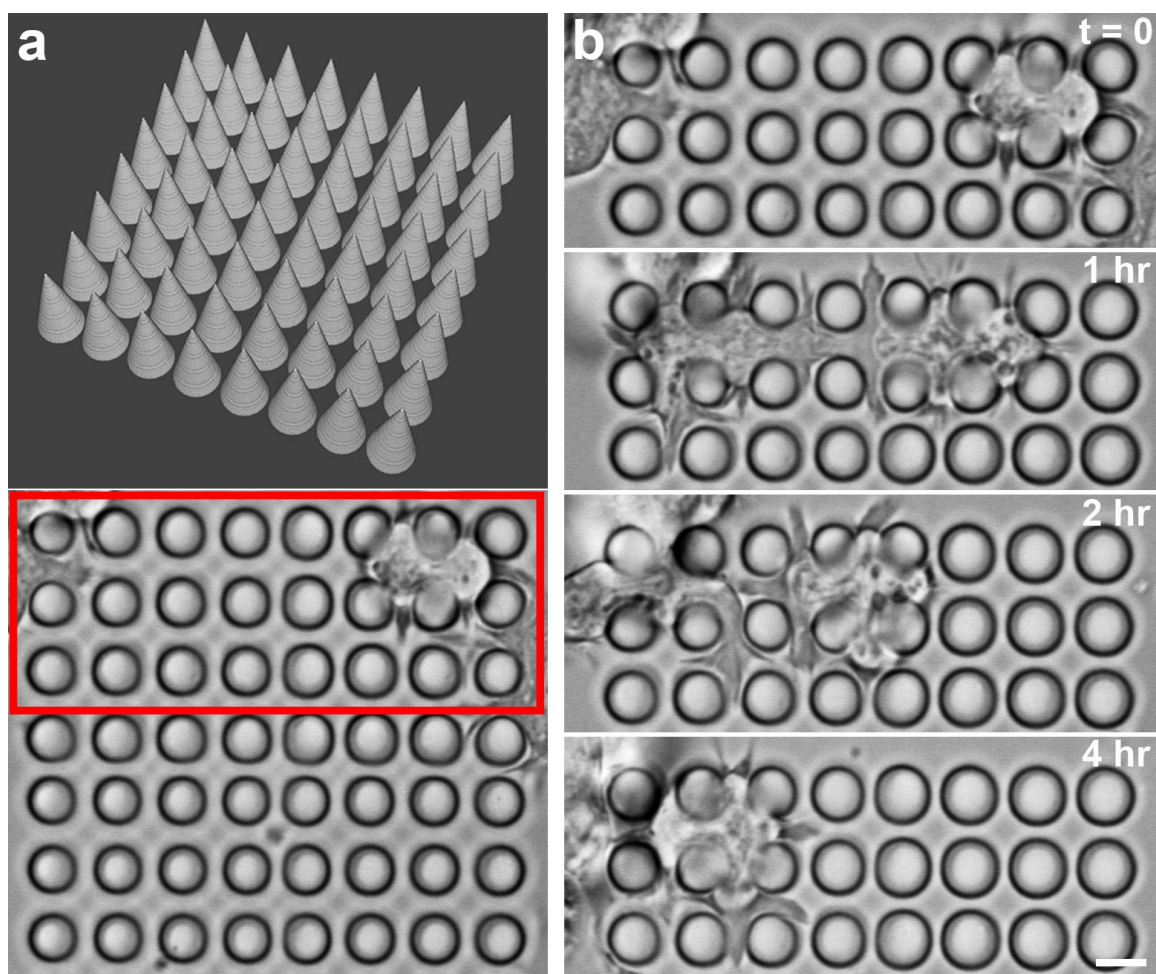


Figure 4.8: Gelatin spikes. (a) A 3D graphic projection (top) of the digital masks used to make 20- μm -tall spikes (10- μm -diameter at the base) and the entire array of gelatin spikes (bottom) (b) A timelapse image sequence from a section within the spikes (red box). Two NG108-15 cells navigated the 5- μm -wide spaces between rows of 20- μm tall spikes by cytoskeletal protrusions at the surface with the cell body suspended above the surface within the spikes. Total time = 4 hours. Scale bar = 10 μm .

To constrain cell migration to a known 2D aperture size without disrupting the cell body's ability to fully contact the surface of the glass, an array of gelatin posts was created with roofs over the apertures and intermediate openings to contain non-migrating cells. In these instances, NG108-15 cells within the arrays continuously rotated and

re-oriented within the openings before extending a leading edge into an adjacent opening, which could then pull the cell body through. Figure 4.9 shows a single NG108-15 cell that periodically migrated between photofabricated gelatin posts. While the cytoskeletal leading edge interrogated adjacent spaces, the cell body remained within the less-confined circular regions while re-orienting intracellular material to fit through the narrow (6- μm -wide) apertures. The gelatin posts were reversibly deformed as the entire cell body squeezed between posts, demonstrating the unique structural response of the material to cellular-level mechanical forces. These assays offer a simplified 2D demonstration of the process cells undergo when migrating through short, narrow openings *in vivo*.

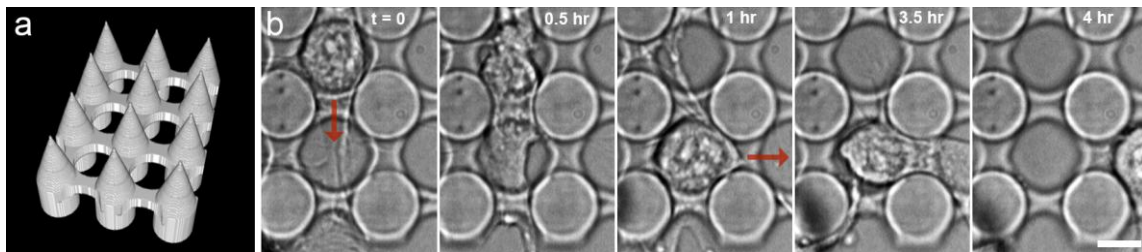


Figure 4.9: Closed narrow channel migration. (a) A 3D graphic projection of the digital masks used to create an array of gelatin posts (10 μm tall; 6 μm edge-to-edge spacing). Spikes at the top of each post prevented cells from landing on the roof of the structure. (b) A single NG108-15 cell continuously rotated within a circular opening while extending into an adjacent space, then migrated through the opening (red arrows). The cell repeated these steps and migrated again. Total time = 4 hours. Scale bar = 10 μm .

The human breast cancer cell line MDA-MB-231 was also investigated in a series of invasion assays. MDA-MB-231 cells are known to be highly metastatic and can invade spaces much smaller than the cell [31]. Figure 4.10 shows multiple MDA-MB-231 cells that migrated through spaces created by a series of gelatin posts. These cells exhibited the

ability to easily navigate a series of posts with 6- μm -wide migration apertures. The cells displayed a number of characteristics distinct from NG108-15 cells, namely that the cell can adopt a long spindle-type morphology that allows it to stretch to a much narrower shape and pull the cell body through constrained spaces without the intermediate openings required for NG108-15 migration. Figure 4.10c shows a single MDA-MB-231 cell that exhibited this spindle-like morphology before pulling the cell body through a series of openings. The cells also showed high levels of interaction with the gelatin, including bifurcating around gelatin posts before migrating in one direction around the post. Figure 4.10b shows a single MDA-MB-231 cell that directly approached a photofabricated gelatin post, bifurcated in both directions around the post, and eventually migrated in one of the two directions. These simplified mazes represent a demonstration of an effective 3D microstructure assay for observing single-cell invasion behavior without the rectifying characteristics of inelastic PDMS microchannels. Specifically, the viscoelastic properties of the crosslinked gelatin allowed these cells to reversibly compress posts as they migrated without damaging the infrastructure. Additionally, the open geometry of the mazes ensured free diffusion of cell signaling factors and cell waste. Future work will focus on quantifying cell behavior in these environments or within more complex geometries.

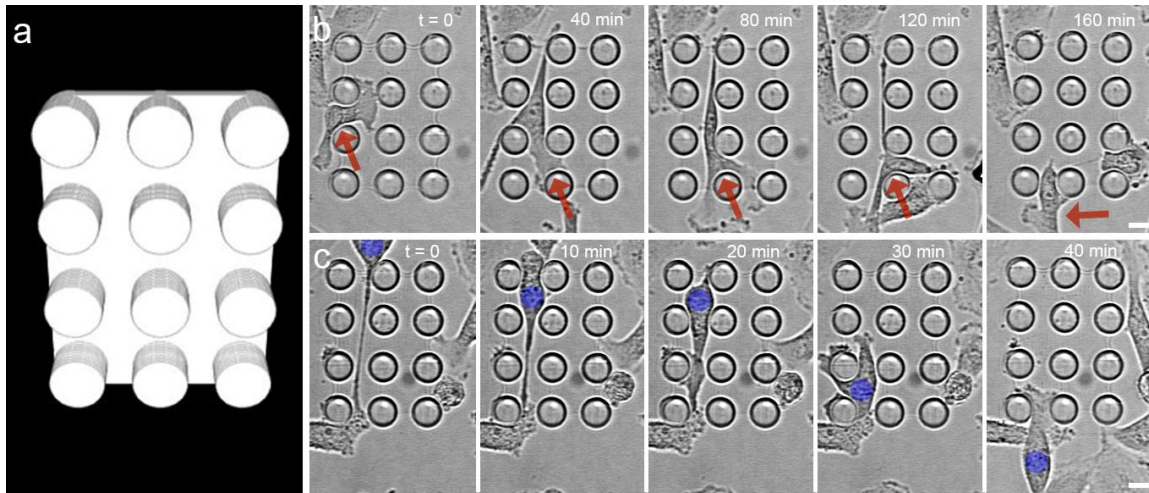


Figure 4.10: MDA-MB-231 invasion. (a) A 3D graphic projection of the digital masks used to create contained posts (10 μm tall; 6 μm edge-to-edge spacing). (b) A single MDA-MB-231 breast cancer cell navigated a series of posts. The cell bifurcated (red arrow) as it encountered each post and extended both directions before migrating around the post. (c) A single MDA-MB-231 (blue marker) lengthened in a spindle-type morphology before contracting to pull the cell body through a series of posts. Scale bars = 10 μm .

4.3.5 Vertical Invasion Traps

While cells demonstrated the ability to invade chambers from the surface of the glass, there was additional biological relevance to be gained by demonstrating cell invasion through the surface (e.g., invadopodia leading the way through the basement membrane). With this in mind, photofabricated chambers with invasion ports in the roof were created from gelatin. These chambers provided the additional benefit that cells that invaded from the top would be less likely to migrate out of the chambers, effectively making them single-cell traps for collecting a specific phenotype or producing true clonal populations in a small, constrained volume. Figure 4.11 shows a single MDA-MB-231 cell that landed on the roof of a funneled gelatin microchamber with an entry port in the roof. After migrating around the roof of the structure, the cell migrated through the opening and remained viable within the interior of the microchamber through the end of

the experiment (~24 hours). This represented the first demonstration of 3D invasion within a protein microstructure by a cell with no contact with the glass surface (until after invasion). These results combined the advantage of direct single-cell observation of fabricated channel assays with the 3D invasion properties of transwell assays. Unfortunately, the success rate of these chambers was low because they relied both on cells landing on the roof of the chamber during plating and on cells invading the chamber from the roof. Cells that did invade these chambers exhibited normal morphology for the cell type on a glass surface and showed no apparent deleterious effects from containment in the limited volume. Cells were plated in a serum-starved media (0% FBS L-15) and exhibited no division when constrained in chambers. For the purposes of single-cell trapping, the *in situ* fabrication technique presented in Chapter 5 was a more efficient technique.

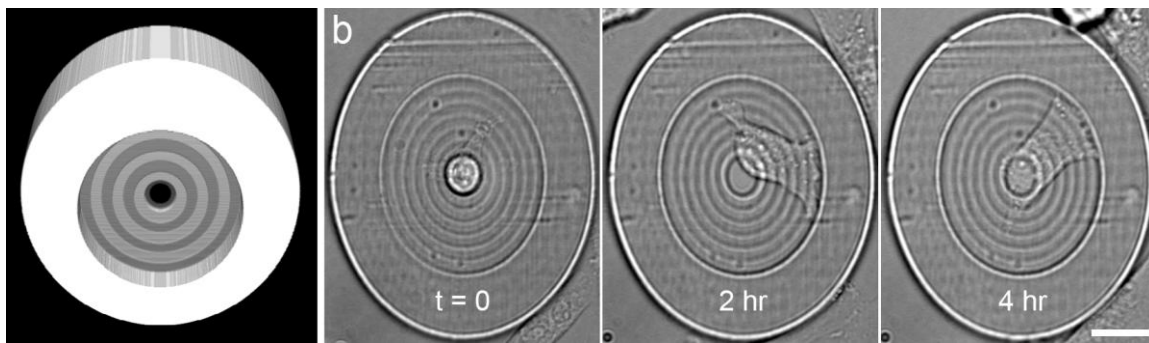


Figure 4.11: Vertical invasion trap. (a) A 3D graphic projection of the digital masks used to create photofabricated container with invasion port in the roof. Interior of the chamber is 10 μm tall. (b) A single MDA-MB-231 breast cancer cell invaded through a $\sim 10\text{-}\mu\text{m}$ -wide opening in the roof and migrated within the chamber. Total time = 4 hours. Scale bar = 20 μm .

4.4 CONCLUSIONS

This chapter presented a technique based on multiphoton fabrication for creating biocompatible protein microstructures to study the migration and invasion of cells in culture. The protein microstructures were biocompatible for a wide variety of cell types and allowed direct observation of single-cell invasion dynamics in materials that better mimic biological tissue. Future work will focus on creating true 3D invasion assays and collecting meaningful statistical samples that provide novel information on invasion. For example, it is not well understood whether the metastatic behavior of tumor cells is determined by development of invasive behavior across the cell population under stress [32] or led by a metastatic phenotype selected and passed through multiple generations [33]. These issues could be investigated on a single-cell level using this technique. Additionally, the ability to acquire fluorescent images of cellular structures during the invasion process would be a significant improvement and would provide more information on cells during invasion (e.g., relative size of the nucleus). Transferring individual cells (e.g., by micromanipulator injection [34]) into enclosed chambers would allow for structures to be transported to dedicated cell biology labs that lack the instrumentation to perform fabrication on site. Chapter 5 focuses on adapting this technique for single-cell isolation and true *in situ* 3D fabrication in the presence of suspended cells.

4.5 REFERENCES

1. Newbold, R. F.; Overell, R. W.; Connell, J. R. Induction of immortality is an early event in malignant transformation of mammalian cells by carcinogens. *Nature* **1982**, *299*, 633–635.
2. Shu, C. J. Visualization of a primary anti-tumor immune response by positron emission tomography. *Proceedings of the National Academy of Sciences* **2005**, *102*, 17412–17417.
3. Arap, W. Cancer treatment by targeted drug delivery to tumor vasculature in a mouse model. *Science* **1998**, *279*, 377–380.
4. Vergara, D.; Merlot, B.; Lucot, J.-P.; Collinet, P.; Vinatier, D.; Fournier, I.; Salzet, M. Epithelial–mesenchymal transition in ovarian cancer. *Cancer Letters* **2010**, *291*, 59–66.
5. Wittekind, C.; Neid, M. Cancer invasion and metastasis. *Oncology* **2005**, *69*, 14–16.
6. Weaver, A. M. Invadopodia: Specialized cell structures for cancer invasion. *Clinical & Experimental Metastasis* **2006**, *23*, 97–105.
7. Carman, C. V.; Sage, P. T.; Sciuto, T. E.; De la Fuente, M. A.; Geha, R. S.; Ochs, H. D.; Dvorak, H. F.; Dvorak, A. M.; Springer, T. A. Transcellular diapedesis is initiated by invasive podosomes. *Immunity* **2007**, *26*, 784–797.
8. Itzstein, C.; Coxon, F. P.; Rogers, M. J. The regulation of osteoclast function and bone resorption by small GTPases. *Small GTPases* **2011**, *2*, 117–130.
9. Kelly, T.; Mueller, S. C.; Yeh, Y.; Chen, W.-T. Invadopodia promote proteolysis of a wide variety of extracellular matrix proteins. *Journal of Cellular Physiology* **1994**, *158*, 299–308.
10. Sarrío, D.; Rodríguez-Pinilla, S. M.; Hardisson, D.; Cano, A.; Moreno-Bueno, G.; Palacios, J. Epithelial-mesenchymal transition in breast cancer relates to the basal-like phenotype. *Cancer Research* **2008**, *68*, 989–997.
11. Duncan, J. R.; Prasse, K. W. Cytology of canine cutaneous round cell tumors. Mast cell tumor, histiocytoma, lymphosarcoma and transmissible venereal tumor. *Veterinary Pathology* **1979**, *16*, 673–679.
12. Boyden, S. The chemotactic effect of mixtures of antibody and antigen on polymorphonuclear leucocytes. *Journal of Experimental Medicine* **1962**, *115*, 453–466.
13. Liu, L.; Sun, B.; Pedersen, J. N.; Aw Yong, K.-M.; Getzenberg, R. H.; Stone, H. A.; Austin, R. H. Probing the invasiveness of prostate cancer cells in a 3D microfabricated landscape. *Proceedings of the National Academy of Sciences* **2011**, *108*, 6853–6856.

14. Karnoub, A. E.; Dash, A. B.; Vo, A. P.; Sullivan, A.; Brooks, M. W.; Bell, G. W.; Richardson, A. L.; Polyak, K.; Tubo, R.; Weinberg, R. A. Mesenchymal stem cells within tumour stroma promote breast cancer metastasis. *Nature* **2007**, *449*, 557–563.
15. Hynes, R. O. Metastatic Potential: Generic predisposition of the primary tumor or rare, metastatic variants - or both? *Cell* **2003**, *113*, 821–823.
16. Mak, M.; Reinhart-King, C. A.; Erickson, D. Microfabricated physical spatial gradients for investigating cell migration and invasion dynamics. *PLoS ONE* **2011**, *6*, e20825.
17. Scherber, C.; Aranyosi, A. J.; Kulemann, B.; Thayer, S. P.; Toner, M.; Iliopoulos, O.; Irimia, D. Epithelial cell guidance by self-generated EGF gradients. *Integrative Biology* **2012**, *4*, 259.
18. Mata, A.; Fleischman, A. J.; Roy, S. Characterization of polydimethylsiloxane (PDMS) properties for biomedical micro/nanosystems. *Biomedical Microdevices* **2005**, *7*, 281–293.
19. Nielson, R.; Kaehr, B.; Shear, J. B. Microreplication and design of biological architectures using dynamic-mask multiphoton lithography. *Small* **2009**, *5*, 120–125.
20. Seidlits, S. K.; Schmidt, C. E.; Shear, J. B. High-resolution patterning of hydrogels in three dimensions using direct-write photofabrication for cell guidance. *Advanced Functional Materials* **2009**, *19*, 3543–3551.
21. Seidlits, S. K.; Khaing, Z. Z.; Petersen, R. R.; Nickels, J. D.; Vanscoy, J. E.; Shear, J. B.; Schmidt, C. E. The effects of hyaluronic acid hydrogels with tunable mechanical properties on neural progenitor cell differentiation. *Biomaterials* **2010**, *31*, 3930–3940.
22. Spivey, E. C. Multiphoton lithography of mechanically and functionally tunable hydrogels. PhD dissertation, University of Texas at Austin, 2012.
23. Kaehr, B.; Allen, R.; Javier, D. J.; Currie, J.; Shear, J. B. Guiding neuronal development with in situ microfabrication. *Proc. Natl. Acad. Sci. U.S.A.* **2004**, *101*, 16104–16108.
24. Connell, J. L.; Wessel, A. K.; Parsek, M. R.; Ellington, A. D.; Whiteley, M.; Shear, J. B. Probing prokaryotic social behaviors with bacterial “lobster traps”. *MBio* **2010**, *1*, e00202-10–e00202-17.
25. Ritschdorff, E. T.; Nielson, R.; Shear, J. B. Multi-focal multiphoton lithography. *Lab on a Chip* **2012**, *12*, 867.
26. Gordon, A. S.; Collier, K.; Diamond, I. Ethanol regulation of adenosine receptor-stimulated cAMP levels in a clonal neural cell line: an in vitro model of cellular

- tolerance to ethanol. *Proceedings of the National Academy of Sciences* **1986**, *83*, 2105–2108.
27. Haemmerli, G.; Arnold, B.; Strauli, P. Comparative morphology of cells located on glass and in the loose connective tissue: A study by scanning electron microscopy. *Cell Biology International Reports* **1984**, *8*, 689–702.
 28. Mahmud, G.; Campbell, C. J.; Bishop, K. J. M.; Komarova, Y. A.; Chaga, O.; Soh, S.; Huda, S.; Kandere-Grzybowska, K.; Grzybowski, B. A. Directing cell motions on micropatterned ratchets. *Nature Physics* **2009**, *5*, 606–612.
 29. Lauffenburger, D. A.; Horwitz, A. F. Cell migration: a physically integrated molecular process. *Cell* **1996**, *84*, 359–369.
 30. Zaman, M. H.; Trapani, L. M.; Sieminski, A. L.; Siemeski, A.; Mackellar, D.; Gong, H.; Kamm, R. D.; Wells, A.; Lauffenburger, D. A.; Matsudaira, P. Migration of tumor cells in 3D matrices is governed by matrix stiffness along with cell-matrix adhesion and proteolysis. *Proceedings of the National Academy of Sciences* **2006**, *103*, 10889–10894.
 31. Kang, Y.; Siegel, P. M.; Shu, W.; Drobnjak, M.; Kakonen, S. M.; Cordon-Cardo, C.; Guise, T. A.; Massagué, J. A multigenic program mediating breast cancer metastasis to bone. *Cancer Cell* **2003**, *3*, 537–549.
 32. Tse, J. M.; Cheng, G.; Tyrrell, J. A.; Wilcox-Adelman, S. A.; Boucher, Y.; Jain, R. K.; Munn, L. L. Mechanical compression drives cancer cells toward invasive phenotype. *Proceedings of the National Academy of Sciences* **2011**, *109*, 911–916.
 33. Sullivan, R.; Graham, C. H. Hypoxia-driven selection of the metastatic phenotype. *Cancer Metastasis Rev.* **2007**, *26*, 319–331.
 34. Lu, Z.; Moraes, C.; Zhao, Y.; You, L.; Simmons, C. A.; Sun, Y. A micromanipulation system for single-cell deposition. In: IEEE, 2010; 494–499.

Chapter 5: In Situ Photofabrication of Eosin-Conjugated Gelatin Microstructures for Single-Cell Trapping

5.1 INTRODUCTION

Divergence within single-cell behavior amongst a large cell population, as a result of phenotypic variations, plays an important role in many biological processes (e.g., development [1], adaptation [2], and disease [3]). Both intrinsic (e.g., low-copy number DNA [4], intracellular crowding effects on molecular diffusion and biochemical equilibria [5]) and extrinsic (e.g., cellular age [6], extracellular matrix effects [7]) variations affecting single-cell gene expression within clonal populations creates heterogeneity that is vital for the survival and development of isogenic groups of cells [8]. For example, phenotypic variations within cancer-cell populations leads to low-frequency variants that exhibit atypical tolerance to targeted chemotherapy by drug efflux [9], drug-binding deficiency [10], and reversible drug-resistant chromatin alterations [11]. The contribution and significance of these single-cell effects are often masked by population averaging in bulk cell analysis techniques (e.g., microplate assays) and studying them requires techniques that provide both spatial resolution and temporal flexibility on the scale of a single cell.

Various microfluidic and fabrication techniques have been developed for single-cell sorting and analysis. Multi-layer PDMS isolation chambers [12], nanowire cages [13], and magnetic microrrafts [14] have all been recently developed for the purpose

of physically isolating and analyzing single cells. These approaches provide a way to physically isolate single cells while maintaining chemical signaling and diffusion of reagents between separated cells, but each technique is limited to a pre-fabricated geometry and there is little control over the characteristics of cells that are trapped.

Microfluidic approaches have also been used for single-cell handling and lysate analysis [15]. Hydrodynamic focusing [16], droplet microfluidics [17], and responsive microfluidic valves [18] are all useful tools within microfluidic platforms for high-throughput manipulation of single cells. In certain geometries, these microfluidic traps can serve as perfusion chambers after trapping a single cell, where fluorescently labeled cells can be chemically manipulated and observed [19]. The inherent limitation of these techniques is that device fabrication and cell manipulation are separate steps that limit the spatial and temporal adaptability of the technique to single-cell characteristics. Additionally, cells must be pre-loaded in each of these approaches, thus limiting the possibility of true 3D isolation of a single cell.

In the Shear Lab, *in situ* multiphoton fabrication has been used to direct somatic-cell growth and to isolate bacteria. In 2004, Kaehr, et al. presented a technique for fabricating BSA lines with flavin adenine dinucleotide (FAD), a type I photosensitizer, to direct neurite outgrowth from NG108-15 cells, as well as cortical neurons. These structures were low-profile, lineographic barriers along the surface of the glass for altering cell outgrowth. In his dissertation [21], Kaehr acknowledged that FAD-sensitized BSA lines lacked the uniformity and reproducibility of microstructures fabricated with more robust sensitizers and that taller structures fabricated by layering FAD-sensitized

BSA lines generally resulted in decreased viability of cells post-fabrication. The combination of fragile crosslinking and the apparent cytotoxicity of larger structures makes FAD-sensitized BSA fabrication a nonideal candidate for *in situ* photofabrication of structures for single-cell isolation. In her 2012 dissertation [22], Jodi Connell first presented a technique where bacteria were suspended in gelatin with type II photosensitizers. In these studies, the gelatin was allowed to thermally set at room temperature, presumably limiting diffusion of phototoxic species during fabrication. After fabricating microstructures around the bacteria, the uncrosslinked gelatin was rinsed away by 37°C media, leaving behind viable bacteria within robust 3D protein microstructures. Chapter 5 describes the development of gelatin-based fabrication techniques for creating 3D microstructures around somatic cells, specifically for the isolation of single somatic cells, by covalently binding a type-II photosensitizer to the gelatin prior to fabrication.

5.2 EXPERIMENTAL METHODS

5.2.1 Eosin Conjugation

Eosin-conjugated gelatin was prepared by reacting eosin-5-isothiocyanate with type A gelatin. In the preparation, 100 mg of type A gelatin was dissolved in 10 mL of 0.1 M sodium bicarbonate buffer (pH = 9) and 10 mg of eosin-5-isothiocyanate was dissolved in 1 mL of filtered (0.22 µm) DMSO, and the two solutions were combined in a 25 mL Erlenmeyer flask at ambient temperature (~20°C) and mixed for ~24 hours. The solution was then transferred to an 8-10 kDa (MWCO) cellulose ester dialysis cassette (G235067; Spectrum Laboratories, Inc.) and dialyzed for ~24 hours in 3 L of 0.1 M

sodium bicarbonate buffer (pH = 9). After dialysis, the solution was transferred to a 50 mL centrifuge tube and lyophilized at -50°C and 0.10 mbar for ~48 hours in a FreeZone[®] 4.5-liter benchtop freeze dry system (Labconco Corp., Kansas City, MO). As determined by measured absorbance at 520 nm ($\epsilon = 78,000 \text{ M}^{-1} \text{ cm}^{-1}$), the lyophilized powder contained ~1 mmol of eosin per 15 grams, or ~5 eosin molecules per gelatin fragment, on average.

5.2.2 Fabrication Solution

Fabrication solutions were prepared from eosin-conjugated gelatin, type A gelatin, and BSA in L-15 (Leibovitz) media. To prepare solutions, 10-15 mg of BSA was added to 500 μL of L-15 media in a 1.5 mL microcentrifuge tube and mixed on a thermomixer for ~15 minutes at 37°C and 1000 RPM. After dissolution of the BSA, 30-40 mg of eosin-conjugated gelatin was added to the solution and the tube was placed in an oven for ~5 minutes at 60°C. The tube was then returned to the thermomixer and mixed at 37°C and 1000 RPM for ~1 hour. Following dissolution of the conjugated gelatin, 40-70 mg of unconjugated type A gelatin was added to solution and the tube was transferred to an oven for ~5 minutes at 60°C. The tube was then transferred to the thermomixer and mixed at 37°C and 1,000 RPM for at least 1 hour. Prior to fabrication, 150 μL of solution was filtered in a 0.22 μm PVDF centrifugal filter unit (Millipore, Billerica, MA) at an RCF of 16,100 g for 15 minutes, resulting in ~100 μL of fabrication solution. The filtered solution was maintained at 37°C until immediately before cells were added.

5.2.3 Cell Culture

Mouse neuroblastoma-rat glioma (NG108-15) hybrid cells and MDA-MB-231 human breast cancer cells, originally purchased from the American Type Culture Collection (ATCC), were stored in their normal growth media supplemented with 5% (v/v) dimethyl sulfoxide (DMSO) at concentrations of approximately 500,000 cells mL⁻¹ in liquid nitrogen until they were needed for culture. Mouse leukaemic monocyte macrophage cells (RAW 264.7) were a generous donation from Dr. Krishnendu Roy (Department of Biomedical Engineering, University of Texas at Austin). When thawed, NG108-15 cells were cultured in Dulbecco's Modified Eagle's Medium (DMEM; Corning Cellgro) supplemented with 10% (v/v) fetal bovine serum (HyClone, AVJ82746), 1% (v/v) penicillin/streptomycin (MP Biomedicals), and 1X HAT (1.0×10^{-4} M hypoxanthine, 2.0×10^{-7} M aminopterin, 1.6×10^{-4} M thymidine; 50X HAT solution was purchased from MediaTech). MDA-MB-231 cells were cultured in Roswell Park Memorial Institute (RPMI 1640; HyClone) medium supplemented with 10% (v/v) fetal bovine serum. Flasks were maintained at 37°C in a 5% CO₂ atmosphere at 100% relative humidity with media replacement every two days and cells were passaged to a new flask every 4-5 days (depending on confluence) for up to 40 total passages. RAW 264.7 cells were stored in 10% (v/v) FBS DMEM at 37°C in a 5% CO₂ atmosphere and passaged by gently scraping the culture plastic surface and diluting cell solution at a 1:10 ratio with media in a new culture flask.

5.2.4 Cell Preparation for Fabrication

For *in situ* fabrication, a coverslip-bottom 35 mm petri dish (P35G-1.5-14-C; MatTek Corp.) was coated with 1.0 mg mL⁻¹ rat-tail collagen (BD Biosciences, 354249) in a 30% ethanol/70% water (v/v) mixture for at least 4 hours prior to plating. These dishes provided a 14-mm fabrication region (no. 1.5 coverslip) and allowed for large rinsing volumes (4-5 mL) within the entire petri dish. Collagen solution was removed at least 30 minutes prior to fabrication and the dish was allowed to air dry. Immediately prior to fabrication, cells were passaged from a confluent flask and centrifuged at an RCF of 150 g. The cell pellet was then reconstituted in media (L-15 for non-CO₂ experiments; DMEM or RPMI for CO₂ experiments) to a concentration of $\sim 2 \times 10^6$ cells mL⁻¹ for suspension in gelatin fabrication solution. 20 μ L of cell solution were then transferred into ~ 100 μ L of filtered gelatin fabrication solution (cell concentration $\sim 3 \times 10^5$ cells mL⁻¹) and 10 μ L (~ 3000 cells) were immediately transferred to the center of each fabrication dish. In early iterations of these experiments, the dishes were cooled to 4°C until ready for fabrication. However, it is known that storage at refrigerated temperatures may affect cell viability [23] and at the concentrations used for these studies, gelatin will thermally set at room temperature ($\sim 20^\circ\text{C}$) after 5-10 minutes. As a result, gelatin fabrication solutions were allowed to thermally set at room temperature during later studies.

5.2.5 Multiphoton Fabrication

The process used for photofabrication of 3D protein microstructures is an adaptation of the instrumentation initially presented by Ritschdorff, et al. in 2012 [24].

Here, the collimated beam of a mode-locked titanium:sapphire laser (Coherent Mira 900), tuned to 740 nm, was aligned to a two-axis galvanometer-driven scan mirror (Leica TCS-4D, Bensheim, Germany) that raster-scanned the beam at 0.1 Hz on the slow axis and 110.0 Hz on the fast axis across an 800×600 digital micromirror device (DMD) from a DLP projector (BenQ, MP510). Each mirror ($\sim 16 \mu\text{m} \times \sim 16 \mu\text{m}$) within the DMD chip was individually adjusted to the “on” (white) or “off” (black) position by its corresponding pixel in a binary mask displayed by the controlling PC. Mirrors in the black position redirected the beam to a beam block while mirrors in the white position directed the beam to overfill the back aperture of a 1.30 numerical aperture (NA) 40X Zeiss Plan-NeoFluar oil-immersion microscope objective. By positioning the DMD in a plane conjugate to the specimen plane of the objective, a 1:1 mapping was achieved between the DMD display and the fabrication pattern in solution at a magnification equal to that of the objective (40X). 3D objects were fabricated within the solution by synchronizing optical axis steps of the microscope stage with changes in the mask displayed to the DMD using software written in LabView™ (National Instruments, Austin, TX), where each individual mask corresponded to a single layer of fabrication in solution.

Fabrication was performed on a Zeiss Axiovert 135 inverted microscope equipped with a three-axis translational stage (562, Newport Corp., Irvine, CA) driven by motorized actuators (LTA-HS, Newport Corp., Irvine, CA) that were controlled using a motion driver (ESP300, Newport Corp., Irvine, CA). Binary masks were created using Adobe Photoshop and ImageJ (National Institutes of Health, Bethesda, MD).

After fabrication, the dishes were then transferred to the microscope stage in a home-built environmental chamber (see **2.2.6 Environmental Chamber**) set to maintain cell culture conditions at ~35 °C and ~45% relative humidity. The dish was filled with ~4 mL of media in the incubation chamber at ~35°C, allowing uncrosslinked gelatin to slowly disperse. For the first hour after fabrication, dishes were gently rinsed (2 mL removed, 2 mL of fresh solution added) with media every 15 minutes. After the first hour, dishes were rinsed with media once every hour until five hours post-fabrication, when dishes were rinsed as necessary for the next 24-48 hours.

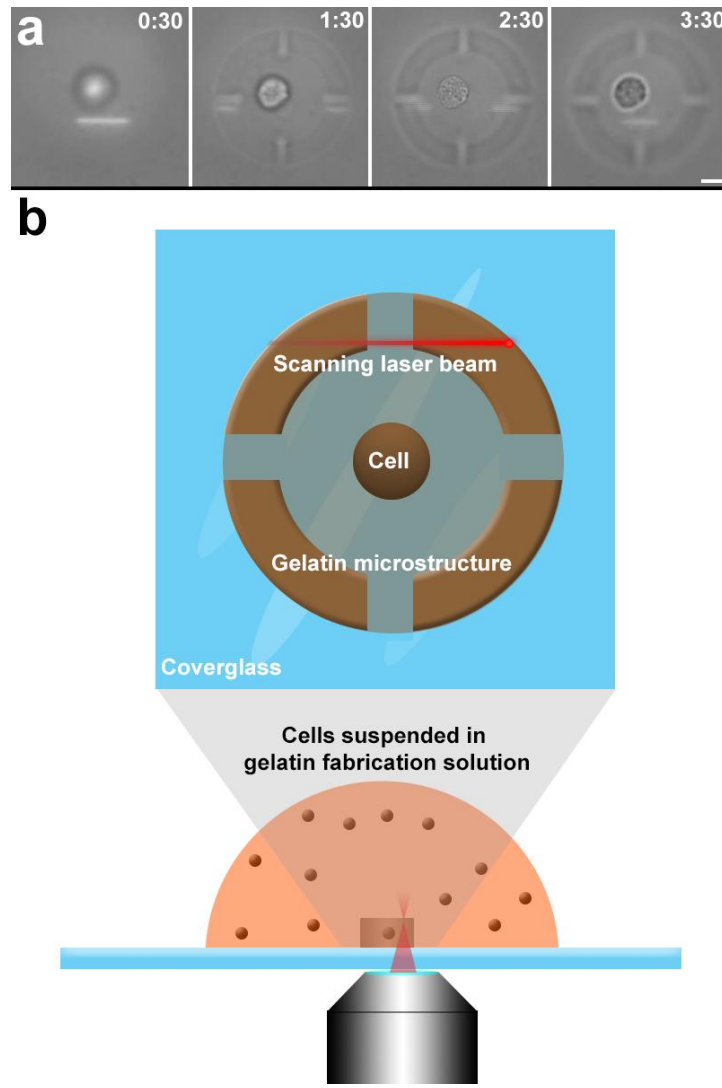


Figure 5.1: In situ fabrication. Gelatin microstructures were photofabricated around suspended cells in eosin-conjugated gelatin. (a) A vented sphere was fabricated layer-by-layer around a suspended MDA-MB-231 breast cancer cell. Time from the beginning of fabrication (minutes:seconds) is listed in the upper right corner of each image. Total time for fabrication = 4 minutes. Scale bar = 10 μm (b) A graphic showing the fabrication of a protein microstructure around a single cell amongst a distributed population of suspended cells in thermally set gelatin-based fabrication solution. As the laser beam scans through solution in a user-defined pattern, gelatin is crosslinked at the focal volume in the same pattern.

5.2.6 Microscopy

Brightfield images were acquired on a Zeiss Axiovert 135 inverted microscope equipped with an incubation chamber using either a 10X objective (Zeiss Fluor 0.5 NA), 20X objective (Zeiss Plan-Neofluar 0.5 NA), or 40X objective (Olympus UPlanFl 0.75 NA) with a Hamamatsu Orca II CCD camera (C4742-98) controlled by MetaMorph Imaging Software (Molecular Devices). Images were acquired once every 1-5 minutes with exposure times of 10-200 ms. Illumination was shuttered between acquisitions by a pulsed Uniblitz UHS1 shutter (Vincent Associates, VMM-T1).

5.2.7 Chemicals

Bovine serum albumin (BAH64) was purchased from Equitech-Bio (Kerrville, TX). Type A gelatin from porcine skin (G2500) and L-ascorbic acid (95210) were purchased from Sigma-Aldrich (St. Louis, MO). Eosin-5-isothiocyanate (E-18) was purchased from Molecular Probes (Eugene, OR). All reagents were used as received without purification.

5.3 RESULTS AND DISCUSSION

5.3.1 In Situ Fabrication with Eosin-Conjugated Gelatin

Initial attempts at *in situ* fabrication were modeled after the technique initially described by Connell for fabricating microstructures around bacteria suspended in gelatin [22]. Briefly, NG108-15 cells were cultured in collagen-coated wells for ~1 hour to ensure attachment to the surface. The cell media was then removed and replaced with a fabrication solution of ~100 mg mL⁻¹ gelatin, ~25 mg mL⁻¹ BSA, and ~5 mM photosensitizer (rose bengal or eosin). After allowing the gelatin to thermally set at room

temperature (~15 minutes), 50- μ m inner-diameter cylindrical microchambers were fabricated around single cells. After fabrication, dishes were transferred to an incubation chamber and uncrosslinked gelatin was slowly rinsed away using warm (~35°C) media. Over multiple attempts with NG108-15 cells, however, the cells displayed no apparent characteristics of viability (e.g., motility, morphological changes) after the gelatin was dispersed. Because cells appeared to have perished by necrosis (swelling of cellular structures, absence of apoptotic bodies, no fragmentation), it was determined that acute cell injury was occurring during fabrication due to cellular internalization of the photosensitizing species.

To address the phototoxicity of fabrication, eosin (a type II photosensitizer) was covalently bound to the gelatin prior to fabrication. It was hypothesized that the sensitizer-conjugated gelatin would limit cellular endocytosis of the relatively small photosensitizing molecule (eosin = 0.7 kDa; eosin-conjugated gelatin = 50-100 kDa¹), reducing phototoxicity of the fabrication solution. Eosin-5-isothiocyanate is an amine-reactive fluorescent probe commonly used to label proteins at lysine residues and as a phosphorescent probe for studying the rotational dynamics of cell surface receptors [25]. Gelatin is 4.3% lysine (by weight) [26], providing a number of sterically available, nucleophilic, primary amines along with the α -amine at each N-terminus. Consequently, there are 20-40 potential isothiocyanate reaction sites per fragment of gelatin. Eosin-5-isothiocyanate reacts by nucleophilic addition at the central carbon of the isothiocyanate

¹ Gelatin is produced by the hydrolysis of collagen and consists of a range of molecular weight fragments from the various collagen chains.

with the ϵ -amine of the lysine residue to form a stable thiourea derivative that maintains the photosensitizing properties of the eosin (Figure 5.2) [27]. The preparation of eosin-conjugated gelatin, as described in section 5.2.1, produced ~ 1 mmol eosin per 15 grams of gelatin, or ~ 5 eosin molecules per gelatin fragment, on average.

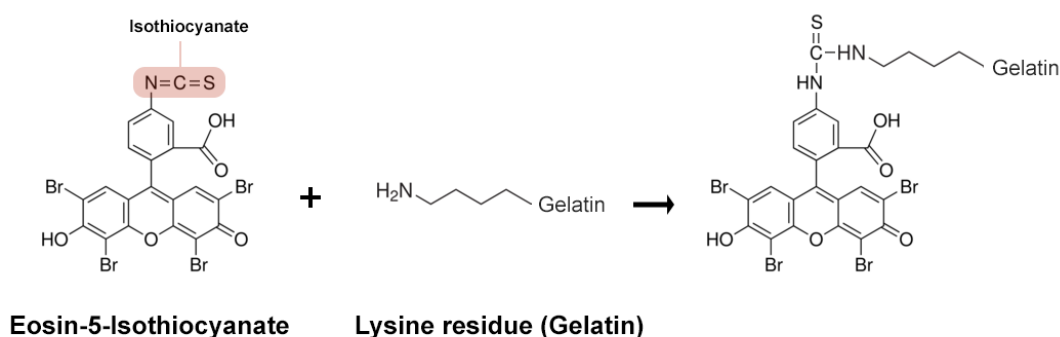


Figure 5.2: Eosin conjugation. Eosin-5-isothiocyanate was used to label the lysine residues on type A gelatin by nucleophilic addition forming a relatively stable thiourea product with no leaving group. Eosin maintained its photosensitizing capabilities when covalently bound to gelatin with a reduction in cytotoxicity as the result of reduced cellular internalization of the relatively large sensitizer-conjugated gelatin fragment (50-100 kDa).

Fabrication solutions for these studies were prepared using a mixture of unconjugated and conjugated forms of gelatin in solution at a ratio of $\sim 2:1$ (unconjugated:conjugated), as solutions consisting of eosin-conjugated gelatin alone appeared to partially crystallize during thermal gelation. Control studies examining the inherent cytotoxicity of gelatin, eosin-conjugated gelatin, and BSA, as well as combinations of all three, showed no apparent effects on NG108-15 cell viability when

the cells were incubated overnight in the respective concentrations of each reagent used for fabrication. In contrast, NG108-15 cells that were incubated overnight in eosin (5 mM in cell media) showed significantly higher death rates, less differentiation, and more rounded morphology compared to controls with no added eosin.

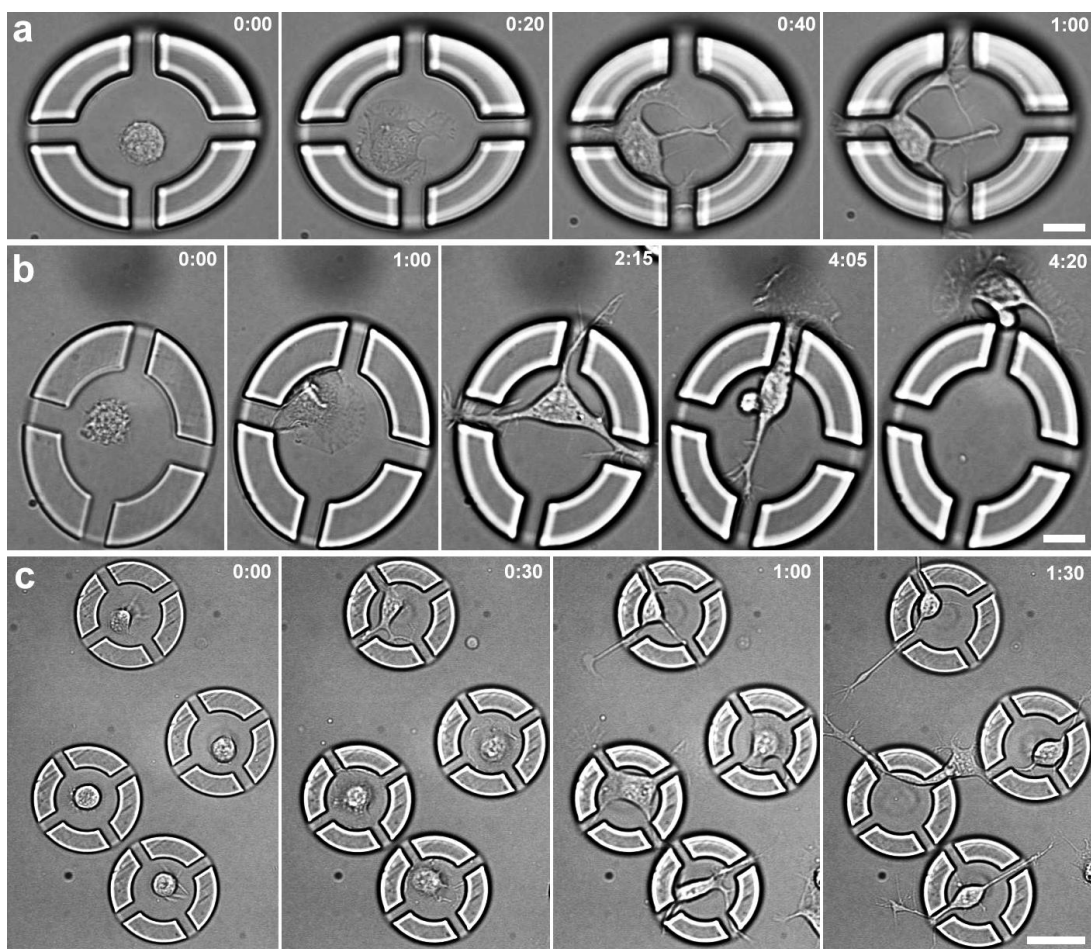


Figure 5.3: Single-cell trapping. NG108-15 cells displayed post-fabrication viability in gelatin cylindrical microstructures (30 μm tall with a 4- μm -thick roof) that were fabricated in the presence of the cells suspended in gelatin-based fabrication solution. (a) A single NG108-15 cell settled to the surface as uncrosslinked gelatin was rinsed away and the cell migrated towards the edge of its containing structure (fabricated from a solution of 77 mg mL^{-1} eosin-gelatin, 25 mg mL^{-1} BSA, and 102 mg mL^{-1} gelatin). Scale bar = 20 μm . (b) A single NG108-15 cell differentiated within the gelatin structure (same fabrication solution as part (a)) then migrated through an opening in the structure. Scale bar = 20 μm . (c) Four NG108-15 cells were contained within gelatin microstructures in close proximity. The cells extended neurite-like processes through openings in the structures (fabricated from a solution of 60 mg mL^{-1} eosin-gelatin, 25 mg mL^{-1} BSA, and 90 mg mL^{-1} gelatin). Scale bar = 50 μm . Images were acquired once per minute with exposure times of ~ 100 ms. Cells were cultured in 0% FBS L-15 media during each timelapse. Time shown in the upper right of each individual frame is hours:minutes from the beginning of the sequence.

Initial attempts at *in situ* fabrication around somatic cells with the eosin-conjugated gelatin produced robust microstructures with cells (NG108-15) that survived for moderate time periods (hours) after the uncrosslinked gelatin was removed (Figure 5.3). These results were the first known demonstration of biocompatible type-II-sensitized photofabrication in the presence of somatic cells. After fabrication, cells displayed typical morphology and motility while also interacting with microstructures in a similar fashion to cells plated around pre-fabricated microstructures (Chapter 4). Unfortunately, these isolated cells also displayed apparent apoptosis (programmed cell death) within 2-12 hours after rinsing, characterized by blebbing (localized protusions on the plasma membrane due to rupture of the F-actin cortex [28]) and fragmentation of the cell (Figure 5.4). Apoptosis is a naturally occurring, self-initiated form of cell death that the body uses to regulate cell number and distribution that occurs in response to local chemical signals (e.g., glucocorticoids [29], tumor necrosis factor (TNF- α) [30]) and cellular stress (e.g. hypoxia [31], hyperthermia [32]). Importantly, these observations suggested that fabrication with cells suspended in conjugated gelatin was not inherently cytotoxic in the same fashion as photofabrication with free photosensitizer, and that reduction of post-fabrication cellular stress could allow for long-term observation of isolated cells in close proximity to microstructures fabricated in the presence of these cells.

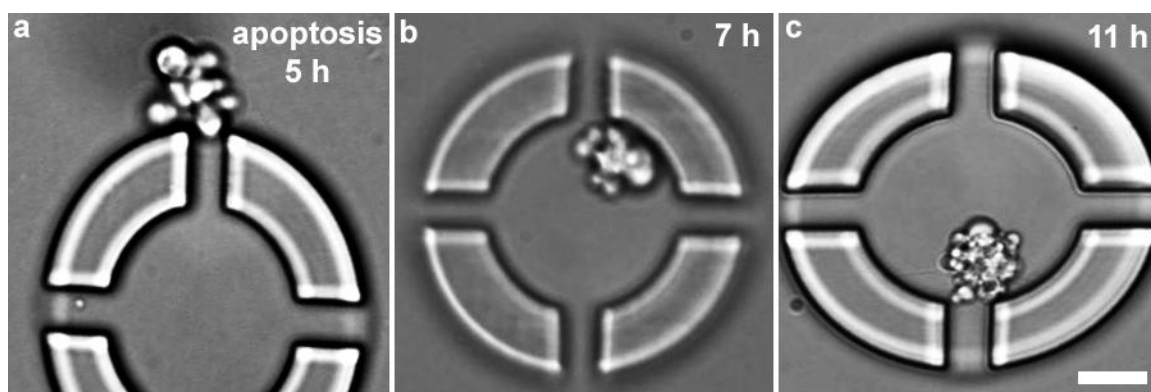


Figure 5.4: Apoptosis. Gelatin-based cylindrical microstructures fabricated around suspended NG108-15 cells initially resulted in apoptosis (programmed cell death). After migrating within and around the microstructures for 2-12 hours, cells underwent rapid apoptosis. (a-c) NG108-15 cells shown within five minutes after apoptosis following 5- (a), 7- (b), and 11- (c) hour migration within eosin-gelatin microstructures. Scale bar (applies to all panels) = 20 μm .

5.3.2 Reducing Post-Fabrication Cytotoxicity

Post-fabrication cytotoxicity observed with *in situ* fabricated microstructures in these studies was likely due to the illumination-mediated excitation of photosensitizer in close proximity to the cell, resulting in the cell damage or stress that led to apoptosis. While cells within microchambers could be cultured in a dark incubator, long-term observation after fabrication necessitated periodic illumination during imaging. To minimize the effects of illumination, a long-pass filter was added to the illumination column to minimize the overlap of illumination wavelengths and photosensitizer excitation wavelengths. In combination with the microscope's IR filter, illumination wavelengths were thus limited to 600-750 nm (Figure 5.5a). In addition to filtering the illumination wavelengths, an extrinsic radical-quenching agent (L-ascorbic acid) was

added to the cell culture medium to minimize the effects of singlet oxygen generation in solution. Many different cell media (e.g., McCoy's 5A, Waymouth's MB 752, CMRL 1066) include ascorbic acid (vitamin C) as a nutritional supplement (e.g., as an essential cofactor in collagen biosynthesis [33]) or an antioxidant (e.g., limiting lipid peroxidation [34]). Of note, ascorbate degrades in aqueous solution at physiological pH and temperature [35] and was freshly prepared prior to each experiment.

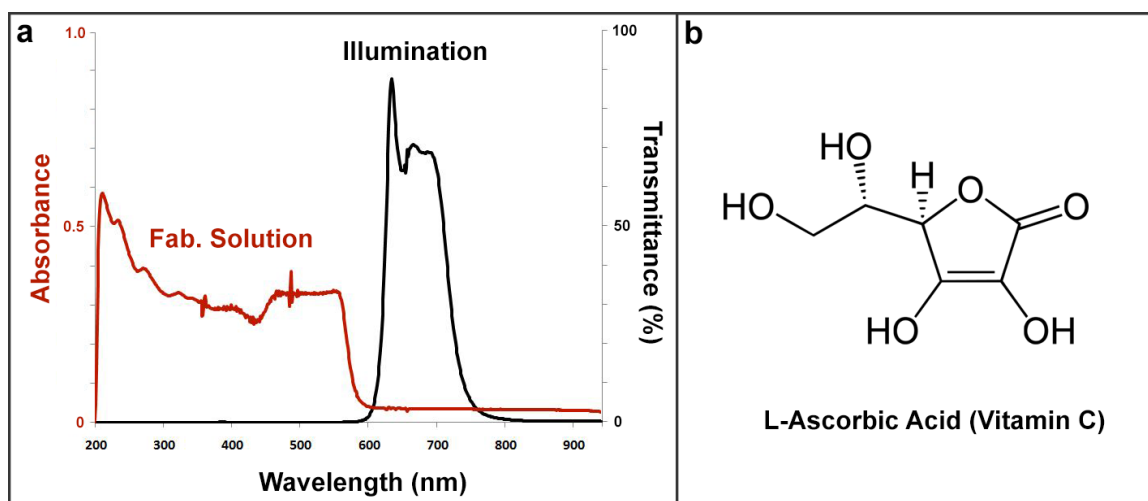


Figure 5.5: Reducing post-fabrication cytotoxicity. (a) (black) A combination of filters was included in the illumination path for eliminating potentially damaging IR exposure as well as reducing the strongest excitation wavelengths of the fabrication solution (red). (b) Low levels ($50 \mu\text{M}$) of L-ascorbic acid (Vitamin C) were also included in medium as a singlet-oxygen quencher and radical scavenger.

Supplementing the cell media with ascorbate, in combination with the filtered illumination, increased cell survival periods within the *in situ* photofabricated microstructures beyond 48 hours, and up to one week in some instances (longer times were not investigated). Importantly, cells inside these isolated microstructures underwent

mitosis when supplied with their normal culture medium (Figure 5.6), a strong indicator that their chromatin was not compromised and that cells could proceed through the cell cycle. For longer experiments (>24 hours), a system was constructed with a syringe pump supplying media, through platinum-cured silicone tubing (Cole-Parmer, 95802-01) inserted in the roof of the dish, at a rate of 0.05 mL min^{-1} and a separate syringe pump removing media from the opposite side of the dish at a rate of 0.04 mL min^{-1} to combat evaporation within the incubation chamber (~45% relative humidity). As a precaution against the excitation of residual photosensitizer, the image acquisition rate was reduced from once every minute to once every 5-15 minutes. These acquisition rates were sufficient for capturing relevant data without a significant loss in temporal resolution while minimizing light exposure. NG108-15 cells were conditioned for ascorbate-containing media by including $50 \text{ }\mu\text{M}$ ascorbate in their growth medium (10% FBS DMEM) for two days prior to fabrication experiments.

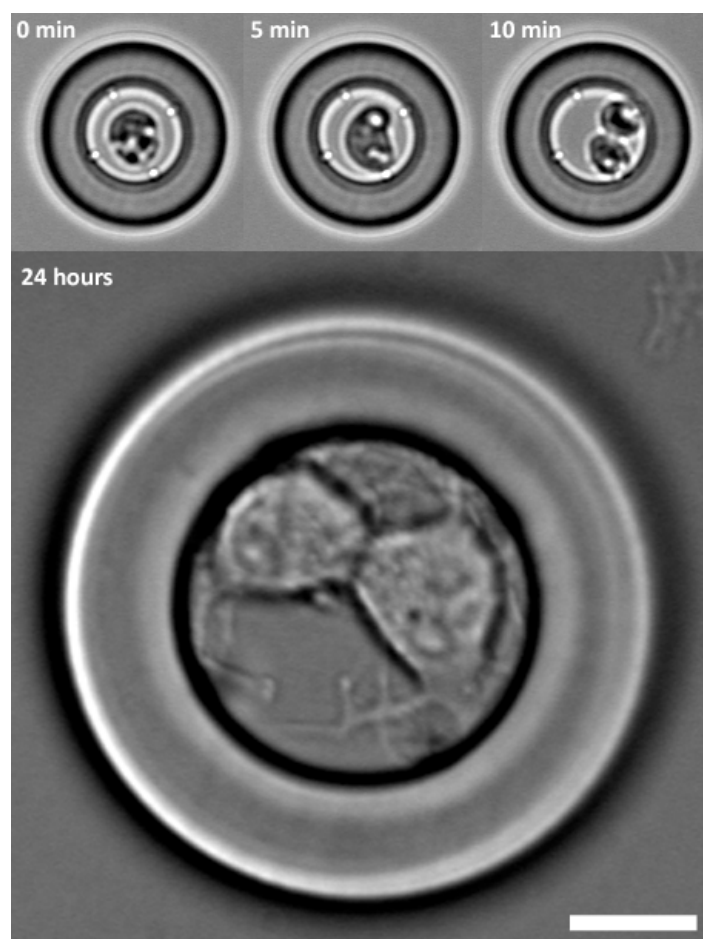


Figure 5.6: Cell division. A single NG108-15 cell divided within an isolated cylindrical gelatin-based microchamber with no cell exit paths (four 2- μm -diameter holes in the roof to aid gelatin removal post-fabrication). Both daughter cells remained viable for the duration of the experiment (24 hours) after division. Images were acquired once every 5 minutes. Cells were cultured in 10% FBS DMEM media supplemented with 50 μM ascorbate in 5% CO_2 at $\sim 35^\circ\text{C}$. Fabrication solution = 68 mg mL^{-1} eosin-gelatin, 26 mg mL^{-1} BSA, 130 mg mL^{-1} gelatin. Scale bar = 20 μm .

Abnormal division events, such as aneuploid division (more than 2 progeny) and re-fusion of daughter cells, were also observed within photofabricated gelatin microchambers. These effects may be due to the constrained volume experienced by the cell, as it has been shown that physical stress on a dividing cancer cell can cause the cell

to bypass checkpoints for conventional mitosis (e.g., properly aligning chromosomes), resulting in as many as five progeny from a single mitosis event [36]. Figure 5.7 shows a single NG108-15 cell that divided into three daughter cells that all survived within the microfabricated chamber through the end of the experiment (16 hours after division). These results suggest that *in situ* photofabricated microchambers could be used to study abnormal mitosis, specifically with cancer cells where abnormal division contributes to damaging behavior (e.g., cell overgrowth, metastasis). Future work will focus on the specific effects of constrained volumes on cell division as well as behavior of these progeny after unconventional mitosis.

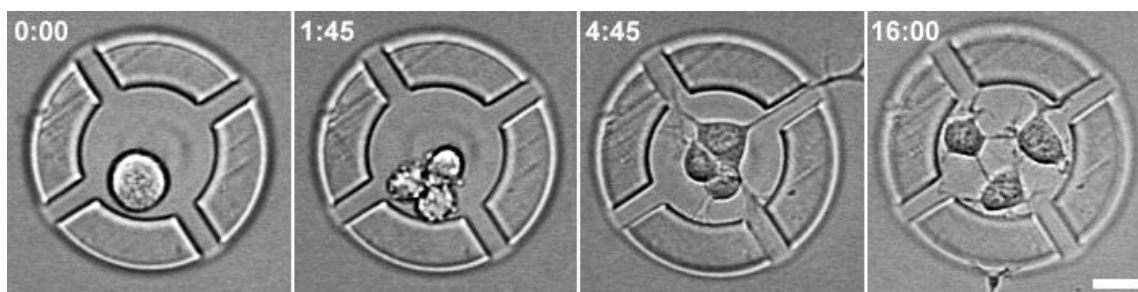


Figure 5.7: Aneuploid division. A gelatin-based cylindrical microchamber (30 μm tall with a 4- μm -thick roof) fabricated around a single NG108-15 cell. The cell divided into three progeny that survived for 16 hours after division. Images were acquired once every 15 minutes. Time in the upper left corner of each image is hours:minutes from the beginning of the timelapse sequence. Cells were cultured in 0% FBS L-15 supplemented with 50 μM ascorbate. The microstructure was fabricated from a solution of 60 mg mL^{-1} eosin-gelatin, 25 mg mL^{-1} BSA, and 90 mg mL^{-1} gelatin. Scale bar = 20 μm .

5.3.3 In Situ Fabrication in the Presence of Human Cells

Cell types other than NG108-15 displayed similar viability after *in situ* fabrication of eosin-conjugated gelatin, including MDA-MB-231 human breast cancer cells. These

cells exhibited similar morphology and motility through 10- μm -wide gaps with *in situ* fabricated gelatin microstructures as they displayed around and within pre-fabricated gelatin structures (Section 4.3.4). Figure 5.8 shows a pair of MDA-MB-231 cells isolated within a photofabricated eosin-gelatin microchamber that migrated in and out of the structure multiple times over the course of ~ 28 hours. This cell type maintained viability through the entire course of 48-hour experiments and they did not require ascorbate conditioning. Future work will focus on invasion assays of this cell type, where initial results suggest that individual cells can manipulate small ($\leq 2 \mu\text{m}$) openings in gelatin microstructures over a period of hours to escape physical isolation.

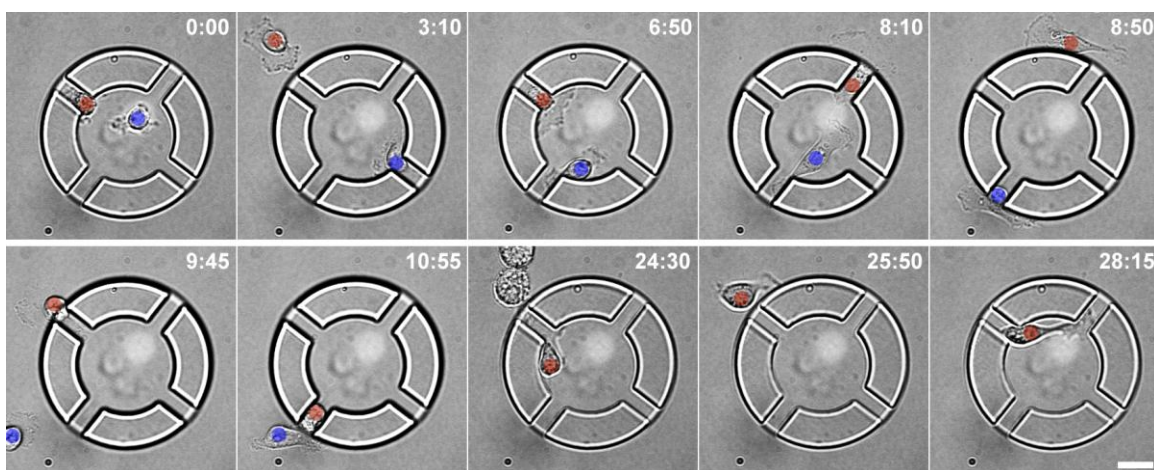


Figure 5.8: MDA-MB-231 isolation. A cylindrical gelatin microchamber (30 μm tall with a 4- μm -thick roof) was fabricated around two different MDA-MB-231 breast cancer cells in close proximity. Over the course of 30 hours of imaging, one of the cells (red marker) migrated in and out of the structure eight times. The other cell (blue marker) migrated out of the structure and then out of the field of view. Images were acquired once every 5 minutes. Time in the upper right corner of each image is hours:minutes from the beginning of the timelapse sequence. Cells were cultured in 10% FBS L-15 supplemented with 50 μM ascorbate. Microstructure was fabricated from a solution of 72 mg mL^{-1} eosin-gelatin, 26 mg mL^{-1} BSA, and 92 mg mL^{-1} gelatin. Scale bar = 20 μm .

5.3.4 Complete 3D Isolation of Single Cells

In contrast to most *in vitro* studies, cells *in vivo* are surrounded in all dimensions by biological material in a highly specific fashion, a condition that is not easily replicated in cell culture. For pre-fabricated materials, it is nearly impossible to isolate cells in all three dimensions. Soft lithography and molding techniques lack the axial resolution to create truly 3D structures and photolithographic techniques, such as those demonstrated in Chapter 4, require openings within pre-fabricated microstructures that rely on migration of the cell into the structure. Conjugated-gelatin allows for the construction of truly 3D and free-floating gelatin microstructures around cells that remain completely viable after rinsing by suspending the cells within gelatin-based fabrication solution and allowing the solution to thermally set around the cell suspension. Figure 5.9 shows a complete 3D isolation chamber that was fabricated around an NG108-15 cell suspended in gelatin. The cell was trapped within an orb-shaped structure and attempted to migrate through narrow openings in the walls of the structure before getting trapped. Because the cells in these studies were suspended above the surface within the gelatin-based fabrication solution, material could be fabricated above and below individual cells. The dynamic layer-by-layer fabrication technique used here allowed for fabrication masks to be altered during the experiment to tailor the shape and size of the microstructure to each cell, as well as adapting to cells at various depths within the 10 μ L drop of fabrication solution.

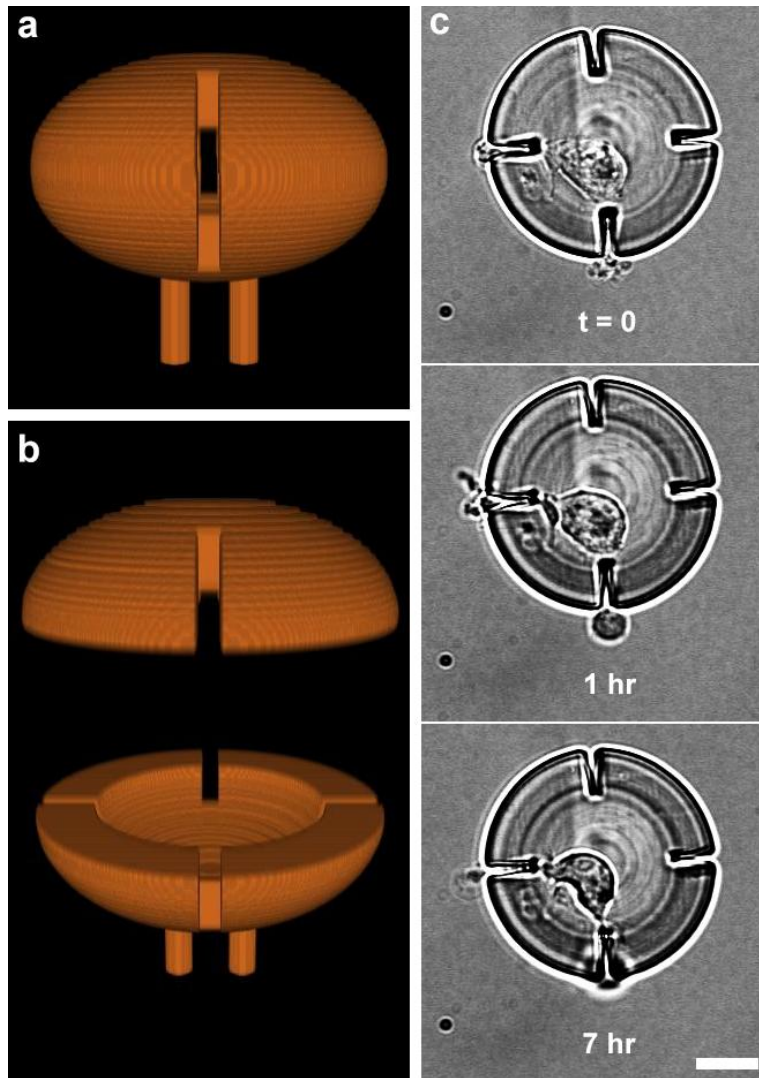


Figure 5.9: 3D isolation. Single cells could be placed in true 3D isolation by *in situ* fabrication of conjugated-gelatin. (a) A 3D projection graphic of the masks used to fabricate a 3D isolation orb attached to the surface by 2 adjacent posts. (b) Exploded version of the graphic from part (a) showing the negative space within the orb-shaped structure. (c) A single NG108-15 cell enclosed within the isolation orb shown in parts (a) and (b). The cell attempted to migrate out of the structure through narrow openings in the wall and became trapped. Images were acquired once per minute. Cells were cultured in 0% FBS L-15 media supplemented with 50 μM ascorbate. The microstructure was fabricated from a solution of 72 mg mL^{-1} eosin-gelatin, 26 mg mL^{-1} BSA, and 92 mg mL^{-1} gelatin. Scale bar = 20 μm .

In addition to anchored 3D microstructures for single-cell confinement, gelatin also allowed for free-floating microstructures to be fabricated around single cells. Because of the high viscosity of the gelled fabrication solution, layers of fabricated material remained stationary during fabrication relative to the scan speeds (5 seconds per layer; 3-4 minutes per microstructure), whereas similar materials would shift during fabrication in a liquid-based reagent. Figure 5.10 shows a free-floating hollow 3D sphere fabricated around a suspended MDA-MB-231 cell. The sphere was contained within a fully enclosed rectangular box anchored to the surface so that the structure remained constrained within a defined volume during removal of uncrosslinked gelatin. The cell migrated within the confined region, occasionally causing the entire sphere to slightly rotate.

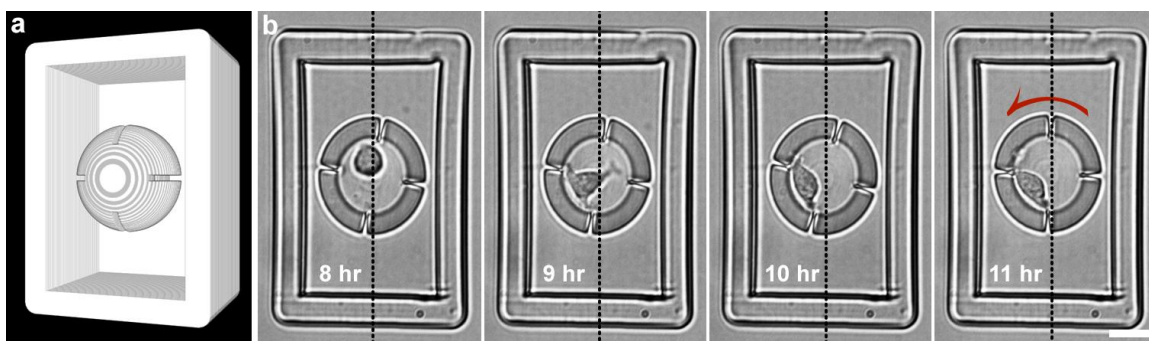


Figure 5.10: Free-floating 3D isolation. Single cells could be placed in true 3D isolation by *in situ* fabrication of conjugated-gelatin (a) 3D projection graphic of the masks used to fabricate a free-floating hollow 3D isolation sphere contained within a box. (b) A single MDA-MB-231 cell isolated within a gelatin sphere (72 mg mL^{-1} eosin-gelatin, 26 mg mL^{-1} BSA, 92 mg mL^{-1} gelatin). The cell migrated within the sphere, occasionally causing it to rotate (red arrow). The cell was cultured in 0% FBS L-15 media supplemented with $50 \text{ }\mu\text{M}$ ascorbate. The time after fabrication is indicated in the lower left corner of each frame. Scale bar = $20 \text{ }\mu\text{m}$.

5.3.5 Internalization of In Situ Fabricated Particles

As a proof-of-concept and further demonstration of cell viability, mouse leukaemic monocyte macrophage (RAW 264.7) cells were isolated within eosin-conjugated microstructures with small (1-5 μm) free-floating gelatin particles using the *in situ* fabrication technique. It has been demonstrated that phagocytosis (vesicular internalization of solid material) of particles by macrophage cells is not only determined by the chemical properties of the particle, but also the geometric (e.g., shape and size [37]) and mechanical properties (e.g., stiffness [38]) of the particle. The common materials used to study these effects are polystyrene and polyacrylamide, whose particle properties are manipulated by changing the conditions used during polymerization. Therefore, the geometry and 3D resolution are limited as compared to multiphoton fabrication. Figure 5.11 shows a single RAW 264.7 cell isolated within a gelatin microchamber along with eight gelatin particles of different shapes and sizes. The cell migrated within the structure for more than 14 hours before apparently internalizing a $3\ \mu\text{m} \times 3\ \mu\text{m} \times 3\ \mu\text{m}$ cube-shaped gelatin particle. In the future, more complex particle shapes or chemically functionalized particles could be investigated using this technique, while incorporating confocal fluorescence imaging to show the orientation of the cell surrounding an individual particle.

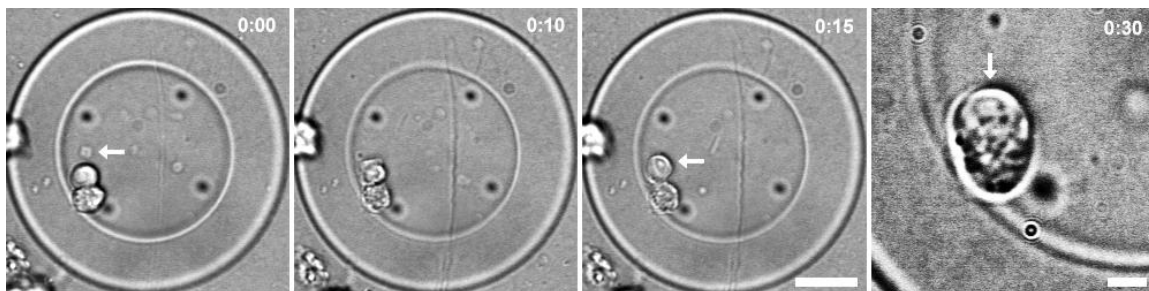


Figure 5.11: Phagocytosis of photofabricated gelatin particles. A single RAW 264.7 macrophage was isolated in a gelatin microstructure with 8 different free-floating fabricated gelatin particles. After migrating within the structure, the cell engulfed a $3\ \mu\text{m} \times 3\ \mu\text{m} \times 3\ \mu\text{m}$ cube-shaped particle (white arrow). Both the microstructure and particles were fabricated from a solution of $70\ \text{mg mL}^{-1}$ eosin-gelatin, $25\ \text{mg mL}^{-1}$ BSA, and $80\ \text{mg mL}^{-1}$ gelatin. Time displayed in the upper right corner of each image corresponds to hours:minutes. Cell was cultured in 10% FBS DMEM at $\sim 35^\circ\text{C}$ and 5% CO_2 during observation. Scale bar (left) = $20\ \mu\text{m}$. Scale bar (right) = $5\ \mu\text{m}$.

5.4 CONCLUSIONS

This chapter presented a technique based on *in situ* multiphoton fabrication for creating biocompatible protein microstructures in the presence of suspended somatic cells. Covalently binding the photosensitizing molecule (eosin) to the crosslinking protein (gelatin) significantly reduced the cytotoxicity of fabrication solutions and allowed for more complex and robust protein microstructures to be fabricated around somatic cells than previous techniques, including free-floating nested structures and 3D containment of single cells. By filtering imaging illumination wavelengths and through the addition of ascorbate acting as a radical scavenger in the cell culture media, the phototoxicity and cytotoxicity of eosin-gelatin microstructures was apparently resolved. Future work will focus on developing specific biological applications for the technique, including

physically isolating different cell types in close proximity that retain the ability to chemically communicate (e.g., immune cells and bacteria). Cell division experiments may be extended through several cell cycles to create isolated, clonal populations of somatic cells as has been previously demonstrated with bacteria [22] and yeast [39]. Additionally, a technique for collecting cells, after isolation and a period of observation, that would allow for endpoint assays, such as PCR and DNA sequencing, would be a significant development in the ability to characterize and explain single-cell behavior using this *in situ* protein microfabrication technique and would be of particular interest to cell biologists.

5.5 REFERENCES

1. Galli, S. J. New insights into ‘the riddle of the mast cells’: Microenvironmental regulation of mast cell development and phenotypic heterogeneity. In *Pathology Reviews* Rubin, E.; Damjanov, I., Eds.; Humana Press: Totowa, NJ, **1990**; 49-77.
2. Tsuru, S.; Yasuda, N.; Murakami, Y.; Ushioda, J.; Kashiwagi, A.; Suzuki, S.; Mori, K.; Ying, B.-W.; Yomo, T. Adaptation by stochastic switching of a monostable genetic circuit in *Escherichia coli*. *Molecular Systems Biology* **2011**, *7*.
3. Capp, J.-P. Stochastic gene expression, disruption of tissue averaging effects and cancer as a disease of development. *BioEssays* **2005**, *27*, 1277–1285.
4. Cai, L.; Friedman, N.; Xie, X. S. Stochastic protein expression in individual cells at the single molecule level. *Nature* **2006**, *440*, 358–362.
5. Morelli, M. J.; Allen, R. J.; Rein ten Wolde, P. Effects of macromolecular crowding on genetic networks. *Biophysical Journal* **2011**, *101*, 2882–2891.
6. Somel, M.; Khaitovich, P.; Bahn, S.; Pääbo, S.; Lachmann, M. Gene expression becomes heterogeneous with age. *Current Biology* **2006**, *16*, R359–360.
7. Bissell, M. J.; Barcellos-Hoff, M. H. The influence of extracellular matrix on gene expression: is structure the message? *Journal of Cell Science – Supplement* **1987**, *8*, 327–343.
8. Elowitz, M. B.; Levine, A. J.; Siggia, E. D.; Swain, P. S. Stochastic gene expression in a single cell. *Science* **2002**, *297*, 1183–1186.
9. Hirschmann-Jax, C. A distinct ‘side population’ of cells with high drug efflux capacity in human tumor cells. *Proceedings of the National Academy of Sciences* **2004**, *101*, 14228–14233.
10. Moriwaki, K.; Shinzaki, S.; Miyoshi, E. GDP-mannose-4,6-dehydratase (GMDS) deficiency renders colon cancer cells resistant to tumor necrosis factor-related apoptosis-inducing ligand (TRAIL) receptor- and CD95-mediated apoptosis by inhibiting complex II formation. *Journal of Biological Chemistry* **2011**, *286*, 43123–43133.
11. Sharma, S. V.; Lee, D. Y.; Li, B.; Quinlan, M. P.; Takahashi, F.; Maheswaran, S.; McDermott, U.; Azizian, N.; Zou, L.; Fischbach, M. A.; Wong, K.-K.; Brandstetter, K.; Wittner, B.; Ramaswamy, S.; Classon, M.; Settleman, J. A chromatin-mediated reversible drug-tolerant state in cancer cell subpopulations. *Cell* **2010**, *141*, 69–80.
12. Eyer, K.; Kuhn, P.; Hanke, C.; Dittrich, P. S. A microchamber array for single cell isolation and analysis of intracellular biomolecules. *Lab on a Chip* **2012**, *12*, 765.

13. Berenschot, E. J. W.; Burouni, N.; Schurink, B.; Van Honschoten, J. W.; Sanders, R. G. P.; Truckenmuller, R.; Jansen, H. V.; Elwenspoek, M. C.; Van Apeldoorn, A. A.; Tas, N. R. 3D Nanofabrication of fluidic components by corner lithography. *Small* **2012**, *8*, 3823–3831.
14. Gach, P. C.; Wang, Y.; Phillips, C.; Sims, C. E.; Allbritton, N. L. Isolation and manipulation of living adherent cells by micromolded magnetic rafts. *Biomicrofluidics* **2011**, *5*, 032002.
15. Yin, H.; Marshall, D. Microfluidics for single cell analysis. *Current Opinion in Biotechnology* **2012**, *23*, 110–119.
16. Di Carlo, D.; Aghdam, N.; Lee, L. P. Single-cell enzyme concentrations, kinetics, and inhibition analysis using high-density hydrodynamic cell isolation arrays. *Analytical Chemistry* **2006**, *78*, 4925–4930.
17. Brouzes, E.; Medkova, M.; Savenelli, N.; Marran, D.; Twardowski, M.; Hutchison, J. B.; Rothberg, J. M.; Link, D. R.; Perrimon, N.; Samuels, M. L. Droplet microfluidic technology for single-cell high-throughput screening. *Proceedings of the National Academy of Sciences* **2009**, *106*, 14195–14200.
18. Frimat, J.-P.; Becker, M.; Chiang, Y.-Y.; Marggraf, U.; Janasek, D.; Hengstler, J. G.; Franzke, J.; West, J. A microfluidic array with cellular valving for single cell co-culture. *Lab on a Chip* **2011**, *11*, 231.
19. Wheeler, A. R.; Thronset, W. R.; Whelan, R. J.; Leach, A. M.; Zare, R. N.; Liao, Y. H.; Farrell, K.; Manger, I. D.; Daridon, A. Microfluidic device for single-cell analysis. *Analytical Chemistry* **2003**, *75*, 3581–3586.
20. Kaehr, B.; Allen, R.; Javier, D. J.; Currie, J.; Shear, J. B. Guiding neuronal development with in situ microfabrication. *Proceedings of the National Academy of Sciences* **2004**, *101*, 16104–16108.
21. Kaehr, B. J. Defining cellular microenvironments using multiphoton lithography. PhD Dissertation, The University of Texas at Austin, **2007**.
22. Connell, J. L. Characterization and microfabrication of environmentally sensitive materials for studying bacterial group behaviors. PhD Dissertation, The University of Texas at Austin, **2012**.
23. Ritschdorff, E. T.; Nielson, R.; Shear, J. B. Multi-focal multiphoton lithography. *Lab on a Chip* **2012**, *12*, 867-871.
24. Pittard, W. B.; Bill, K. Human milk banking. Effect of refrigeration on cellular components. *Clinical Pediatrics* **1981**, *20*, 31–33.
25. Austin, R. H.; Chan, S. S.; Jovin, T. M. Rotational diffusion of cell surface components by time-resolved phosphorescence anisotropy. *Proceedings of the National Academy of Sciences* **1979**, *76*, 5650–5654.

26. Courts, A. The N-terminal amino acid residues of gelatin. 1. Intact gelatins. *Biochemical Journal* **1954**, *58*, 70–74.
27. Hermanson, G. T. *Bioconjugate techniques*; Academic Press: Boston, MA, **2008**, 170.
28. Fackler, O. T.; Grosse, R. Cell motility through plasma membrane blebbing. *The Journal of Cell Biology* **2008**, *181*, 879–884.
29. Weinstein, R. S.; Jilka, R. L.; Parfitt, A. M.; Manolagas, S. C. Inhibition of osteoblastogenesis and promotion of apoptosis of osteoblasts and osteocytes by glucocorticoids. Potential mechanisms of their deleterious effects on bone. *Journal of Clinical Investigation* **1998**, *102*, 274–282.
30. Van Antwerp, D. J.; Martin, S. J.; Kafri, T.; Green, D. R.; Verma, I. M. Suppression of TNF- α -induced apoptosis by NF- κ B. *Science* **1996**, *274*, 787–789.
31. Tanaka, M.; Ito, H.; Adachi, S.; Akimoto, H.; Nishikawa, T.; Kasajima, T.; Marumo, F.; Hiroe, M. Hypoxia induces apoptosis with enhanced expression of Fas antigen messenger RNA in cultured neonatal rat cardiomyocytes. *Circulation Research* **1994**, *75*, 426–433.
32. Fuse, T.; Yoon, K. W.; Kato, T.; Yamada, K. Heat-induced apoptosis in human glioblastoma cell line A172. *Neurosurgery* **1998**, *42*, 843–849.
33. Pinnell, S. R. Regulation of collagen biosynthesis by ascorbic acid: a review. *Yale Journal of Biology and Medicine* **1985**, *58*, 553–559.
34. Frei, B.; England, L.; Ames, B. N. Ascorbate is an outstanding antioxidant in human blood plasma. *Proceedings of the National Academy of Sciences* **1989**, *86*, 6377–6381.
35. Peterkofsky, B. The effect of ascorbic acid on collagen polypeptide synthesis and proline hydroxylation during the growth of cultured fibroblasts. *Archives of Biochemistry and Biophysics* **1972**, *152*, 318–328.
36. Tse, H. T. K.; Weaver, W. M.; Di Carlo, D. Increased asymmetric and multi-daughter cell division in mechanically confined microenvironments. *PLoS ONE* **2012**, *7*, e38986.
37. Champion, J. A. Role of target geometry in phagocytosis. *Proceedings of the National Academy of Sciences* **2006**, *103*, 4930–4934.
38. Beningo, K. A.; Wang, Y. Fc-receptor-mediated phagocytosis is regulated by mechanical properties of the target. *Journal of Cell Science* **2002**, *115*, 849–856.
39. Harper, J. C.; Brozik, S. M.; Brinker, C. J.; Kaehr, B. Biocompatible microfabrication of 3D isolation chambers for targeted confinement of individual cells and their progeny. *Analytical Chemistry* **2012**, 8985–8989.

Bibliography

- Arap, W. Cancer treatment by targeted drug delivery to tumor vasculature in a mouse model. *Science* **1998**, *279*, 377–380.
- Atencia, J.; Cooksey, G. A.; Locascio, L. E. A robust diffusion-based gradient generator for dynamic cell assays. *Lab on a Chip* **2012**, *12*, 309–316.
- Atencia, J.; Morrow, J.; Locascio, L. E. The microfluidic palette: A diffusive gradient generator with spatio-temporal control. *Lab on a Chip* **2009**, *9*, 2707.
- Austin, R. H.; Chan, S. S.; Jovin, T. M. Rotational diffusion of cell surface components by time-resolved phosphorescence anisotropy. *Proceedings of the National Academy of Sciences* **1979**, *76*, 5650–5654.
- Bacia, K.; Kim, S. A.; Schwille, P. Fluorescence cross-correlation spectroscopy in living cells. *Nature Methods* **2006**, *3*, 83–89.
- Balkwill, F. R.; Burke, F. The cytokine network. *Immunology Today* **1989**, *10*, 299–304.
- Bargmann, C. I.; Horvitz, H. R. Chemosensory neurons with overlapping functions direct chemotaxis to multiple chemicals in *C. elegans*. *Neuron* **1991**, *7*, 729–742.
- Becker, W.; Bergmann, A.; Hink, M. A.; Konig, K.; Benndorf, K.; Biskup, C. Fluorescence lifetime imaging by time-correlated single-photon counting. *Microscopy Research and Technique* **2004**, *63*, 58–66.
- Beningo, K. A.; Wang, Y. Fc-receptor-mediated phagocytosis is regulated by mechanical properties of the target. *Journal of Cell Science* **2002**, *115*, 849–856.
- Berenschot, E. J. W.; Burouni, N.; Schurink, B.; van Honschoten, J. W.; Sanders, R. G. P.; Truckenmuller, R.; Jansen, H. V.; Elwenspoek, M. C.; van Apeldoorn, A. A.; Tas, N. R. 3D nanofabrication of fluidic components by corner lithography. *Small* **2012**, *8*, 3823–3831.
- Bissell, M. J.; Barcellos-Hoff, M. H. The influence of extracellular matrix on gene expression: Is structure the message? *Journal of Cell Science Supplement* **1987**, *8*, 327–343.
- Boyden, S. The chemotactic effect of mixtures of antibody and antigen on polymorphonuclear leucocytes. *Journal of Experimental Medicine* **1962**, *115*, 453–466.
- Brehm-Stecher, B. F.; Johnson, E. A. Single-cell microbiology: Tools, technologies, and applications. *Microbiology and Molecular Biology Reviews* **2004**, *68*, 538–559.
- Brouzes, E.; Medkova, M.; Savenelli, N.; Marran, D.; Twardowski, M.; Hutchison, J. B.; Rothberg, J. M.; Link, D. R.; Perrimon, N.; Samuels, M. L. Droplet microfluidic

- technology for single-cell high-throughput screening. *Proceedings of the National Academy of Sciences* **2009**, *106*, 14195–14200.
- Brunette, D. M. The effects of implant surface topography on the behavior of cells. *International Journal of Oral and Maxillofacial Implants* **1988**, *3*, 231–246.
- Cadena, D. L.; Gill, G. N. Receptor tyrosine kinases. *The FASEB Journal* **1992**, *6*, 2332–2337.
- Cai, L.; Friedman, N.; Xie, X. S. Stochastic protein expression in individual cells at the single molecule level. *Nature* **2006**, *440*, 358–362.
- Capp, J.-P. Stochastic gene expression, disruption of tissue averaging effects and cancer as a disease of development. *BioEssays* **2005**, *27*, 1277–1285.
- Carman, C. V.; Sage, P. T.; Sciuto, T. E.; de la Fuente, M. A.; Geha, R. S.; Ochs, H. D.; Dvorak, H. F.; Dvorak, A. M.; Springer, T. A. Transcellular diapedesis is initiated by invasive podosomes. *Immunity* **2007**, *26*, 784–797.
- Champion, J. A. Role of target geometry in phagocytosis. *Proceedings of the National Academy of Sciences* **2006**, *103*, 4930–4934.
- Chen, Y.; Munteanu, A. C.; Huang, Y.-F.; Phillips, J.; Zhu, Z.; Mavros, M.; Tan, W. Mapping receptor density on live cells by using fluorescence correlation spectroscopy. *Chemistry - A European Journal* **2009**, *15*, 5327–5336.
- Chu, S.; Hollberg, L.; Bjorkholm, J.; Cable, A.; Ashkin, A. Three-dimensional viscous confinement and cooling of atoms by resonance radiation pressure. *Physical Review Letters* **1985**, *55*, 48–51.
- Connell, J. L.; Wessel, A. K.; Parsek, M. R.; Ellington, A. D.; Whiteley, M.; Shear, J. B. Probing prokaryotic social behaviors with bacterial “lobster traps.” *mBio* **2010**, *1*, e00202-10–17.
- Connell, J. L. Characterization and microfabrication of environmentally sensitive materials for studying bacterial group behaviors. PhD dissertation, The University of Texas at Austin, **2012**.
- Cooksey, G. A.; Sip, C. G.; Folch, A. A multi-purpose microfluidic perfusion system with combinatorial choice of inputs, mixtures, gradient patterns, and flow rates. *Lab on a Chip* **2009**, *9*, 417.
- Courts, A. The N-terminal amino acid residues of gelatin. 1. Intact gelatins. *Biochemical Journal* **1954**, *58*, 70–74.
- Craig, A. M.; Blackstone, C. D.; Haganir, R. L.; Banker, G. Selective clustering of glutamate and gamma-aminobutyric acid receptors opposite terminals releasing the corresponding neurotransmitters. *Proceedings of the National Academy of Sciences* **1994**, *91*, 12373–12377.

- Denk, W.; Strickler, J. H.; Webb, W. W. Two-photon laser scanning fluorescence microscopy. *Science* **1990**, *248*, 73–76.
- DeRosa, M.; Crutchley, R. J. Photosensitized singlet oxygen and its applications. *Coordination Chemistry Reviews* **2002**, *233-234*, 351–371.
- Dertinger, S. K. W.; Chiu, D. T.; Jeon, N. L.; Whitesides, G. M. Generation of gradients having complex shapes using microfluidic networks. *Analytical Chemistry* **2001**, *73*, 1240–1246.
- Di Carlo, D.; Aghdam, N.; Lee, L. P. Single-cell enzyme concentrations, kinetics, and inhibition analysis using high-density hydrodynamic cell isolation arrays. *Analytical Chemistry* **2006**, *78*, 4925–4930.
- Discher, D. E. Tissue cells feel and respond to the stiffness of their substrate. *Science* **2005**, *310*, 1139–1143.
- Dixon, R. A.; Kobilka, B. K.; Strader, D. J.; Benovic, J. L.; Dohlman, H. G.; Frielle, T.; Bolanowski, M. A.; Bennett, C. D.; Rands, E.; Diehl, R. E.; Mumford, R. A.; Slater, E. E.; Sigal, I. S.; Caron, M. G.; Lefkowitz, R. J.; Strader, C. D. Cloning of the gene and cDNA for mammalian beta-adrenergic receptor and homology with rhodopsin. *Nature* **1986**, *321*, 75–79.
- Duncan, J. R.; Prasse, K. W. Cytology of canine cutaneous round cell tumors. Mast cell tumor, histiocytoma, lymphosarcoma and transmissible venereal tumor. *Veterinary Pathology* **1979**, *16*, 673–679.
- Dyer, P. E.; Pervolaraki, M.; Lippert, T. Experimental studies and thermal modelling of 1064- and 532-nm Nd:YVO₄ micro-laser ablation of polyimide. *Applied Physics A* **2004**, *80*, 529–536.
- Elaboudi, I.; Lazare, S.; Belin, C.; Talaga, D.; Labrugère, C. Underwater excimer laser ablation of polymers. *Applied Physics A* **2008**, *92*, 743–748.
- Elowitz, M. B.; Levine, A. J.; Siggia, E. D.; Swain, P. S. Stochastic gene expression in a single cell. *Science* **2002**, *297*, 1183–1186.
- Engler, A. J.; Sen, S.; Sweeney, H. L.; Discher, D. E. Matrix elasticity directs stem cell lineage specification. *Cell* **2006**, *126*, 677–689.
- Eyer, K.; Kuhn, P.; Hanke, C.; Dittrich, P. S. A microchamber array for single cell isolation and analysis of intracellular biomolecules. *Lab on a Chip* **2012**, *12*, 765.
- Fackler, O. T.; Grosse, R. Cell motility through plasma membrane blebbing. *The Journal of Cell Biology* **2008**, *181*, 879–884.
- Feinerman, O.; Jentsch, G.; Tkach, K. E.; Coward, J. W.; Hathorn, M. M.; Sneddon, M. W.; Emonet, T.; Smith, K. A.; Altan-Bonnet, G. Single-cell quantification of IL-2 response by effector and regulatory T cells reveals critical plasticity in immune response. *Molecular Systems Biology* **2010**, *6*.

- Ferrell, J. E., Jr; Machleder, E. M. The biochemical basis of an all-or-none cell fate switch in *Xenopus* oocytes. *Science* **1998**, *280*, 895–898.
- Finkel, M.; Oddis, C.; Jacob, T.; Watkins, S.; Hattler, B.; Simmons, R. Negative inotropic effects of cytokines on the heart mediated by nitric oxide. *Science* **1992**, *257*, 387–389.
- Flanagan, J. G. Neural map specification by gradients. *Current Opinion in Neurobiology* **2006**, *16*, 59–66.
- Folch, A. *Introduction to BioMEMS*; CRC Press: Boca Raton, FL **2013**.
- Forbes, E. M.; Thompson, A. W.; Yuan, J.; Goodhill, G. J. Calcium and cAMP levels interact to determine attraction versus repulsion in axon guidance. *Neuron* **2012**, *74*, 490–503.
- Foster, A.; Kemp, J. Glutamate- and GABA-based CNS therapeutics. *Current Opinion in Pharmacology* **2006**, *6*, 7–17.
- Foxman, E. F.; Campbell, J. J.; Butcher, E. C. Multistep navigation and the combinatorial control of leukocyte chemotaxis. *Journal of Cell Biology* **1997**, *139*, 1349–1360.
- Foxman, E. F.; Kunkel, E. J.; Butcher, E. C. Integrating conflicting chemotactic signals. The role of memory in leukocyte navigation. *Journal of Cell Biology* **1999**, *147*, 577–588.
- Frei, B.; England, L.; Ames, B. N. Ascorbate is an outstanding antioxidant in human blood plasma. *Proceedings of the National Academy of Sciences* **1989**, *86*, 6377–6381.
- Friedman, N. Inferring cellular networks using probabilistic graphical models. *Science* **2004**, *303*, 799–805.
- Frimat, J.-P.; Becker, M.; Chiang, Y.-Y.; Marggraf, U.; Janasek, D.; Hengstler, J. G.; Franzke, J.; West, J. A microfluidic array with cellular valving for single cell co-culture. *Lab on a Chip* **2011**, *11*, 231–237.
- Fuse, T.; Yoon, K. W.; Kato, T.; Yamada, K. Heat-induced apoptosis in human glioblastoma cell line A172. *Neurosurgery* **1998**, *42*, 843–849.
- Gach, P. C.; Wang, Y.; Phillips, C.; Sims, C. E.; Allbritton, N. L. Isolation and manipulation of living adherent cells by micromolded magnetic rafts. *Biomicrofluidics* **2011**, *5*, 32002–3200212.
- Galli, S. J. New insights into ‘the riddle of the mast cells’: Microenvironmental regulation of mast cell development and phenotypic heterogeneity. In *Pathology Reviews* Rubin, E.; Damjanov, I., Eds.; Humana Press: Totowa, NJ, **1990**; 49-77.
- Georges, P. C.; Janmey, P. A. Cell type-specific response to growth on soft materials. *Journal of Applied Physiology* **2005**, *98*, 1547–1553.

- Geusic, J. E.; Marcos, H. M.; Van Uitert, L. G. Laser oscillations in Nd-doped yttrium aluminum, yttrium gallium and gadolinium garnets. *Applied Physics Letters* **1964**, *4*, 182–184.
- Gordon, A. S.; Collier, K.; Diamond, I. Ethanol regulation of adenosine receptor-stimulated cAMP levels in a clonal neural cell line: an in vitro model of cellular tolerance to ethanol. *Proceedings of the National Academy of Sciences* **1986**, *83*, 2105–2108.
- Gray, A. L. Solid sample introduction by laser ablation for inductively coupled plasma source mass spectrometry. *The Analyst* **1985**, *110*, 551–556.
- Grunze, M.; Lamb, R. N. Preparation and adhesion of ultrathin polyimide films on polycrystalline silver. *Chemical Physics Letters* **1987**, *133*, 283–287.
- Haemmerli, G.; Arnold, B.; Strauli, P. Comparative morphology of cells located on glass and in the loose connective tissue: A study by scanning electron microscopy. *Cell Biology International Reports* **1984**, *8*, 689–702.
- Harper, J. C.; Brozik, S. M.; Brinker, C. J.; Kaehr, B. Biocompatible microfabrication of 3D isolation chambers for targeted confinement of individual cells and their progeny. *Analytical Chemistry* **2012**, 8985–8989.
- Harrison, R. G.; Greenman, M. J.; Mall, F. P.; Jackson, C. M. Observations of the living developing nerve fiber. *The Anatomical Record* **1907**, *1*, 116–128.
- Hermanson, G. T. *Bioconjugate techniques*; Academic Press: Boston, MA, **2008**, 170.
- Hirschmann-Jax, C. A distinct “side population” of cells with high drug efflux capacity in human tumor cells. *Proceedings of the National Academy of Sciences* **2004**, *101*, 14228–14233.
- Hoppe, T. J.; Moorjani, S. G.; Shear, J. B. Generating arbitrary chemical patterns for multi-point dosing of single cells. *Analytical Chemistry* **2013**, *85*, 3746–3751.
- Hynes, R. O. Metastatic Potential: Generic predisposition of the primary tumor or rare, metastatic variants - or both? *Cell* **2003**, *113*, 821–823.
- Hyson, R. L.; Reyes, A. D.; Rubel, E. W. A depolarizing inhibitory response to GABA in brainstem auditory neurons of the chick. *Brain Research* **1995**, *677*, 117–126.
- Itzstein, C.; Coxon, F. P.; Rogers, M. J. The regulation of osteoclast function and bone resorption by small GTPases. *Small GTPases* **2011**, *2*, 117–130.
- Javan, A.; Bennett, W.; Herriott, D. Population inversion and continuous optical maser oscillation in a gas discharge containing a He-Ne mixture. *Physical Review Letters* **1961**, *6*, 106–110.
- Jones, D. J.; Diddams, S. A.; Ranka, J. K.; Stentz, A.; Windeler, R. S.; Hall, J. L.; Cundiff, S. T. Carrier-envelope phase control of femtosecond mode-locked lasers and direct optical frequency synthesis. *Science* **2000**, *288*, 635–639.

- Jones, J. I.; Clemmons, D. R. Insulin-like growth factors and their binding proteins: Biological actions. *Endocrine Reviews* **1995**, *16*, 3–34.
- Kaehr, B. Defining cellular microenvironments using multiphoton lithography. PhD dissertation, University of Texas at Austin, **2007**.
- Kaehr, B.; Allen, R.; Javier, D. J.; Currie, J.; Shear, J. B. Guiding neuronal development with in situ microfabrication. *Proceedings of the National Academy of Sciences* **2004**, *101*, 16104–16108.
- Kaehr, B.; Shear, J. B. Mask-directed multiphoton lithography. *Journal of the American Chemical Society* **2007**, *129*, 1904–1905.
- Kahn, C. R. Membrane receptors for hormones and neurotransmitters. *The Journal of Cell Biology* **1976**, *70*, 261–286.
- Kane, R.; Takayama, S.; Ostuni, E.; Ingber, D. E.; Whitesides, G. M. Patterning proteins and cells using soft lithography. *Biomaterials* **1999**, *20*, 2363–2376.
- Kang, Y.; Siegel, P. M.; Shu, W.; Drobnjak, M.; Kakonen, S. M.; Córdón-Cardo, C.; Guise, T. A.; Massagué, J. A multigenic program mediating breast cancer metastasis to bone. *Cancer Cell* **2003**, *3*, 537–549.
- Karnoub, A. E.; Dash, A. B.; Vo, A. P.; Sullivan, A.; Brooks, M. W.; Bell, G. W.; Richardson, A. L.; Polyak, K.; Tubo, R.; Weinberg, R. A. Mesenchymal stem cells within tumour stroma promote breast cancer metastasis. *Nature* **2007**, *449*, 557–563.
- Kawakami, H.; Hiraka, K.; Nagaoka, S.; Suzuki, Y.; Iwaki, M. Neuronal attachment and outgrowth on a micropatterned fluorinated polyimide surface. *Journal of Artificial Organs* **2004**, *7*, 83–90.
- Keenan, T. M.; Folch, A. Biomolecular gradients in cell culture systems. *Lab on a Chip* **2008**, *8*, 34–57.
- Kelly, T.; Mueller, S. C.; Yeh, Y.; Chen, W.-T. Invadopodia promote proteolysis of a wide variety of extracellular matrix proteins. *Journal of Cellular Physiology* **1994**, *158*, 299–308.
- Khiroug, L.; Giniatullin, R.; Talantova, M.; Nistri, A. Role of intracellular calcium in fast and slow desensitization of P2-receptors in PC12 cells. *British Journal of Pharmacology* **1997**, *120*, 1552–1560.
- Kilfoil, M. L.; Lasko, P.; Abouheif, E. Stochastic variation: From single cells to superorganisms. *HFSP Journal* **2009**, *3*, 379–385.
- Kim, S.; Kim, H. J.; Jeon, N. L. Biological applications of microfluidic gradient devices. *Integrative Biology* **2010**, *2*, 584–603.

- Kim, T. N.; Campbell, K.; Groisman, A.; Kleinfeld, D.; Schaffer, C. B. Femtosecond laser-drilled capillary integrated into a microfluidic device. *Applied Physics Letters* **2005**, *86*, 201106-1–3.
- Kneipp, K.; Wang, Y.; Kneipp, H.; Perelman, L.; Itzkan, I.; Dasari, R.; Feld, M. Single molecule detection using surface-enhanced Raman scattering (SERS). *Physical Review Letters* **1997**, *78*, 1667–1670.
- Kralj, J. M.; Douglass, A. D.; Hochbaum, D. R.; Maclaurin, D.; Cohen, A. E. Optical recording of action potentials in mammalian neurons using a microbial rhodopsin. *Nature Methods* **2011**, *9*, 90–95.
- Kratchmarova, I.; Blagoev, B.; Haack-Sorensen, M.; Kassem, M.; Mann, M. Mechanism of divergent growth factor effects in mesenchymal stem cell differentiation. *Science* **2005**, *308*, 1472–1477.
- Kume, N.; Gimbrone, M. A. Lysophosphatidylcholine transcriptionally induces growth factor gene expression in cultured human endothelial cells. *Journal of Clinical Investigation* **1994**, *93*, 907–911.
- LaFratta, C. N.; Li, L.; Fourkas, J. T. Soft-lithographic replication of 3D microstructures with closed loops. *Proceedings of the National Academy of Sciences* **2006**, *103*, 8589–8594.
- Landecker, H. *Culturing life : How cells became technologies*; Harvard University Press: Cambridge, Mass., 2007.
- Lauffenburger, D. A.; Horwitz, A. F. Cell migration: A physically integrated molecular process. *Cell* **1996**, *84*, 359–369.
- Li, W.; Llopis, J.; Whitney, M.; Zlokarnik, G.; Tsien, R. Y. Cell-permeant caged InsP3 ester shows that Ca²⁺ spike frequency can optimize gene expression. *Nature* **1998**, *392*, 936–941.
- Li Jeon, N.; Baskaran, H.; Dertinger, S. K. W.; Whitesides, G. M.; Van De Water, L.; Toner, M. Neutrophil chemotaxis in linear and complex gradients of interleukin-8 formed in a microfabricated device. *Nature Biotechnology* **2002**, *20*, 826–830.
- Li, R. S.; Jiao, J. The effects of temperature and aging on Young's moduli of polymeric based flexible substrates. In IMAPS 2000: International Symposium on Microelectronics, **2000**, 68–73.
- Liao, Y.; Song, J.; Li, E.; Luo, Y.; Shen, Y.; Chen, D.; Cheng, Y.; Xu, Z.; Sugioka, K.; Midorikawa, K. Rapid prototyping of three-dimensional microfluidic mixers in glass by femtosecond laser direct writing. *Lab on a Chip* **2012**, *12*, 746.
- Lin, F.; Nguyen, C. M.-C.; Wang, S.-J.; Saadi, W.; Gross, S. P.; Jeon, N. L. Neutrophil migration in opposing chemoattractant gradients using microfluidic chemotaxis devices. *Annals of Biomedical Engineering* **2005**, *33*, 475–482.

- Lippert, T. K.; Georgiou, S. *Polymers and light*; Advances in polymer science; Springer: Berlin ; New York, **2004**.
- Liu, L.; Sun, B.; Pedersen, J. N.; Aw Yong, K.-M.; Getzenberg, R. H.; Stone, H. A.; Austin, R. H. Probing the invasiveness of prostate cancer cells in a 3D microfabricated landscape. *Proceedings of the National Academy of Sciences* **2011**, *108*, 6853–6856.
- Mahmud, G.; Campbell, C. J.; Bishop, K. J. M.; Komarova, Y. A.; Chaga, O.; Soh, S.; Huda, S.; Kandere-Grzybowska, K.; Grzybowski, B. A. Directing cell motions on micropatterned ratchets. *Nature Physics* **2009**, *5*, 606–612.
- Maiman, T. H. Stimulated optical radiation in ruby. *Nature* **1960**, *187*, 493–494.
- Mak, M.; Reinhart-King, C. A.; Erickson, D. Microfabricated physical spatial gradients for investigating cell migration and invasion dynamics. *PLoS ONE* **2011**, *6*, e20825.
- Maldve, R. E.; Zhang, T. A.; Ferrani-Kile, K.; Schreiber, S. S.; Lippmann, M. J.; Snyder, G. L.; Fienberg, A. A.; Leslie, S. W.; Gonzales, R. A.; Morrisett, R. A. DARPP-32 and regulation of the ethanol sensitivity of NMDA receptors in the nucleus accumbens. *Nature Neuroscience* **2002**, *5*, 641–648.
- Manz, A.; Graber, N.; Widmer, H. M. Miniaturized total chemical analysis systems: A novel concept for chemical sensing. *Sensors and Actuators B: Chemical* **1990**, *1*, 244–248.
- Marin, O. Directional guidance of interneuron migration to the cerebral cortex relies on subcortical Slit1/2-independent repulsion and cortical attraction. *Development* **2003**, *130*, 1889–1901.
- Marin, O.; Valiente, M.; Ge, X.; Tsai, L.-H. Guiding neuronal cell migrations. *Cold Spring Harbor Perspectives in Biology* **2010**, *2*, a001834.
- Martin, M. M.; Lindqvist, L. The pH dependence of fluorescein fluorescence. *Journal of Luminescence* **1975**, *10*, 381–390.
- Mata, A.; Fleischman, A. J.; Roy, S. Characterization of polydimethylsiloxane (PDMS) properties for biomedical micro/nanosystems. *Biomedical Microdevices* **2005**, *7*, 281–293.
- Matzer, L. Instructional Resources: Drawing with light: Focus on four photographic processes. *Art Education* **2003**, *56*, 25–32.
- Miller, H.; Miller, B. Photodynamic therapy of subretinal neovascularization in the monkey eye. *Archives of Ophthalmology* **1993**, *111*, 855–860.
- Ming, G.; Song, H.; Berninger, B.; Holt, C. E.; Tessier-Lavigne, M.; Poo, M. cAMP-dependent growth cone guidance by netrin-1. *Neuron* **1997**, *19*, 1225–1235.

- Mooibroek, M. J.; Wang, J. H. Integration of signal-transduction processes. *Biochemistry and Cell Biology* **1988**, *66*, 557–566.
- Moorjani, S.; Nielson, R.; Chang, X. A.; Shear, J. B. Dynamic remodeling of subcellular chemical gradients using a multi-directional flow device. *Lab on a Chip* **2010**, *10*, 2139–2146.
- Morelli, M. J.; Allen, R. J.; Rein ten Wolde, P. Effects of macromolecular crowding on genetic networks. *Biophysical Journal* **2011**, *101*, 2882–2891.
- Moriwaki, K.; Shinzaki, S.; Miyoshi, E. GDP-mannose-4,6-dehydratase (GMDS) deficiency renders colon cancer cells resistant to tumor necrosis factor-related apoptosis-inducing ligand (TRAIL) receptor- and CD95-mediated apoptosis by inhibiting complex II formation. *Journal of Biological Chemistry* **2011**, *286*, 43123–43133.
- Mosesson, Y.; Mills, G. B.; Yarden, Y. Derailed endocytosis: an emerging feature of cancer. *Nature Reviews Cancer* **2008**, *8*, 835–850.
- Nemes, P.; Vertes, A. Laser ablation electrospray ionization for atmospheric pressure, in vivo, and imaging mass spectrometry. *Analytical Chemistry* **2007**, *79*, 8098–8106.
- Newbold, R. F.; Overell, R. W.; Connell, J. R. Induction of immortality is an early event in malignant transformation of mammalian cells by carcinogens. *Nature* **1982**, *299*, 633–635.
- Nielson, R.; Kaehr, B.; Shear, J. B. Microreplication and design of biological architectures using dynamic-mask multiphoton lithography. *Small* **2009**, *5*, 120–125.
- Nielson, R.; Shear, J. B. Parallel chemical dosing of subcellular targets. *Analytical Chemistry* **2006**, *78*, 5987–5993.
- Olofsson, J.; Bridle, H.; Jesorka, A.; Isaksson, I.; Weber, S.; Orwar, O. Direct access and control of the intracellular solution environment in single cells. *Analytical Chemistry* **2009**, *81*, 1810–1818.
- Olofsson, J.; Pihl, J.; Sinclair, J.; Sahlin, E.; Karlsson, M.; Orwar, O. A microfluidics approach to the problem of creating separate solution environments accessible from macroscopic volumes. *Analytical Chemistry* **2004**, *76*, 4968–4976.
- Olson, E. N. Development. The path to the heart and the road not taken. *Science* **2001**, *291*, 2327–2328.
- Paegel, B. M.; Blazej, R. G.; Mathies, R. A. Microfluidic devices for DNA sequencing: Sample preparation and electrophoretic analysis. *Current Opinion in Biotechnology* **2003**, *14*, 42–50.
- Pawley, J. B. *Handbook of biological confocal microscopy*; 3rd ed.; Springer: New York, NY, **2006**.

- Pelham, R. J.; Wang, Y. Cell locomotion and focal adhesions are regulated by substrate flexibility. *Proceedings of the National Academy of Sciences* **1997**, *94*, 13661–13665.
- Perlmann, G. E.; Longworth, L. G. The specific refractive increment of some purified proteins. *Journal of the American Chemical Society* **1948**, *70*, 2719–2724.
- Peterkofsky, B. The effect of ascorbic acid on collagen polypeptide synthesis and proline hydroxylation during the growth of cultured fibroblasts. *Archives of Biochemistry and Biophysics* **1972**, *152*, 318–328.
- Pinnell, S. R. Regulation of collagen biosynthesis by ascorbic acid: a review. *Yale Journal of Biology and Medicine* **1985**, *58*, 553–559.
- Pittard, W. B., 3rd; Bill, K. Human milk banking. Effect of refrigeration on cellular components. *Clinical Pediatrics* **1981**, *20*, 31–33.
- Pitts, J. D.; Campagnola, P. J.; Epling, G. A.; Goodman, S. L. Submicron multiphoton free-form fabrication of proteins and polymers: Studies of reaction efficiencies and applications in sustained release. *Macromolecules* **2000**, *33*, 1514–1523.
- Porterfield, S. P.; Hendrich, C. E. The role of thyroid hormones in prenatal and neonatal neurological development – Current perspectives. *Endocrine Reviews* **1993**, *14*, 94–106.
- Postma, M.; Haastert, P. J. M. Mathematics of experimentally generated chemoattractant gradients. In *Chemotaxis*; Jin, T.; Hereld, D., Eds.; Humana Press: Totowa, NJ, **2009**; Vol. 571, 473–488.
- Prager, D. J.; Bowman, R. L.; Vurek, G. G. Constant Volume, Self-filling nanoliter pipette: Construction and calibration. *Science* **1965**, *147*, 606–608.
- Purvis, J. E.; Lahav, G. Encoding and Decoding Cellular Information through Signaling Dynamics. *Cell* **2013**, *152*, 945–956.
- Raper, J.; Mason, C. Cellular Strategies of Axonal Pathfinding. *Cold Spring Harbor Perspectives in Biology* **2010**, *2*, a001933.
- Richardson, R. R.; Miller, J. A.; Reichert, W. M. Polyimides as biomaterials: preliminary biocompatibility testing. *Biomaterials* **1993**, *14*, 627–635.
- Ritschdorff, E. T.; Nielson, R.; Shear, J. B. Multi-focal multiphoton lithography. *Lab on a Chip* **2012**, *12*, 867–871.
- Santillo, M. F.; Arcibal, I. G.; Ewing, A. G. Flow characterization of a microfluidic device to selectively and reliably apply reagents to a cellular network. *Lab on a Chip* **2007**, *7*, 1212–1215.
- Sarrio, D.; Rodriguez-Pinilla, S. M.; Hardisson, D.; Cano, A.; Moreno-Bueno, G.; Palacios, J. Epithelial-mesenchymal transition in breast cancer relates to the basal-like phenotype. *Cancer Research* **2008**, *68*, 989–997.

- Schawlow, A.; Townes, C. Infrared and optical masers. *Physical Review* **1958**, *112*, 1940–1949.
- Scherber, C.; Aranyosi, A. J.; Kulemann, B.; Thayer, S. P.; Toner, M.; Iliopoulos, O.; Irimia, D. Epithelial cell guidance by self-generated EGF gradients. *Integrative Biology* **2012**, *4*, 259–269.
- Schultheiss, D.; Bloom, D. A.; Wefer, J.; Jonas, U. Tissue engineering from Adam to the zygote: historical reflections. *World Journal of Urology* **2000**, *18*, 84–90.
- Seidlits, S. K.; Khaing, Z. Z.; Petersen, R. R.; Nickels, J. D.; Vanscoy, J. E.; Shear, J. B.; Schmidt, C. E. The effects of hyaluronic acid hydrogels with tunable mechanical properties on neural progenitor cell differentiation. *Biomaterials* **2010**, *31*, 3930–3940.
- Seidlits, S. K.; Schmidt, C. E.; Shear, J. B. High-resolution patterning of hydrogels in three dimensions using direct-write photofabrication for cell guidance. *Advanced Functional Materials* **2009**, *19*, 3543–3551.
- Seo, J.-M.; Kim, S. J.; Chung, H.; Kim, E. T.; Yu, H. G.; Yu, Y. S. Biocompatibility of polyimide microelectrode array for retinal stimulation. *Materials Science and Engineering: C* **2004**, *24*, 185–189.
- Sharma, S. V.; Lee, D. Y.; Li, B.; Quinlan, M. P.; Takahashi, F.; Maheswaran, S.; McDermott, U.; Azizian, N.; Zou, L.; Fischbach, M. A.; Wong, K.-K.; Brandstetter, K.; Wittner, B.; Ramaswamy, S.; Classon, M.; Settleman, J. A chromatin-mediated reversible drug-tolerant state in cancer cell subpopulations. *Cell* **2010**, *141*, 69–80.
- Shear, J. B. Multiphoton-excited fluorescence in bioanalytical chemistry. *Analytical Chemistry* **1999**, *71*, 598A–605A.
- Shen, H.-R.; Spikes, J. D.; Kopečeková, P.; Kopeček, J. Photodynamic crosslinking of proteins. I. Model studies using histidine- and lysine-containing N-(2-hydroxypropyl) methacrylamide copolymers. *Journal of Photochemistry and Photobiology B: Biology* **1996**, *34*, 203–210.
- Shu, C. J. Visualization of a primary anti-tumor immune response by positron emission tomography. *Proceedings of the National Academy of Sciences* **2005**, *102*, 17412–17417.
- Sims, C. E.; Allbritton, N. L. Analysis of single mammalian cells on-chip. *Lab on a Chip* **2007**, *7*, 423–440.
- Somel, M.; Khaitovich, P.; Bahn, S.; Pääbo, S.; Lachmann, M. Gene expression becomes heterogeneous with age. *Current Biology* **2006**, *16*, R359–360.
- Sorokin, P. P.; Lankard, J. R. Stimulated emission observed from an organic dye, chloroaluminum phthalocyanine. *IBM Journal of Research and Development* **1966**, *10*, 162–163.

- Spence, D. E.; Kean, P. N.; Sibbett, W. 60-fsec pulse generation from a self-mode-locked Ti:sapphire laser. *Optics Letters* **1991**, *16*, 42–44.
- Spikes, J. D.; Shen, H.-R.; Kopečková, P.; Kopeček, J. Photodynamic crosslinking of proteins. III. Kinetics of the FMN- and rose bengal-sensitized photooxidation and intermolecular crosslinking of model tyrosine-containing N-(2-Hydroxypropyl)methacrylamide copolymers. *Photochemistry and Photobiology* **1999**, *70*, 130–137.
- Spivey, E. C. Multiphoton lithography of mechanically and functionally tunable hydrogels. PhD dissertation, University of Texas at Austin, **2012**.
- Spivey, E. C.; Ritschdorff, E. T.; Connell, J. L.; McLennon, C. A.; Schmidt, C. E.; Shear, J. B. Multiphoton lithography of unconstrained three-dimensional protein microstructures. *Advanced Functional Materials* **2013**, *23*, 333–339.
- Spradling, A.; Drummond-Barbosa, D.; Kai, T. Stem cells find their niche. *Nature* **2001**, *414*, 98–104.
- Stahling-Hampton, K.; Jackson, P. D.; Clark, M. J.; Brand, A. H.; Hoffmann, F. M. Specificity of bone morphogenetic protein-related factors: cell fate and gene expression changes in *Drosophila* embryos induced by decapentaplegic but not 60A. *Cell Growth and Differentiation* **1994**, *5*, 585–593.
- Stosiek, C. In vivo two-photon calcium imaging of neuronal networks. *Proceedings of the National Academy of Sciences* **2003**, *100*, 7319–7324.
- Sullivan, R.; Graham, C. H. Hypoxia-driven selection of the metastatic phenotype. *Cancer and Metastasis Reviews* **2007**, *26*, 319–331.
- Takayama, S.; Ostuni, E.; LeDuc, P.; Naruse, K.; Ingber, D. E.; Whitesides, G. M. Subcellular positioning of small molecules. *Nature* **2001**, *411*, 1016.
- Takayama, S.; Ostuni, E.; LeDuc, P.; Naruse, K.; Ingber, D. E.; Whitesides, G. M. Selective chemical treatment of cellular microdomains using multiple laminar streams. *Chemistry & Biology* **2003**, *10*, 123–130.
- Tanaka, M.; Ito, H.; Adachi, S.; Akimoto, H.; Nishikawa, T.; Kasajima, T.; Marumo, F.; Hiroe, M. Hypoxia induces apoptosis with enhanced expression of Fas antigen messenger RNA in cultured neonatal rat cardiomyocytes. *Circulation Research* **1994**, *75*, 426–433.
- Taylor, A. M.; Blurton-Jones, M.; Rhee, S. W.; Cribbs, D. H.; Cotman, C. W.; Jeon, N. L. A microfluidic culture platform for CNS axonal injury, regeneration and transport. *Nature Methods* **2005**, *2*, 599–605.
- Thangawng, A. L.; Ruoff, R. S.; Swartz, M. A.; Glucksberg, M. R. An ultra-thin PDMS membrane as a bio/micro–nano interface: fabrication and characterization. *Biomedical Microdevices* **2007**, *9*, 587–595.

- Tourovskaya, A.; Figueroa-Masot, X.; Folch, A. Differentiation-on-a-chip: A microfluidic platform for long-term cell culture studies. *Lab on a Chip* **2005**, *5*, 14–19.
- Truskey, G. A.; Yuan, F.; Katz, D. F. *Transport phenomena in biological systems*; Pearson/Prentice Hall: Upper Saddle River, N.J., **2004**.
- Tse, H. T. K.; Weaver, W. M.; Di Carlo, D. Increased asymmetric and multi-daughter cell division in mechanically confined microenvironments. *PLoS ONE* **2012**, *7*, e38986.
- Tse, J. M.; Cheng, G.; Tyrrell, J. A.; Wilcox-Adelman, S. A.; Boucher, Y.; Jain, R. K.; Munn, L. L. Mechanical compression drives cancer cells toward invasive phenotype. *Proceedings of the National Academy of Sciences* **2011**, *109*, 911–916.
- Tsuru, S.; Yasuda, N.; Murakami, Y.; Ushioda, J.; Kashiwagi, A.; Suzuki, S.; Mori, K.; Ying, B.-W.; Yomo, T. Adaptation by stochastic switching of a monostable genetic circuit in *Escherichia coli*. *Molecular Systems Biology* **2011**, *7*.
- Umesono, K.; Giguere, V.; Glass, C. K.; Rosenfeld, M. G.; Evans, R. M. Retinoic acid and thyroid hormone induce gene expression through a common responsive element. *Nature* **1988**, *336*, 262–265.
- Van den Pol, A. N.; Trombley, P. Q. Glutamate neurons in hypothalamus regulate excitatory transmission. *The Journal of Neuroscience* **1993**, *13*, 2829–2836.
- Van Antwerp, D. J.; Martin, S. J.; Kafri, T.; Green, D. R.; Verma, I. M. Suppression of TNF- α -Induced Apoptosis by NF- κ B. *Science* **1996**, *274*, 787–789.
- VanDersarl, J. J.; Xu, A. M.; Melosh, N. A. Rapid spatial and temporal controlled signal delivery over large cell culture areas. *Lab on a Chip* **2011**, *11*, 3057–3063.
- Vemuri, S.; Yu, C.-D.; Wangsatorntanakun, V.; Roosdorp, N. Large-scale production of liposomes by a microfluidizer. *Drug Development and Industrial Pharmacy* **1990**, *16*, 2243–2256.
- Vergara, D.; Merlot, B.; Lucot, J.-P.; Collinet, P.; Vinatier, D.; Fournier, I.; Salzet, M. Epithelial–mesenchymal transition in ovarian cancer. *Cancer Letters* **2010**, *291*, 59–66.
- Wang, K.; Wang, K.; Li, W.; Huang, T.; Li, R.; Wang, D.; Shen, B.; Chen, X. Characterizing breast cancer xenograft epidermal growth factor receptor expression by using near-infrared optical imaging. *Acta Radiologica* **2009**, *50*, 1095–1103.
- Wang, M. M.; Tu, E.; Raymond, D. E.; Yang, J. M.; Zhang, H.; Hagen, N.; Dees, B.; Mercer, E. M.; Forster, A. H.; Kariv, I.; Marchand, P. J.; Butler, W. F. Microfluidic sorting of mammalian cells by optical force switching. *Nature Biotechnology* **2004**, *23*, 83–87.

- Wang, S.-J.; Saadi, W.; Lin, F.; Minh-Canh Nguyen, C.; Li Jeon, N. Differential effects of EGF gradient profiles on MDA-MB-231 breast cancer cell chemotaxis. *Experimental Cell Research* **2004**, *300*, 180–189.
- Weaver, A. M. Invadopodia: Specialized cell structures for cancer invasion. *Clinical & Experimental Metastasis* **2006**, *23*, 97–105.
- Webb, R. H. Confocal optical microscopy. *Reports on Progress in Physics* **1996**, *59*, 427–471.
- Weibel, D.; Whitesides, G. Applications of microfluidics in chemical biology. *Current Opinion in Chemical Biology* **2006**, *10*, 584–591.
- Weinstein, R. S.; Jilka, R. L.; Parfitt, A. M.; Manolagas, S. C. Inhibition of osteoblastogenesis and promotion of apoptosis of osteoblasts and osteocytes by glucocorticoids. Potential mechanisms of their deleterious effects on bone. *Journal of Clinical Investigation* **1998**, *102*, 274–282.
- Wheeler, A. R.; Thronset, W. R.; Whelan, R. J.; Leach, A. M.; Zare, R. N.; Liao, Y. H.; Farrell, K.; Manger, I. D.; Daridon, A. Microfluidic device for single-cell Analysis. *Analytical Chemistry* **2003**, *75*, 3581–3586.
- Whitesides, G. M. The origins and the future of microfluidics. *Nature* **2006**, *442*, 368–373.
- Wittekind, C.; Neid, M. Cancer invasion and metastasis. *Oncology* **2005**, *69*, 14–16.
- Xia, Y.; Whitesides, G. M. Soft lithography. *Annual Review of Materials Science* **1998**, *28*, 153–184.
- Xu, K.; Babcock, H. P.; Zhuang, X. Dual-objective STORM reveals three-dimensional filament organization in the actin cytoskeleton. *Nature Methods* **2012**, *9*, 185–188.
- Yin, H.; Marshall, D. Microfluidics for single cell analysis. *Current Opinion in Biotechnology* **2012**, *23*, 110–119.
- Young, E. W. K.; Beebe, D. J. Fundamentals of microfluidic cell culture in controlled microenvironments. *Chemical Society Reviews* **2010**, *39*, 1036–1048.
- Zaman, M. H.; Trapani, L. M.; Sieminski, A. L.; Siemeski, A.; Mackellar, D.; Gong, H.; Kamm, R. D.; Wells, A.; Lauffenburger, D. A.; Matsudaira, P. Migration of tumor cells in 3D matrices is governed by matrix stiffness along with cell-matrix adhesion and proteolysis. *Proceedings of the National Academy of Sciences* **2006**, *103*, 10889–10894.
- Zewail, A. H. Femtochemistry: Atomic-scale dynamics of the chemical bond *The Journal of Physical Chemistry A* **2000**, *104*, 5660–5694.
- Zhao, Y.; Inayat, S.; Dikin, D. A.; Singer, J. H.; Ruoff, R. S.; Troy, J. B. Patch clamp technique: Review of the current state of the art and potential contributions from

- nanoengineering. *Proceedings of the Institution of Mechanical Engineers, Part N: Journal of Nanoengineering and Nanosystems* **2008**, 222, 1–11.
- Lu, Z.; Moraes, C.; Zhao, Y.; You, L.; Simmons, C. A.; Sun, Y. A micromanipulation system for single cell deposition. In: IEEE, **2010**; 494–499.
- Zigmond, S. H. Ability of polymorphonuclear leukocytes to orient in gradients of chemotactic factors. *Journal of Cell Biology* **1977**, 75, 606–616.